

Romain JAN
romain.jan@isae-sup Aero.fr

Experimental validation of ASWING. Part I: Aerodynamics

Supervisors:

- Prof J-M. Moschetta
- Prof J-P. Condomines

ISAE-Supaero: Technical report, ISAE-ASW-1 2024

Abstract

This technical report presents an experimental validation and modification of the ASWING aeroelastic framework. The study focuses on the aerodynamic model. Firstly, the report reviews the nonlinear unsteady lift line and slender body theories. Then, modifications to the ASWING framework are proposed based on recent literature. The experimental validation is divided into two sections: steady and unsteady. The study evaluates the nonlinear steady lift line model using six single planform configurations and examines stall predictions where possible. The investigation also includes the effects of ailerons and flaps on roll and yaw performance. Additionally, steady wake interaction predictions are evaluated using two tandem configurations with particular emphasis on lift and drag up to stall. The study evaluates the slender body theory using four airship configurations to highlight a numerical anomaly with the current version of ASWING. A solution is proposed. Additionally, the unsteady lift line model is evaluated using two cases: a plunging airfoil and a wing. Particular emphasis is placed on the time average, amplitude and phase of the first harmonic, and the phase average of the lift. The investigation includes several reduced frequencies, amplitudes, and wing root angles. The paper concludes by comparing the computational time costs with higher fidelity methods. Based on this initial comparative work, ASWING appears to be an attractive, fast, and accurate aerodynamic pre-design tool.

Important note to the reader:

This work has not been peer reviewed yet. Only the author's PhD referee members (Professors Mark Drela, Rafael Palacios, Eric Laurendeau and Murat Bronz) had access to this work and have authorised the defence. For more details, please refer to <https://www.theses.fr/s251420>. Nevertheless, this material is in a process of publication in peer reviewed journals, in a shorter version. This document will be updated if new material has to be added.

About the data presented in this report:

This report presents various comparisons with different sets of experimental data. The latter and numerical simulations are available on Git Repository: ISAE ASWING Validation. However, if you consider using them for your own studies, please cite this work and the related ones from which data are coming. Contact: romain.jan@isae-supaero.fr

Version notes

This technical report aims to be updated if new experimental cases and ASWING modifications have to be added. Also, the updates aim to take into account the feedback of the community (typos, theoretical development mistakes, etc).

Versioning syntax:

The version of this document is given as follows: I.X.y, where I denotes the first part of this experimental evaluation, X and y denote respectively major and minor updates.

- **Version I.1.0:**

(30/07/2023) This version is the one submitted to the author's PhD referee as a partial fulfilment of the PhD degree. This version presented the following experimental cases:

- CASE 1: a straight wing for total lift and drag prediction up to stall
- CASE 2: a 45 degrees swept back wing for total lift and drag prediction
- CASE 3: an elliptical wing (total lift and drag)
- CASE 4: a crescent wing (total lift and drag)
- CASE 5: a 45 degrees dihedral angle wing (StarCCM+)
- CASE 6: a straight wing, rolling and yawing moments induced by various ailerons.
- CASE 7: Tandem 1, total lift prediction up to stall
- CASE 8: Tandem 2, total lift and drag on linear lift range
- CASE 9 A-E: Five swept back and forward wings, lift distribution and centre of pressure location.
- CASE 10: Straight wing with tip sails, lift-to-drag ratio
- CASE 11: a swept back wing with Whitcomb winglets, transonic total lift and drag
- Four Airships: slender body theory validation, lift distribution and pressure distribution.
- U-CASE 1 (Unsteady case) 2D plunging airfoil, lift peak to peak, phase and time average.
- U-CASE 2 (Unsteady case) 3D plunging airfoil, lift peak to peak, and time average.

This version also proposed a bench of modifications to the code summed up as follows

- viscous loop and the lift, lift slope correction based on 2D polars
- viscous loop on the drag based on XFOIL polars
- lift stall limits shift due to deflected flap
- flap derivatives interpolation with the Reynolds number
- Slender body theory correction to avoid numerical noise due to implementation

- **Version I.2.0:**

(16/01/2024) Major typos have been corrected. Some experimental validation cases have been added and are summed up as follows:

- CASE 12 A-B: rectangular wing with slotted and plain flaps. Use for ground effects prediction on lift-to-drag ratio. Some theoretical developments have been added
- CASE 13 A-D: airships of version I.1.0 have been renamed.
- CASE 14: 45 degrees swept-back wing and fuselage for wing/body interaction studies. Some theoretical developments have been added.

- ***Version I.3.0:***

(23/04/2024) A new experimental validation case and modifications have been brought to this report and are summed up as follows:

- CASE 15 A-C: Three joined wings aircrafts are studied at $\text{Ma} = 0.35$. Its longitudinal characteristic Aswing predictions are compared to experiments. In particular, lift, drag and pitching moment, that is the first time in this report. Also the effect of the rear wing elevator deflection on the longitudinal characteristic is assessed. This case is of interest to show, why not modelling the fuselage lift carry over can bring significant discrepancies.
- The cases' names have been modified. The steady aerodynamic are defined as \mathcal{SA} followed by the case number, while the unsteady one have been named \mathcal{UA} . This has been done so that to match the formalism used in a submitted journal article that summarized those technical reports.
- List of tables and figures have been added.
- Markers of figure 33 to 36 (Case UA-2) are no longer empty to better distinguish the 2D from the 3D unsteady cases.

- ***Version I.4.0:***

(28/02/2025) Creation of a Git repository

- A git repository has been created. It can be found here: Git Repository: [ISAE ASWING Validation](#)
- The level of repeatability of each case in the Git is specified in the cases description tables. This is because Aswing has been modified for some of them. As the source code is not allowed to be diffused, only the Aswing output data is contained in the Git repository. This is qualified as a "Partial" repeatable case.

Contents

1	Introduction	11
2	The extended unsteady slender body theory	13
3	The extended non-linear lifting line model	13
3.1	Vectorial formulation of the unsteady Kutta-Joukowsky theorem	13
3.2	Modelling drag	15
3.3	Aerodynamic moment	15
3.4	Extented Kutta-Joukowsky condition	15
3.5	Velocity influence of lifting bodies	18
4	ASWING aerodynamic model improvements	20
5	Numerical mesh convergence, aliasing and stability analysis	21
6	Experimental validation	22
6.1	Steady non-linear lifting line validation (Cases SA-1 to 12)	22
6.2	The Slender Body Theory validation (Case SA-13)	40
6.3	Steady wing-fuselage interference (Case SA-14)	40
6.4	Lifting surfaces close interaction: rear wing induced upstream curvature (Case SA-15)	43
6.5	Unsteady aerodynamics validation (Cases UA-1 to 2)	48
7	Computational performance	54
8	Conclusions	58
References		73

List of Figures

1	ASWING citation history, blue bars : mentioned as an existing tool; yellow : used as a tool ; orange : used and validated against experimental or higher fidelity CFD data	12
2	Slender Body Theory : lift and drag directions. The drag is split into 2 components : 1 - the pressure drag is always aligned with V_{\perp} and 2 - the skin friction drag aligned with the upcoming velocity V	14
3	ASWING lifting line forces directions (a) 3D directions of lift and drag contributions (b) zoom on the boundary profile low-speed profile	16
4	ASWING horseshoe representation (a) 2D Kutta Joukowski plane (b) top view with corrected chord c_{β} (c) ASWING wake straight shedding (d) Modern literature horseshoe representation	16
5	Recovering airfoil camber line (first line) and flap deflection effect (second line):	17
6	Modulus and phase comparison of Theordorsen and ASWING lag function	18
7	Slender Body Theory: Flow field modelling with source/sink and doublet distribution, 2D simplification of the problem.	19
8	Ground effect modelling in ASWING	21
9	Numerical scheme relative convergence to theoretical Prandlt's solution (inviscid case)	22
10	CASE # 1: Aliasing effects on the Γ distribution due to floating point number of digits in ASWING outputs file (default value: 2 for coordinates variables).	24
11	CASE $\mathcal{S}\mathcal{A}$ -1 : Straight wing C_L and C_D predictions versus experimental from [1]. Improvement of C_L and C_D brought by a viscous loop and a quadratic varying 2D drag coefficient.	26
12	CASE $\mathcal{S}\mathcal{A}$ -2 : 45° swept back wing C_L and C_D predictions versus experimental from J. Weber, Dr.rer.nat. and G. G. Brebner, M.A-1958. Improvement of C_L and C_D brought by a viscous loop and a quadratic varying 2D drag coefficient.	26
13	CASE $\mathcal{S}\mathcal{A}$ -3 : Quasi-Elliptical wing C_L and C_D predictions versus experimental from van Dam et al. 1991). Improvement of C_L and C_D brought by a viscous loop and a quadratic varying 2D drag coefficient.	28
14	CASE $\mathcal{S}\mathcal{A}$ -4 : Crescent wing C_L and C_D predictions versus experimental from van Dam et al. 1991. Improvement of C_L and C_D brought by a viscous loop and a quadratic varying 2D drag coefficient.	28
15	CASE $\mathcal{S}\mathcal{A}$ -5 : Straight Wing with 45° dihedral angle C_L and C_D predictions	29
16	CASE $\mathcal{S}\mathcal{A}$ -6: Effect of various deflected ailerons on the rolling and yawing moment coefficients. ASWING prediction against experimental data (Heald and Strother, 1929). Level flight condition (un-stalled $\alpha = 4^{\circ}$)	30
17	CASE $\mathcal{S}\mathcal{A}$ -6: Effect of various deflected ailerons on the rolling and yawing moment coefficients. ASWING prediction against experimental data from Heald and Strother 1930. Level flight condition (post-stall $\alpha = 16^{\circ}$)	31
18	CASE $\mathcal{S}\mathcal{A}$ -7 : Tandem #1, total, backward and forward wing C_L and C_D predictions versus experimental and CFD data from Feistel et al. (1981)and Cheng and Wang (2018))	33
19	CASE $\mathcal{S}\mathcal{A}$ -8 : Tandem #2, total and backward wing C_L predictions vs higher fidelity data from Cheng and Wang (2018)	34

20	CASE <i>UA</i> -9 A-E: lift coefficient and centre of pressure location predictions for 5 swept forward and backward wing. Comparison with experiments from McCormack and Stevens Jr (1947)	36
21	CASE <i>SA</i> -10: Lift and drag predictions of configurations with bent winglet and tip sails. Comparison with experimental data from (Miklosovic, 2008)	37
22	CASE <i>SA</i> -11. Lift and drag predictions of the KC-135 wing with various wingtip devices. W-A : Wing Alone, WT-U : Wingtip up only: W-E : Wing Extension, WT-U&D Wingtip Up and Down. Experimental data from Jacobs et al. (1977) part of the program Barber and Selegan (1982)	39
23	CASE <i>SA</i> -12 A-B: Ground effects on lift and drag predictions on a rectangular wing with no flaps and slotted one. Experimental data adapted from Recant (1939)	41
24	CASE <i>SA</i> -13 A-D: Lift and dynamic pressure distribution ASWING predictions on different airship against experimental data from Von Karman (1930)	42
25	CASE <i>SA</i> -14: Wing body interference illustration and comparison with experiments. ASWING predictions against data from Martina-1956	44
26	Case <i>SA</i> -15 A-C : Diamond joined wing geometry and proximity effect	45
27	CASE <i>SA</i> -15 A-C : Joined wing JW-1 to 3 longitudinal characteristics. Aswing 5.98 prediction against experimental data from Smith and Stonum-1989	46
28	CASE <i>SA</i> -15 C : Joined wing JW-3 Longitudinal control. Rear wing inboard and outboard flap deflected at 15°. Aswing 5.98 prediction for various hinge location against experimental data from Smith and Stonum-1989	47
29	Case <i>UA</i> -1: 2D lift coefficient first harmonic amplitude and phase lag at $\alpha = 0^\circ$, effect of the reduced amplitude and frequency. ASWING prediction comparison with experiments (Chiereghin et al. 2017b)	50
30	Case <i>UA</i> -1: 2D lift coefficient first harmonic amplitude and phase lag at $\alpha = 5^\circ$, effect of the reduced amplitude and frequency. ASWING prediction comparison with experiments (Chiereghin et al. 2017b)	51
31	Case <i>UA</i> -1: 2D lift coefficient first harmonic amplitude and phase lag at $\alpha = 9^\circ$, effect of the reduced amplitude and frequency. ASWING prediction comparison with experiments (Chiereghin et al. 2017b)	52
32	Case <i>UA</i> -1: Phase lag average for 2 reduced frequencies and 3 angles of attack. ASWING predictions versus experiments (Chiereghin et al. 2017b). Comparison with a corrected function taking into account the time average experimental data.	53
33	Case <i>UA</i> -2: 3D lift coefficient first harmonic amplitude and phase lag at $\alpha = 0^\circ$, effect of the reduced amplitude and frequency. ASWING prediction comparison with experiments from Chiereghin et al. (2017a)	55
34	Case <i>UA</i> -2: 3D lift coefficient first harmonic amplitude and phase lag at $\alpha = 5^\circ$, effect of the reduced amplitude and frequency. ASWING prediction comparison with experiments from Chiereghin et al. (2017a)	56
35	Case <i>UA</i> -2: 3D lift coefficient first harmonic amplitude and phase lag at $\alpha = 9^\circ$, effect of the reduced amplitude and frequency. ASWING prediction comparison with experiments from Chiereghin et al. (2017a)	57
36	Case <i>UA</i> -1&2: Leading Edge Vortices effect on the time average 2D and 3D lift coefficient versus ASWING predictions. Comparison with experimental data from Chiereghin et al. 2017b and 2017a	58

37	Kutta-Joukowsky theorem illustration of the vortex sheet lumping and simplification	64
38	Effect of Reynolds number and flap deflection on ASWING airfoil derivatives. Illustration on the NACA4415	66
39	Appendix-D:Boeing KC-135 geometry and airfoils	67
40	Appendix-D: Boeing KC-135 geometry and airfoils	68
41	Appendix-E : Diamond Joined wing (JWRA) forward wing airfoil polars	69
42	Appendix-E : Diamond Joined wing (JWRA) forward wing airfoil flap derivatives with the hinge located at 0.70c.	70
43	Appendix-E : Diamond Joined wing (JWRA) rear wing airfoil polars	71
44	Appendix-E : Diamond Joined wing (JWRA) rear wing airfoil flap derivatives with the hinge located at 0.70c.	72

1	ASWING features comparison with modern most cited aeroelastic framework (A,S,AE,O) : Aerodynamic, Structure, Aeroelastic and Other features	12
2	Experimental evaluation cases 1/2. \mathcal{SA} = Steady Aerodynamics. (Git Repository: ISAE ASWING Validation)	23
3	Experimental evaluation cases 2/2. \mathcal{UA} = Unsteady Aerodynamics ; (Git Repository: ISAE ASWING Validation)	24
4	ClarkY wing parameters ($Re = 3E5$)	31
5	Swept forward and backward wings parameters ($\Lambda < 0$: swept forward)	38
6	Computational time comparison with higher fidelity methods adapted from the work of Fernandez-Escudero et al. (2019)	59

1 Introduction

 Ver the last three decades, the increase in computer power has led to the growing use of fast models for pre-design and geometry optimisation of unmanned aerial vehicles (UAVs) and commercial aircraft. In the future, both will be exposed to higher levels of gusts and turbulence due to climate change, and their design will have to take these predictions into account. Therefore, it is crucial to have a proper understanding of the aeroelastic phenomenon to optimize the flight envelope while minimizing the use of raw materials. As an aircraft/UAV manufacturer, ensuring good aerodynamic performance is essential to remain competitive in a growing market. Accurately predicting such a characteristic provides a significant advantage. Fast models can be a useful starting point for exploring ideas that can later be verified with higher fidelity methods.

ASWING is a software that was first released in 1999 ([Drela 1999](#) [2009](#) and [2008](#)) Specifically, ASWING can provide steady lift and drag predictions up to stall, as well as unsteady lift forecast. The software can capture the effect of ailerons and flaps, and take into account wake interference. It can also provide information on thrust and moment of propellers and their jets/swirl can be modelled so that their interactions with lifting surfaces can be captured. In terms of aeroelastic properties, the software can provide steady analysis such as torsional divergence, aileron reversal speed and wing washout. The prediction of structural deformation of wings and fuselage under steady and unsteady flow is also possible. Modal analysis can be used to predict flutter boundaries and divergence speed. The impact of nacelles, struts, structure tailoring, and propellers on the flutter speed can be investigated. Additionally, ASWING allows for the study of Limit Cycle Oscillations (LCO) as the model is fully non-linearly coupled. To provide these features, the unsteady nonlinear lifting line and slender body theory are coupled with a nonlinear extended Euler-Bernoulli beam model. Each lifting body is then connected to the others using compliant, elastic, or restrictive joints. Up to 40 lifting bodies, 10 engines, and 20 flaps can be implemented. ASWING is mainly dedicated to high aspect ratio geometries due to its formalism. This framework is used, for example, for designing High Altitude Long Endurance (HALE) UAVs.

Table 1 compares the main features of ASWING with other modern frameworks used in academia and industry. These include Openaerostruct, developed at the University of Michigan ([Jasa et al. 2018](#),[Chauhan and Martins 2019](#)), FNSA (Fast Nonlinear Static

Aeroelasticity) developed at Airbus and ISAE-SUPAERO ([Chandre Vila et al. 2022](#) and [2023](#)) and finally a no-name framework developed at Delft University ([Werter and De Breuker 2016](#)). The softwares are compared as they are derived from similar theories, namely potential methods extended with viscous loops for aerodynamics and Euler-Bernoulli/Timoshenko beam theory for structural modelling. They are also considered the best candidates for use in optimization work due to their low computational cost. The main ASWING disadvantage is that it is not coupled to the OPENMDAO planform. However, it is in early development at ISAE-SUPAERO. Despite these drawbacks, ASWING is in early development at ISAE-SUPAERO. The software is provided in a non-compiled version so that the user can modify it if necessary. However, ASWING lacks the benefits of an open-source community since the code cannot be published. Therefore, despite its combined features, ASWING is not widely used by the community. In fact, as shown in figure 1, ASWING has been cited a little less than 200 times since 1999. Nevertheless, it is mostly cited and presented as an existing tool. Upon closer examination of all publications, it is evident that ASWING has been utilised as an analysis and pre-design tool in 30 publications. However, only 6 of these publications presented a benchmark or validation of the tool against experimental and higher fidelity CFD data (cf the work of [Colas et al.](#), [González et al.](#), [Jones, Love et al.](#), [Variyar et al.](#), [Warwick et al.](#)). All six papers evaluated the same features: flutter speed or gust load predictions. Additionally, the aircraft considered in these papers were not stress cases of the model, as they all had high aspect ratio wings. Neither the original paper nor the technical documentation includes a section dedicated to code validation. Therefore, our main contribution is to provide experimental validation of the main features proposed by ASWING. In consideration of recent literature, updates have been made to the code and evaluated. The updated model will be referred to ASWING-m. To facilitate evaluation, the work has been divided into 4 parts: I - aerodynamics, II - propellers and jets, III - structure, and IV - aeroelasticity. The third motivation, following validation and modification, is to provide greater insight into the theoretical results used in the model. As stated by the author, this tool is primarily intended for individuals in the aircraft design community. But it can also be used by the control community, especially since the implementation of a modern control toolbox ([Jan et al. 2021](#)). Control engineers may not be familiar with all the theoretical advancements of ASWING and their limitations. Therefore, based on the validation results, the critical parameter limits are emphasised to ensure proper use of the tool. This report presents the first part of the experimental validation and modification of ASWING.

Table 1: ASWING features comparison with modern most cited aeroelastic framework (A,S,AE,O) : Aerodynamic, Structure, Aeroelastic and Other features

	ASWING	Openaerostruct	FNSA	Delft
Reference papers	[14], [15]	[27], [5]	[4] [3]	[47]
Non linear planform	✓	✓	✓	✓
3D Aerodynamic	✓	✓	✓	✓
Steady wake interaction	✓	NC	✗	NC
Propeller jet/wing interaction	✓	✗	✗	✗
A Fuselage modeling	✓	✗	✓	✗
Volume effect	✓	✗	✗ : QS	✓
Unsteady aerodynamic	✓	✗	✓	✗
Drag predictions	✓	✓	✓	✗
Flap/Ailerons effects	✓	✗	✗	✗
Steady-stall	✓	✗	✓	✗
Non-linear deflection	✓	✗	✗	✓
6-DOF	✓	✓	✓	✓
S Structural damping (unsteady)	✓	✗	✗	✗
Tension/elastic axis decoupling	✓	✗	✗	✓
Ponctual and concentrated mass effect	✓	✗	✗	✓
Wing box	✓ with [10]	✓	✗	✓
Steady deflection	✓	✓	✓	✓
Gust response	✓	✗	✓	✓
AE Torsional divergence	✓	✓	✓	✓
Structure failure	✓	✓	✗	✓
Ailerons reversal	✓	✗	✗	✗
Flutter analysis	✓	✗	✗	✓
Whirl flutter analysis	✓	✗	✗	✗
Limit cycle oscillations	✓	✗	✗	✗
O Embedded control toolbox	✓ [26]	✗	✗	✗
Open MDAO coupling	✗ In progress	✓	✗ In progress	✗
Opensource	✓	✓	✗ Airbus	✓

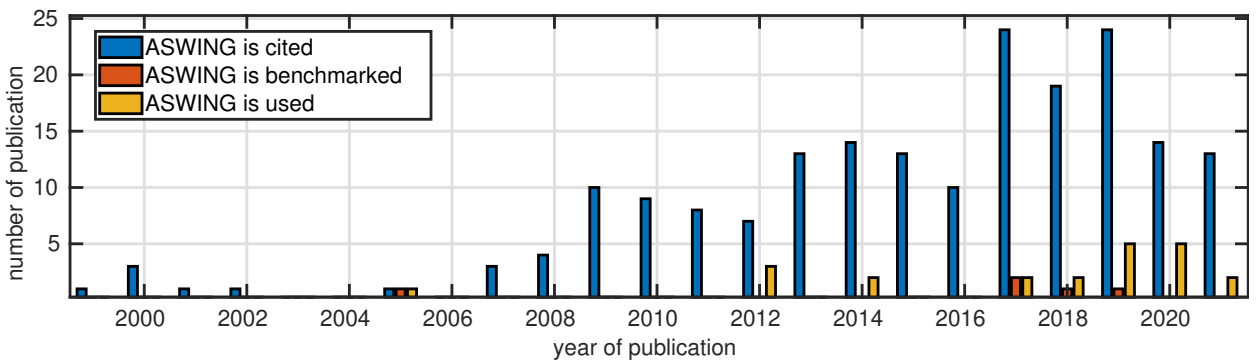


Figure 1: ASWING citation history, blue bars : mentioned as an existing tool; yellow : used as a tool ; orange : used and validated against experimental or higher fidelity CFD data

The focus is on the aerodynamic model. Firstly, the technical report recalls the nonlinear unsteady lifting line and slender body theories and introduces some modifications based on modern literature. Secondly, it proposes an experimental validation. It is important to note that no experimental campaign has been carried out. The dataset is a compilation of peer-reviewed data from journal articles, technical reports, and conference proceedings. It has been divided into two parts: I - steady and II - unsteady. The steady lift and drag predictions up to stall are presented for single and tandem layouts to evaluate the lifting line theory. Additionally, the effect of different ailerons is studied. The slender body theory is evaluated using four airships to highlight a numerical problem that arises from its implementation. A solution is proposed. Finally, the study evaluates 2D and 3D unsteady lift predictions for a plunging airfoil and a wing. The lift time, phase average, and first harmonic amplitude and phase are presented against various reduced frequencies, amplitudes, and root angles. Thirdly, this paper presents a computational time comparison between ASWING and higher fidelity methods to highlight its advantages. The paper concludes by discussing future theoretical developments and experimental validation.

2 The extended unsteady slender body theory

In ASWING there are 2 types of lifting bodies: wings and fuselage. Since the aeroelastic behaviour is of interest, the aerodynamic loads must be derived in a distributed form. To start with the fuselage, only fuselages with a local cross-section having a symmetry of revolution (circular) are considered. In this case, the unsteady distributed lift on a fuselage is given by the unsteady vector form of the slender body theory.

Theorem 2.1 (Extented SBT). *Let $R(s)$ be the cross-section radius at the spanwise location s . Let V and a_i be the air relative speed and local inertial acceleration evaluated at the cross-section centre. The local or distributed unsteady lift applied on an infinitesimal fuselage element of length ds is given by*

$$\begin{aligned} \frac{d\vec{L}}{ds} &= f_{lift} = 2\pi\rho V \cdot s \vec{V}_\perp R \frac{dR}{ds} - 2\pi\rho R^2 a_{i,\perp} \\ &= 2\pi\rho V \cdot s \vec{V}_\perp R \frac{dR}{ds} - 2\pi\rho R^2 (\vec{a}_i - (\vec{a}_i \cdot \vec{s}) \vec{s}) \end{aligned} \quad (1)$$

Proof. see Appendix B □

Note that \vec{V}_\perp and $a_{i,\perp}$ are the components of V and a_i lying in the cross-section plane as shown in

figure 2. The latter gives a visual insight into the aerodynamic lift direction and the effect of a positive or negative variation of R with respect to s on the steady lift. The second term in the equation 44 represents the unsteady components, also known as the added mass terms. It will be seen in the later section that the equation 44, as it is implemented numerically, can cause some instabilities. As the extended slender body theory is derived from potential methods, i.e. the inviscid assumption, ASWING recovers the viscosity effect using a semi-empirical equation. The elementary drag per unit length is then given by

$$f_{drag} = \frac{1}{2}\rho|\vec{V}|^2 2R c_{df} + \frac{1}{2}\rho|V_\perp|^2 2R c_{dp} \quad (2)$$

Note that in the expression 2 the different drag contributions do not have the same direction. In fact, as shown in the figure 2, the pressure drag acts in the direction of \vec{V}_\perp . From empirical data, the value of the pressure drag coefficient is usually between 0.4 and 1.2, depending on the nature of the flow. Skin friction drag, on the other hand, is applied in the direction of the upcoming flow \vec{V} . Assuming that the low velocity streamlines of the boundary layer are aligned with the free flow, so are the viscous shear stress efforts. The latter is shown in the upper right part of the figure 2

3 The extended non-linear lifting line model

3.1 Vectorial formulation of the unsteady Kutta-Joukowsky theorem

The unsteady aerodynamic loads on the wings are calculated using the extended nonlinear lifting line theory originally introduced by Prandtl and Glauert. The aerodynamic loads are divided into two contributions, circulatory and non-circulatory. The local unsteady circulatory lift is given by the unsteady vector form of the Kutta-Joukowsky theorem:

Theorem 3.1 (Unsteady Kutta-Joukowsky in its vectorial form). *Let Γ be a vortex line resulting from the vortex sheet lumping at the horseshoe boundary $r_{hv} = c/4$. The unsteady circulatory lift generated by an airfoil of chord c into a flow of velocity $V(r_{hv})$ is given by*

$$\begin{aligned} \vec{f}_{lift,\Gamma} &= \rho \frac{\partial \Gamma}{\partial t} c_\beta + \rho \Gamma (\vec{V} \times \vec{s}) \\ &= \rho c \frac{\partial \Gamma}{\partial t} \frac{(\vec{V} \times \vec{s})}{|V_\perp|} + \rho \Gamma (\vec{V} \times \vec{s}) \end{aligned} \quad (3)$$

Proof. see Appendix C □

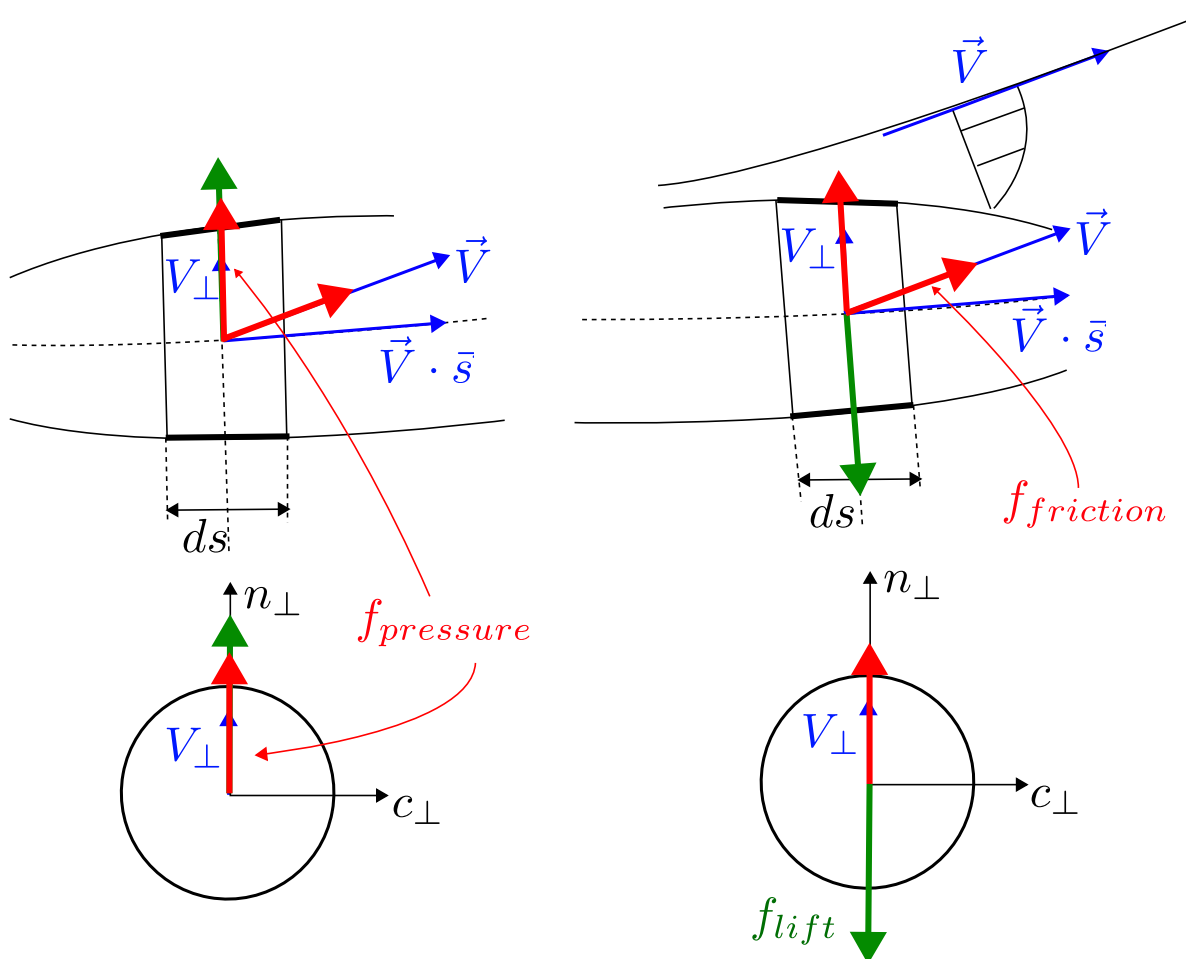


Figure 2: Slender Body Theory : lift and drag directions. The drag is split into 2 components : 1 - the pressure drag is always aligned with V_{\perp} and 2 - the skin friction drag aligned with the upcoming velocity V .

Note that c_β in equation 3 denotes the wind-aligned projected chord. In fact, as shown in figure 4 (a) and (b), the unsteady Kutta-Joukowsky theorem is integrated along the wake. Or the latter is wind-aligned in the ASWING model. The pressure integration must be performed over a corrected airfoil of length c_β (see Appendix C for more details). In the equation 3 Γ is unknown and distributed along the span. As will be seen in the velocity influence section, it is represented by a finite Fourier transform where the coefficients are unknown. Therefore, an appropriate set of constraints must be established to calculate them. Non-circulatory lift, i.e. source/sink lift, also known as an added mass effect, is provided by an approximation of Theodorsen's theory.

Theorem 3.2 (Theodorsen : apparent mass terms). *The unsteady lift and momentum due to a source/sink distribution ensuring the impermeability condition over the entire airfoil is given by*

$$\vec{f}_{am} = \frac{\pi}{4} c^2 \left[\vec{V} \times (\vec{\Omega} + \vec{\omega}_i) \cdot \vec{n} - a_{c/2} \cdot \vec{n} \right] \cdot \vec{n} \quad (4)$$

$$\begin{aligned} \vec{m}_{am} = & \\ & - \frac{\pi}{4} c^2 \frac{c}{4} \left[\vec{V} \times (\vec{\Omega} + \vec{\omega}_i) \cdot \vec{n} + \frac{c}{8} (\alpha_0 + \dot{\omega}_i) \cdot \vec{s} \right] \cdot \vec{s} \quad (5) \\ & + \Delta r_{c/2} \times \vec{f}_{am} \end{aligned}$$

Proof. see (Theodore Theodorsen 1935). It is important to note that the equations 4 and 5 are a vectorial formulation of Theodorsen's theory. Moreover, they do not exactly reproduce the results proposed in 1935. In fact, the airfoil is assumed to pitch and plunge around the mid chord, which is more conservative. \square

3.2 Modelling drag

As the lifting line and Theodorsen are inviscid theories, viscosity effects are recovered using 2D airfoil polars. In consequence, the distributed drag generated over a wing is locally given by :

$$\begin{aligned} \frac{d\vec{D}}{ds} = \vec{f}_{drag} = & \frac{1}{2} \rho |\vec{V}| \vec{V} \bar{c} c_{df} + \frac{1}{2} \rho |\vec{V}_\perp| \vec{V}_\perp \bar{c} c_{dp} \\ & + 2\rho \frac{\vec{V}_\perp}{|\vec{V}_\perp|} (\vec{V} \cdot \vec{n})^2 c_p \quad (6) \end{aligned}$$

In equation 6 the first term is the skin friction drag contribution, aligned with the free stream velocity (figure 3-a). As in slender body theory, the streamlines in the boundary layer are assumed to be aligned with the upcoming free stream, as shown in figure 3 (b). The second term implies that the pressure drag contribution lies in the cross-sectional plane (as the lift) (figure 3-a). Finally, the third term appears only

at stall and is also in the cross-section plane. Note that c_{df} and c_{dp} can be obtained from higher fidelity methods or experimental data for any airfoil used on a wing. However, in the equation 6 the latter are considered to be constant. This simplification was made because lift-induced drag is usually more important than skin friction/pressure drag. This assertion is true for high Reynolds number flow, but in the case of mini UAV design (low Reynolds number flight), errors in the prediction of drag should be observed.

3.3 Aerodynamic moment

The distributed aerodynamic moment applied to a lifting surface is the sum of the lift and airfoil pitch moment coefficient contributions. Note that drag has been omitted because it is mostly chord-wise (the moment arm is small). Furthermore, its amplitude is usually much smaller than that of the lift.

$$\vec{m}_{lift} = \Delta \vec{r}_{hv} \times \vec{f}_{lift} + \frac{1}{2} \rho \left| \vec{V}_\perp \right|^2 \bar{c}^2 c_m \hat{s} \quad (7)$$

with the pitching moment coefficient and its flap-induced shift given as

$$c_m = \left(c_{m0} + \frac{dc_m}{d\delta_{F_1}} \delta_{F_1} + \frac{dc_m}{d\delta_{F_2}} \delta_{F_2} \dots \right) \frac{1}{\sqrt{1 - M_\perp^2}} \quad (8)$$

The linear shift of the pitching moment is valid for reasonable flap deflections as illustrated in Appendix C. The Prandtl-Glauert factor uses the local perpendicular Mach number $M_\perp = \left| \vec{V}_\perp \right| / V_{sound}$ to take into account the compressibility effects.

3.4 Extented Kutta-Joukowsky condition

The extended Kutta condition serves several purposes in ASWING. Firstly, it imposes physical constraints on the circulation Fourier coefficients in order to build a good constraint system of equations. Secondly, it recovers the 2D airfoil properties such as the linear lift slope cl_α , the camber line α_0 and the effect of flaps. Thirdly, it recovers the unsteady effect using a lag term that brings reasonable consistency with Theodorsen's circulatory lift.

To do this, for each circulation Fourier coefficient, a flow tangency condition is imposed on the airfoil at each "control point" location. In other words, the local velocity evaluated at this point must be parallel/tangent to the surface of the airfoil, as shown in figure 4(d). However, because of the ASWING formalism, the Kutta-Joukowsky condition has been modified.

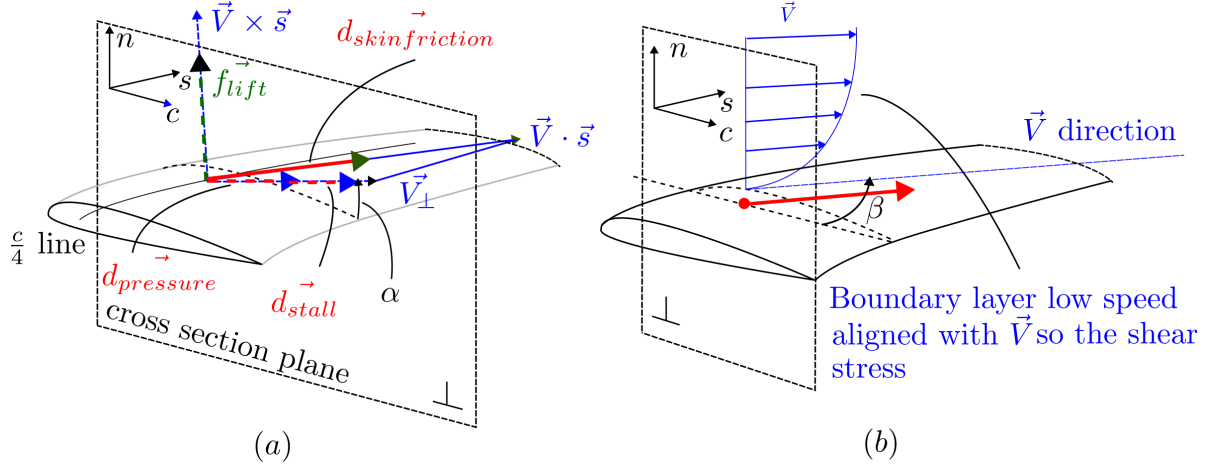


Figure 3: ASWING lifting line forces directions
 (a) 3D directions of lift and drag contributions
 (b) zoom on the boundary profile low-speed profile

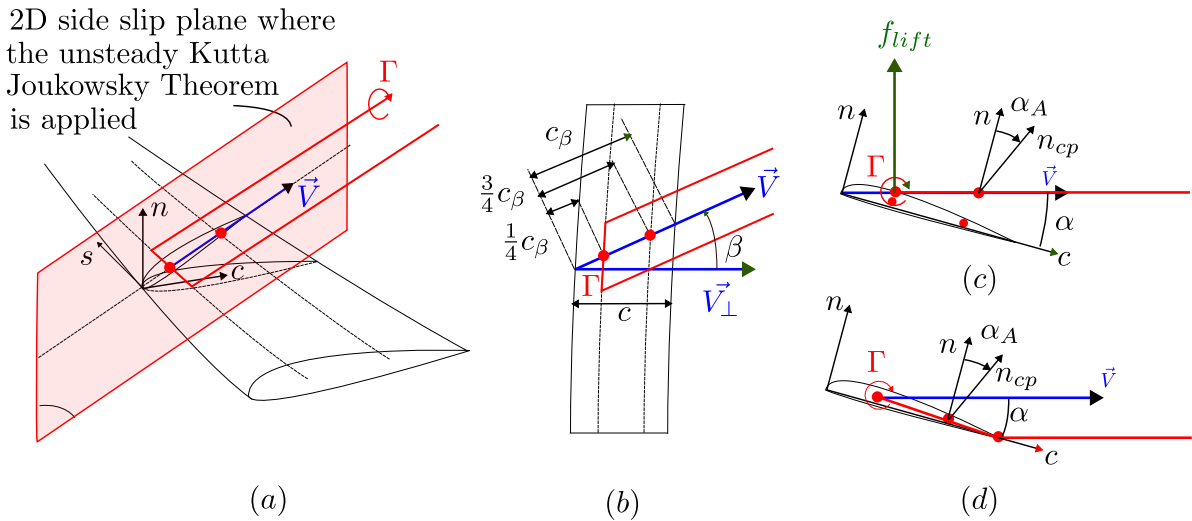


Figure 4: ASWING horseshoe representation
 (a) 2D Kutta Joukowski plane
 (b) top view with corrected chord c_β
 (c) ASWING wake straight shedding
 (d) Modern literature horseshoe representation

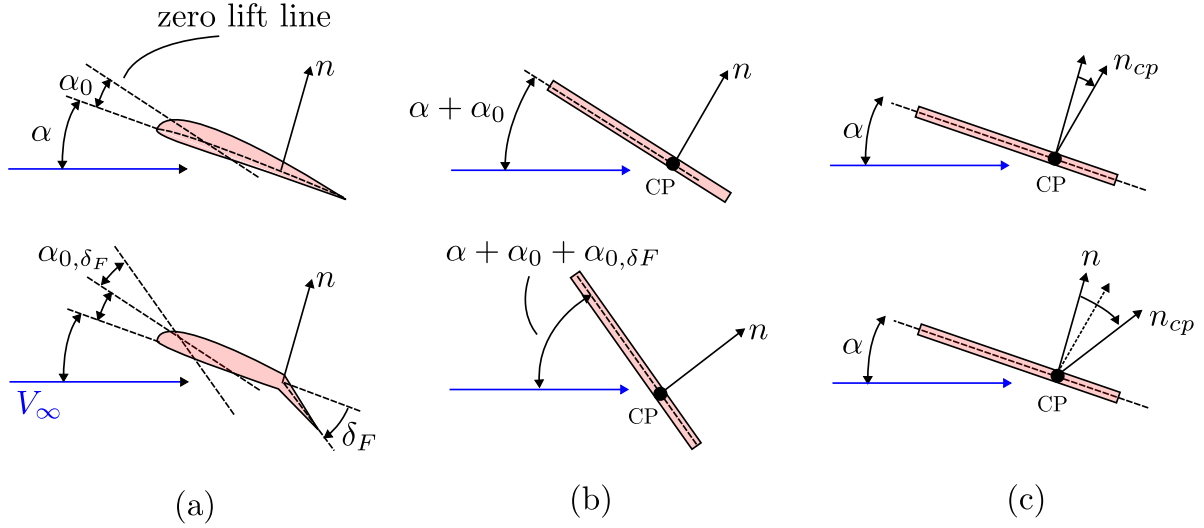


Figure 5: Recovering airfoil camber line (first line) and flap deflection effect (second line):

First, as shown in figure 4 (c), the wake is shed directly from the centre of pressure (quarter chord) and no longer from the trailing edge. As the control point must be placed on the vortex sheet, it is no longer part of the wing geometry. Secondly, as the wake is wind-aligned, the position of the centre of pressure and control point varies with the upcoming freestream direction. Criticism of this horseshoe representation has been made in (Chreim 2019). Stability issue and a lack of 'physical' meaning as the wake is not shed from the trailing edge have been reported. However, in our validation work, we did not observe such instabilities related to the wake representation. Furthermore, although the second argument is valid, at high aspect ratios the difference in wake position between the two representations is negligible. The ASWING representation has the advantage of having a direct vectorial solution for the vortex-induced velocities, while the second requires the computation of the contribution of a vortex ring and a horseshoe vortex, which increases the computational time. The horseshoe boundary or centre of pressure and the control point are placed at a distance of $\frac{1}{4}c_\beta$ and $(\frac{1}{4} + h)c_\beta$ respectively along the wind-aligned unit vector $\vec{\xi} = \frac{\vec{V}_\infty}{|\vec{V}_\infty|}$ from the leading edge of the wing. The meaning of h will be derived in the next lines. If \vec{r}_{cp} is given as the local position of the control point. The flow tangency condition is written as follows.

$$\vec{V}(\vec{r}_{cp}) \cdot \vec{n}_{cp} = 0 \quad (9)$$

where $\vec{V}(\vec{r}_{cp})$ is the air relative velocity evaluated at the control point. The latter depends on the body motion, the velocity induced by the horseshoe vortices, the sources, the doublets, the engine jet and the gust. The position of the control point is wisely chosen in order to recover the linear incompressible lift airfoil slope $c_{l,\alpha}$. In fact, if the position of the control point

is defined as :

$$\vec{r}_{cp} = \vec{r}_{hv} + \frac{h\bar{c}}{|\vec{\xi} \times \hat{s}|} \vec{\xi} = hc_\beta \hat{\xi} = \frac{1}{4\pi} \frac{dc_l}{d\alpha} c_\beta \vec{\xi} \quad (10)$$

when the Kutta condition is solved to compute the circulation and combined with the lift theorem, the latter is given by

$$f_{lift} = \frac{1}{2} \rho c l_\alpha \alpha_{eff} V_\infty^2$$

recovering the airfoil lift slope on the local lift. 2 other airfoil properties can be recovered by modifying the flow tangency condition. Indeed, let us introduce the zero lift angle of attack and its linear shift induced by the deflected flap defined as

$$\alpha_A = \alpha_0 + \frac{dc_l}{d\delta_{F_1}} \frac{d\alpha}{dc_l} \delta_{F_1} + \frac{dc_l}{d\delta_{F_2}} \frac{d\alpha}{dc_l} \delta_{F_2} + \dots \quad (11)$$

where α_0 is the zero lift angle of attack of the airfoil, $\frac{dc_l}{d\delta_{F_1}} \frac{d\alpha}{dc_l}$ is the linear shift slope induced by a flap placed on the airfoil. The linearity of the shift as for the pitch momentum is valid for reasonable small flap deflections as shown in Appendix C. It is possible to consider more than 1 flap per airfoil, but this is very unlikely to be used on a UAV.

As shown in the figure 5 these airfoil parameters can be recovered by tilting the normal vector of the flow tangency condition by the angle α_A . This tilting is the only way to achieve compatibility with the structural model as the structure cannot be virtually deformed to match the airfoil properties as shown in the second line of figure 5. The flow tangency condition is then rewritten as

$$\vec{V}(\vec{r}_{cp}(c_{l_\alpha})) \cdot \vec{n}_{cp} (\alpha_0, d\alpha/d\delta_{F_1}) = 0 \quad (12)$$

The airfoil local stall is caught through the use of the

lift slope decambering function in the flow tangency condition

$$\vec{V}(r_{cp}(c_{l_\alpha})) \cdot n_{cp}(\alpha_0, d\alpha/\delta F_1) - \frac{V_\perp}{4\pi h} K_s f_{\text{stall}}(c_l, cl_{min}, cl_{max}) = 0 \quad (13)$$

with $c_l = \frac{2\Gamma}{cV_\perp}$ the 2D lift coefficient and $f_{\text{stall}}(c_l, cl_{min}, cl_{max})$ the stall activation function defined as

$$f_{\text{stall}}(c_\ell) = \Delta c_\ell \log \frac{1 + \exp[(c_\ell - c_{\ell \max})/\Delta c_\ell]}{1 + \exp[(c_{\ell \min} - c_\ell)/\Delta c_\ell]}$$

Note that $K_S = 40$ and $\Delta c_l = 0.05$ have been empirically chosen to match pre-stall usual behaviour. Finally, a 2D unsteady approximation of the wake is used leading to the final modification of the flow tangency condition.

$$\vec{V}(r_{cp}(c_{l_\alpha})) \cdot n_{cp}\left(\alpha_0, \frac{d\alpha}{d\delta F_1}\right) - \frac{V_\perp}{4\pi h} K_s f_{\text{stall}}(c_l, cl_{min}, cl_{max}) - \frac{b}{V_\perp} \frac{\partial \Gamma}{\partial t} = 0 \quad (14)$$

This lag term is claimed by the author [14] to be the best temporal fit possible to the Theodoren theory. Indeed when the full aerodynamic model is translated into the frequency domain, it is possible to build a lift coefficient transfer function defined as

$$C_{\text{ASWING}}(k) = (F + iG)_{\text{ASWING}} = \frac{1 + 2ik}{1 + 4ik} \quad (15)$$

which is graphically compared to the Theodorsen circulatory lift function in figure 6. ASWING lag function seems to be weak to reproduce the Theodorsen's for reduced frequency between 0 and 1. This range is of particular interest in the experimental validation sections.

3.5 Velocity influence of lifting bodies

As it has been seen, the air relative speed is needed to compute the lift and drag in both LLT and SBT. As described earlier the latter is the summation of different contributions, as follow

$$\vec{V}(\vec{r}) = \vec{V}_\infty - \vec{\Omega} \times \vec{r} + \vec{V}_{ind}(\vec{r}) + \vec{V}_{gust}(\vec{r}) \quad (16)$$

In this section, the velocities induced by the singularities used in the SBT and LLT ie doublets, sources, and vortices are derived.

Prandtl Glauert Transformation

The singularities induced velocities are computed in the Prandtl Glauert space through the use of the

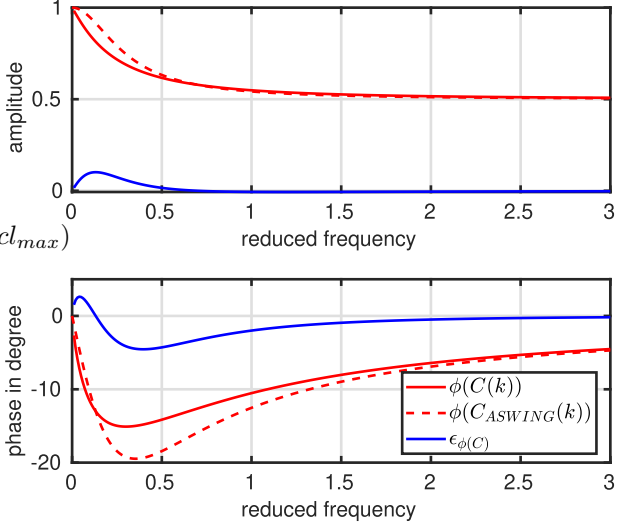


Figure 6: Modulus and phase comparison of Theodorsen and ASWING lag function

following transformation (PGT)

$$\begin{aligned} \bar{P} &= \begin{bmatrix} \dots \vec{\xi} \dots \\ \dots \hat{\eta} \dots \\ \dots \hat{\zeta} \dots \end{bmatrix} \\ &= \begin{bmatrix} \frac{1}{\lambda} \cos \alpha \cos \beta & -\frac{1}{\lambda} \sin \beta & \frac{1}{\lambda} \sin \alpha \cos \beta \\ \cos \alpha \sin \beta & \cos \beta & \sin \alpha \sin \beta \\ -\sin \alpha & 0 & \cos \alpha \end{bmatrix} \end{aligned} \quad (17)$$

where α , β , and λ are the angle of attack, side slip angle, and compressibility stretching factor. The PGT has mainly 2 purposes. Firstly to provide a direct vectorial solution of the horseshoe vortices induced velocity. The second is to take into account the compressibility effect using the stretching factor λ .

Vortex influence function

Let us consider an aircraft having N_w wings (lifting surfaces) and its j^{th} wing. Its circulation spanwise distribution is given by the Fourier series

$$\begin{aligned} \Gamma_j(s) &= \sum_{k=1}^{K_j} A_{k,j} \sin(k \arccos(s/s_{\max})) \\ &= \sum_{k=1}^{K_j} A_{k,j} \sin(k\theta) \end{aligned} \quad (18)$$

where $A_{k,j}$ are the Fourier coefficients associated with the j^{th} wing, K_j is the number of coefficients, s is the wing spanwise coordinate, and s_{\max} its maximum value (usually close to the wing half span). Equation 18 is very convenient as it is continuous in s . As a consequence, it can be directly used in equation 3 to compute the local lift. $\frac{\partial \Gamma(s)}{\partial t}$ is numerically computed using a first order backward difference. Let us consider now that the j^{th} wing has been discretized in I_j structural nodes. The wing wake is represented by a discrete horseshoe system associated with the struc-

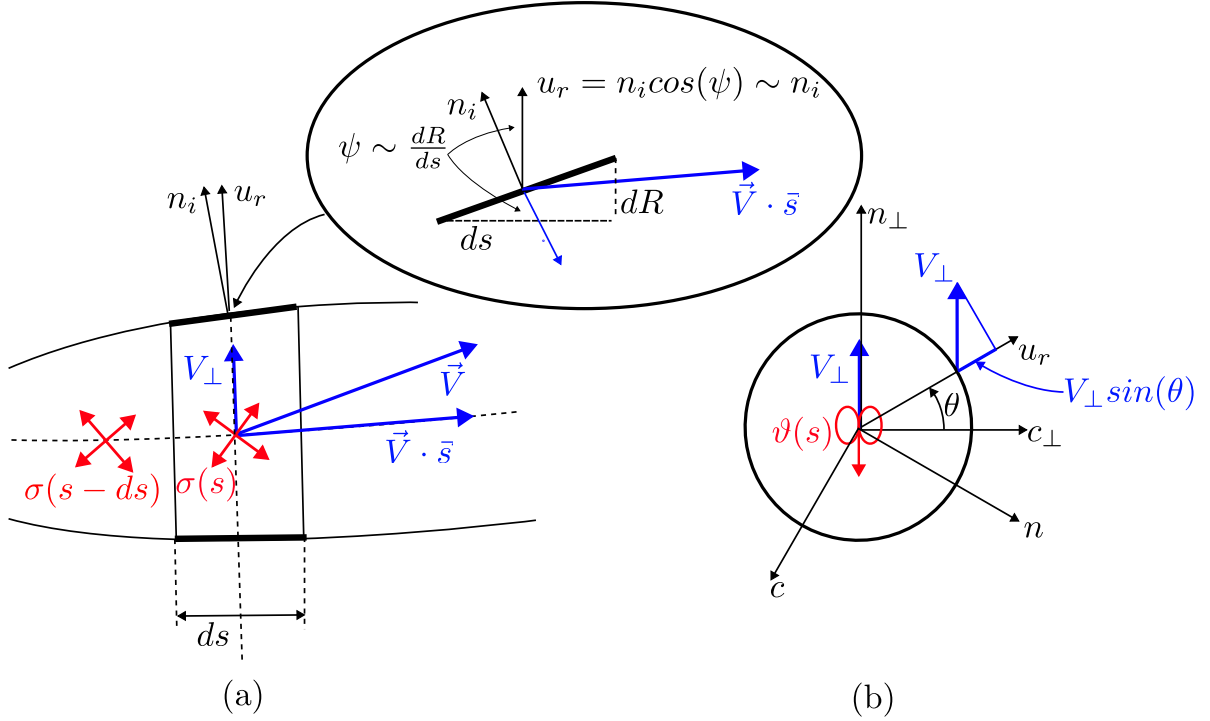


Figure 7: Slender Body Theory: Flow field modelling with source/sink and doublet distribution, 2D simplification of the problem.

tural mesh. Each discrete horseshoe has a circulation of strength $\Gamma_j(s_{a,i})$

$$\begin{aligned}\Gamma_j(s_{a,i}) &= \Gamma_j(\theta_{a,i}) \\ &= \sum_{k=1}^{K_j} A_{k,j} \sin(k \arccos(s_{a,i}/s_{max})) \\ &= \sum_{k=1}^{K_j} A_{k,j} \sin(k\theta_{a,i})\end{aligned}\quad (19)$$

where $s_{a,i} = \frac{1}{2}(s_{i+1} - s_i)$ is the spanwise averaged position of the discrete circulation segment. The velocity induced by the i^{th} horseshoe is given by the Biot Savart's law

$$\begin{aligned}V_{\Gamma_{j,i}}(\vec{r}) &= [P]^T \left[\sum_{k=1}^{K_j} A_{k,j} \sin(k\theta_{a,i}) \right] \\ &\quad \frac{1}{4\pi} \oint_{\Gamma_{j,i}} \frac{\vec{\delta}_i(\vec{r}) \times d\vec{l}_i}{\delta_i(\vec{r})^3}\end{aligned}\quad (20)$$

In the above equation, the integrand has a vectorial solution that can be found in equation (6.33) of (Drela 2014). The latter can be desingularized when the i^{th} horseshoe legs cross the position of a point where the local velocity must be computed. The denominator of the integrand is then replaced by $(\delta_i^2 + \epsilon_i)^{3/2}$ with $\epsilon_i = c_{a,i}/4$. The velocity induced by the j^{th} wing horseshoe system is then given by summing the contribution of

each horseshoe vortices.

$$\begin{aligned}V_{\Gamma_{j,i}}(\vec{r}) &= [P]^T \sum_{i=1}^{I_j-1} \left[\sum_{k=1}^{K_j} A_{k,j} \sin(k\theta_{a,i}) \right] \\ &\quad \frac{1}{4\pi} \oint_{\Gamma_{j,i}} \frac{\vec{\delta}_i(\vec{r}) \times d\vec{l}_i}{\delta_i(\vec{r})^3}\end{aligned}\quad (21)$$

The latter equation is not very convenient to compute the $A_{k,j}$ coefficients using the Kutta condition. By noticing that the latter does not depend on structural index i they can be set outside of the i summation. The velocity induced by the j^{th} wing can be rewritten as follows

$$\begin{aligned}V_{\Gamma_{j,i}}(\vec{r}) &= \sum_{k=1}^{K_j} A_{k,j} v_{k,j}(\vec{r}) \\ &= \sum_{k=1}^{K_j} A_{k,j} \\ &\quad \left[[P]^T \sum_{i=1}^{I_j-1} \sin(k\theta_{a,i}) \frac{1}{4\pi} \oint_{\Gamma_{j,i}} \frac{\vec{\delta}_i(\vec{r}) \times d\vec{l}_i}{\delta_i(\vec{r})^3} \right]\end{aligned}\quad (22)$$

where $v_{k,j}$ can be interpreted as the velocity induced by the k^{th} Fourier coefficient of the j^{th} wing circulation function. The total velocity induced by the N_w lifting surfaces is then given by

$$V_{\Gamma}(\vec{r}) = \sum_{j=1}^{N_w} V_{\Gamma_j}(\vec{r}) = \sum_{j=1}^{N_w} \sum_{k=1}^{K_j} A_{k,j} v_{k,j}\quad (23)$$

which now defines a solvable set of equations when integrated into the Kutta condition. The Kutta condition must be applied $K = \sum_{j=1}^{N_w} K_j$ times, corresponding to the number of Fourier coefficients to be computed. Describing the circulation distribution as a finite Fourier transform instead of a piecewise one drastically reduces the number of unknowns in the system. It also allows the aerodynamic model to be decoupled from the structural model. As the discrete horseshoe system is related to the structural one, the wake would be particularly refined despite the small number of Fourier coefficients.

Volume influence function

The velocity induced by the sources and doublets distributions used (cf figure 7) in the slender body theory is given by.

$$\vec{V}_\sigma(\vec{r}) = V_\infty [P]^T \left(\frac{1}{4\pi} \sum_{k=1}^{N_\sigma} \frac{\sigma_k \vec{\delta}_k(\vec{r})}{(\vec{\delta}_k^2 + \epsilon_k^2)^{3/2}} \right) \quad (24)$$

where N_σ is the number discrete sources used in the SBT and $\vec{\delta}_k$ the relative position vector to the k^{th} source. σ_k is the strength of the sources placed at the position \vec{r}_k . To avoid any numerical divergence, each source has an associated desingularizing core $\epsilon_k = R(r_k)/2$. Similarly, the flow field induced by a doublet distribution is given by

$$\vec{V}_\vartheta(\vec{r}) = V_\infty [P]^T \left(\frac{1}{4\pi} \sum_{k=1}^{N_\vartheta} \frac{\vartheta_k \vec{\delta}_k^2 - 3(\vec{\vartheta}_k \cdot \vec{\delta}_k) \cdot \vec{\delta}_k}{(\vec{\delta}_k^2 + \epsilon_k^2)^{3/2}} \right) \quad (25)$$

In practice $N_\vartheta = N_\sigma$ so equations 24 and 25 can be merged. Appendix A gives an insight into the role of sources and doublets in the slender body theory and how their strengths σ_k and ϑ_k are computed. Induced velocity functions allow us to recover the close interaction between lifting bodies and take into the 3D effects on the aerodynamic forces (wake downwash). In consequence, the total induced velocity can be defined using equation 25, 24, and 23 as follows

$$\vec{V}_{ind}(\vec{r}) = V_\Gamma(\vec{r}) + \vec{V}_\sigma(\vec{r}) + \vec{V}_\vartheta(\vec{r}) \quad (26)$$

Modelling Ground Effects:

During take-off and landing, an aircraft flies quite close to the ground, where strong aerodynamic effects such as an increase in lift and a reduction in drag can be observed (Recant. 1939). The ground acts as a solid surface where the impermeability condition must be respected. As a consequence, the flow field around the aircraft is drastically modified if it is close enough to the ground. In ASWING, the ground is considered as an infinite flat oriented plane. In order to ensure the impermeability condition over the entire ground

plane, a system of symmetric vorticity, source and doublet is created, whose intensity is equal in absolute value to maintain the same number of variables in the system. Figure 8 shows how such a system is constructed for a solid ground. The predictions of the ground effects are evaluated in the following sections ¹.

4 ASWING aerodynamic model improvements

This section describes the various improvements made to the ASWING model. From now on the modified model will be called ASWING-m. The most important aerodynamic improvements are described below:

1 - Improvements in drag prediction:

The ASWING source code has been modified to allow the polar to vary with angle of attack and Reynolds number. A polar lookup table for each airfoil used on the wing is provided to ASWING. Then, during the time marching or steady state computation, the lookup table is interrogated at each spanwise location based on the local angle of attack and Reynolds number. Note that no convergence problems are expected as the variation of the polar is convex with α . The Watchdogs routines have been coded so that if the Reynolds number is outside the boundary set of the lookup table, the polars are stops at the bounds to avoid their divergence. This is of particular interest for elliptical wings where the local chord is zero at the tip, so the Reynolds number is. The wing drag equation is then rewritten as follows

$$\begin{aligned} \frac{d\vec{D}}{ds} &= \frac{1}{2} \rho |\vec{V}| \vec{V} \bar{c} c_{df}(\alpha, Re) + \frac{1}{2} \rho |\vec{V}_\perp| \vec{V}_\perp \bar{c} c_{dp}(\alpha, Re) \\ &\quad + 2\rho \frac{\vec{V}_\perp}{|\vec{V}_\perp|} (\vec{V} \cdot n)^2 c_p \end{aligned} \quad (27)$$

2 - Pre-stall viscous de-cambering: During the validation analysis, we observed that ASWING does not accurately capture the lift for a high angle of attack, especially at a low Reynolds number. This discrepancy is mainly due to the linear lift assumption. Since cl_α is assumed to be constant, it can introduce errors in the lift predictions, depending on the quality of the linear regression of the lift polar. Consequently, we have implemented a vicious loop to calculate a new "decambered" lift slope at a high angle of attack based on the XFOIL viscous polar provided to ASWING-m. We also added a dependence on the Reynolds number

¹A second type of ground exists in ASWING (free-surface) but is not presented here

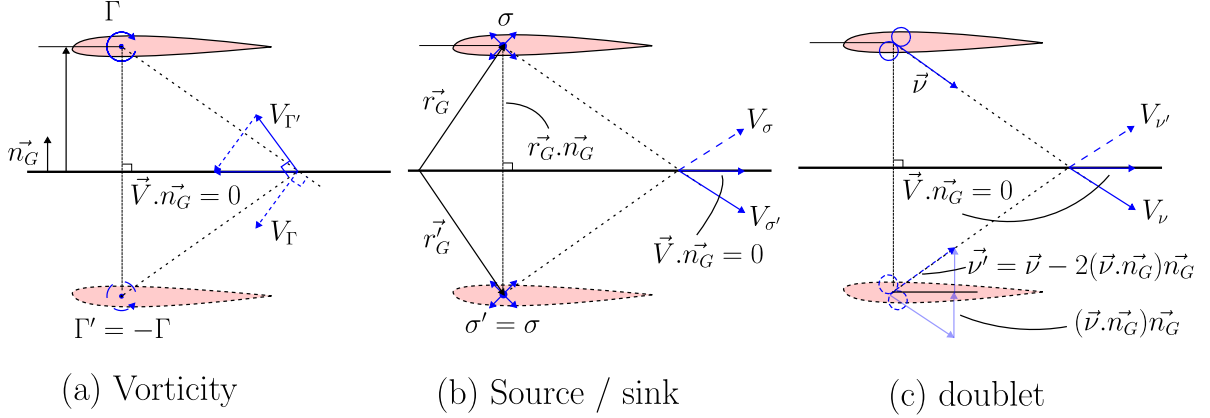


Figure 8: Ground effect modelling in ASWING

to more accurately capture the variation of airfoil lift across the flight envelope.

3 - Airfoil parameter dependence on Reynolds number:

Some of the airfoil parameters vary with the Reynolds number, such as the cl linear slope. Among them, cl_{min} , cl_{max} , α_0 , $d\alpha_0/d\delta F$ and $dc_m/d\delta F$ can vary quite significantly as illustrated in Appendix C. As a result, the source code was modified. At each Newton iteration during the time marching calculation, the Reynolds number is calculated at each spanwise location. The airfoil parameters are changed accordingly using pre-computed single-entry lookup tables. This brings a degree of convenience to any aircraft analysis on its flight envelope.

4 - Shift of stall limits due to flap deflection:

This change is motivated by the analysis presented in Appendix C. For a positive deflection, cl_{max} and cl_{min} are positively shifted as follows

$$\begin{aligned} cl_{min}(\delta_F) &= cl_{min} + cl_\alpha \frac{d\alpha_0}{d\delta F} \delta_F \\ cl_{max}(\delta_F) &= cl_{max} + cl_\alpha \frac{d\alpha_0}{d\delta F} \delta_F \end{aligned} \quad (28)$$

This modification should provide more accuracy for wing washout and flap effectiveness analysis. Unfortunately, no experimental data were found to evaluate this modification. Improvements 1 to 3 are evaluated against ASWING in the following sections.

5 Numerical mesh convergence, aliasing and stability analysis

The convergence of the numerical scheme for 3D lift prediction was evaluated against the Prandtl theoretical solution for 3 different angles of attack. The wing considered was elliptical. As shown in figure 9, all configurations converge quite quickly to their respective theoretical solutions. Therefore, discretising a wing with 20 to 40 circulation variables (or Fourier coefficients) seems to be a reasonable choice. The study of the lift convergence is sufficient to infer the drag and pitch moments. In fact, both depend on the flow field formed by the horseshoe vortex system. The aerodynamic moment also depends on the lift. Since the lift is given by the circulation distribution, when the latter has numerically converged, so will the induced flow field and thus the drag and the aerodynamic pitching moment.

During the later analysis, instabilities were observed for the elliptical wing. As the chord tends to zero towards the wing tip, so does the singularizing core of the horseshoe vortex. As the structural model is discretised by a cosine clustering function, the distance between the control point and the legs of the horseshoe becomes smaller and smaller towards the wing tip. This results in a singular calculation of the velocity. However, this is not actually a problem, as the solution converged for a much smaller number of nodes than the one where this phenomenon is observed (40 against 400).

Finally, aliasing effects were observed on the post-processed data from the ASWING output files. This artefact is illustrated in figure 10 (a). This problem originates in the writing of the output files. In fact, in the ASWING source code, it is possible to assign a certain number of decimal places to each characteristic output value. Therefore, after identification, the

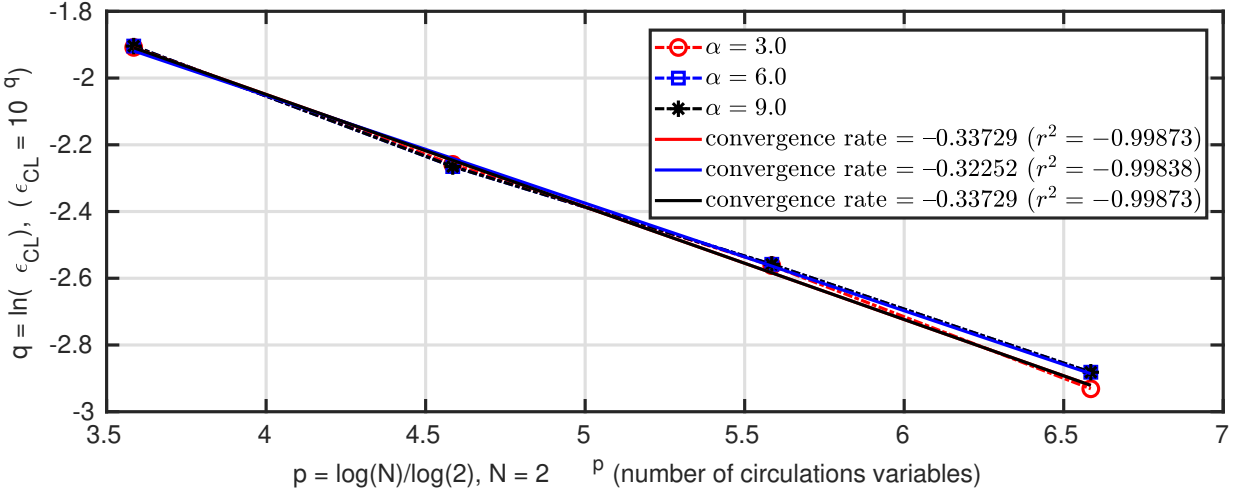


Figure 9: Numerical scheme relative convergence to theoretical Prandtl's solution (inviscid case)

spatial quantities are returned with 2 decimal places. This problem can be solved by a simple modification of the source code (see figure 10-b). Note that this problem is accentuated for particularly refined meshes, as the cosine clustering function tends to produce a very fine mesh towards the wing tip.

6 Experimental validation

This section presents an experimental/CFD² validation of ASWING. An important focus is placed on the steady aerodynamics. Through the use of 6 cases, single planforms have been selected to stress the non-linear lifting line model. Case number 1 is an academic rectangular planform where C_L and C_D predictions up to stall have been investigated. Case number 2 is a 45° swept-back wing, chosen mainly to evaluate the vector formulation of drag and lift. Cases 3 and 4 are chord-varying swept and unswept wings. The fifth case is a 45° dihedral angle wing chosen to virtually reproduce a highly deflected wing. The effects of aileron deflection are then investigated on a straight wing (6th case). Rolling and yawing moments induced by deflected ailerons are studied. Thirdly, 2 tandem cases are presented. Both were chosen to test the ability of the ASWING to consider wake interactions. Two cases were necessary to evaluate both the lift and drag of each planform up to stall. Note that for each case we have tried to find a platform with the lowest aspect ratio possible. In the next section, the reader will have a complete detail of each case experimental/CFD bench and its ASWING equivalent parameters. The slender body theory is evaluated with 4 different airship cases. Note that the latter have been chosen more to highlight a numerical prob-

lem arising from the ASWING model than to validate the slender body theory. The second part is entirely dedicated to 2D and 3D unsteady aerodynamics. Each steady (\mathcal{SA}) and unsteady (\mathcal{UA}) case and its purpose are summarised in the tables 2 and 3. If the reader want to reproduce these case, a Git repository has been created that contain all the cases simulation files and experimental data. For some (specified in tables 2 and 3) only partial repeatability is possible. This is because we had to modify the source code of Aswing to perform them. The latter is not allowed to be diffused publicly (please refer to Aswing License). For these cases, the reader will find the only Aswing output data in the repository. This might be useful for comparison with other aeroelasticity codes. The repository can be found here : [Git Repository: ISAE ASWING Validation](#)

6.1 Steady non-linear lifting line validation (Cases SA-1 to 12)

CASE SA-1: Straight Wing

The first case chosen is a straight wing tested and presented in the work of (Applin 1995). The experiments were carried out in Langley's 14 by 22-foot subsonic wind tunnel. The wing model was mounted vertically on a six-component strain gauge balance. The wing span is 116 inches (2.95m) and the chord is 39.37 inches (1.0m). The airfoil selected was a NACA0012. The wing was deliberately made rigid to avoid any aeroelastic phenomena. The boundary layer transition was forced by the use of strips located on the upper and lower surfaces. Their position (assumed to be the same as the transition) was 2 inches from the leading edge (0.05c). Pressure measurements were taken on the upper and lower surfaces

²higher fidelity CFD : URANS, LES, etc

Table 2: Experimental evaluation cases 1/2. \mathcal{SA} = Steady Aerodynamics. (Git Repository: [ISAE ASWING Validation](#))

CASE	Geometry	Exp data	Evaluation type	Repeatability
$\mathcal{SA}-1$	Straight wing	[1]	Baseline case (C_L and C_D up to stall)	Full
$\mathcal{SA}-2$	45° swept back	[24]	Non linear scheme drag formalism evaluation (C_L and C_D)	Full
$\mathcal{SA}-3$	Elliptical wing	[41]	Chord varying planform (C_L and C_D)	Full
$\mathcal{SA}-4$	Crescent wing	[41]	Non linear scheme evaluation	Full
$\mathcal{SA}-5$	45° dihedral wing	CFD	Non linear scheme evaluation (C_L and C_D)	Full
$\mathcal{SA}-6$	Straight wing	[22], [23]	Rolling and Yawing moments induced by various ailerons	Full
$\mathcal{SA}-7$	Tandem 1	[19], [19]	Wake interference (C_L and C_D)	Full
$\mathcal{SA}-8$	Tandem 2	[6]	Wake interference (C_L up to stall)	Full
$\mathcal{SA}-9 \text{ A-E}$	5 Swept forward, and backward wing	[33], [42]	lift loading distribution ($c_l c$), center of pressure spanwise location y_p	Full
$\mathcal{SA}-10$	Straight wing with, winglet and tip sails	[34]	effect of tip devices on, lift and drag (C_L, C_D)	Full
$\mathcal{SA}-11$	Swept back wing with, Whitcomb winglet	[25] [2]	discussion on transonic flight, limits of ASWING	Full
$\mathcal{SA}-12 \text{ A-B}$	Rectangular wing with plain and slotted flaps	[36]	ground effects on lift and drag, (C_L, C_D) of a rectangular wing with flaps	Full
$\mathcal{SA}-13 \text{ A-D}$	Airships / fuselages	[44]	Slender Body Theory validation lift and pressure ($c_l(s), q(s)$) distribution on 4 airships	Partial
$\mathcal{SA}-14$	45 degrees swept back wing with fuselage	[32]	Wing body interference: local and total lift (c_l, C_L) effect with and without body	Full
$\mathcal{SA}-15$	Diamond joined wing	[37]	Longitudinal characteristics (C_L, C_D, C_M) and control ($C_L(\delta_E), C_M(\delta_E)$) of diamond joined wing with variable joint location	Full

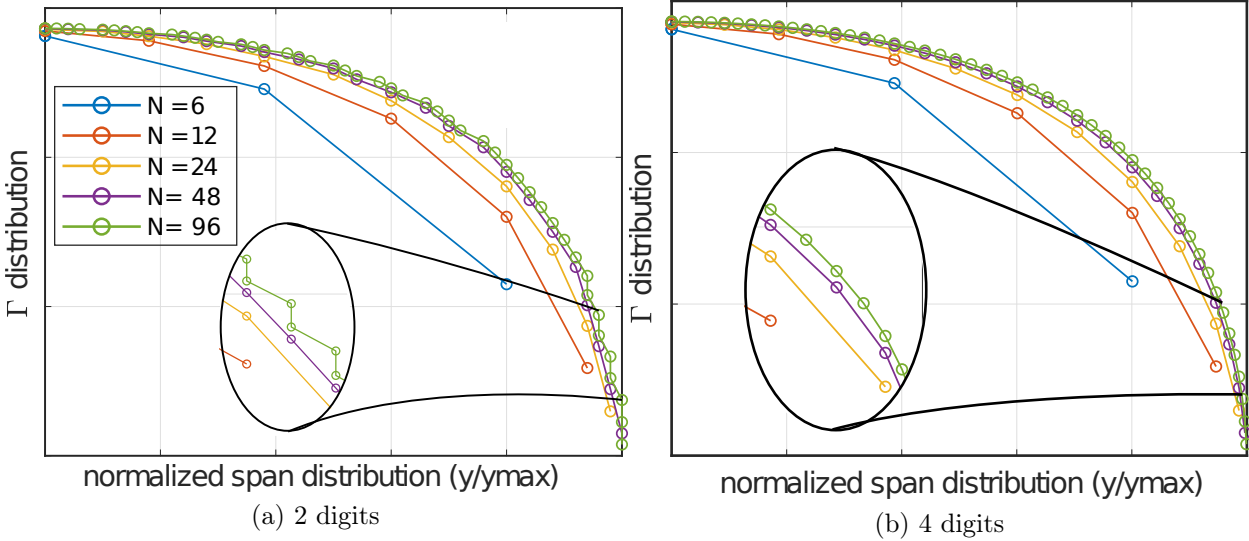


Figure 10: CASE # 1: Aliasing effects on the Γ distribution due to floating point number of digits in ASWING outputs file (default value: 2 for coordinates variables).

Table 3: Experimental evaluation cases 2/2. $\mathcal{U}\mathcal{A}$ = *S*nsteady *A*erodynamics ; (Git Repository: [ISAE ASWING Validation](#))

CASE	Geometry	Exp data	Evaluation type	Repeatability
$\mathcal{U}\mathcal{A}-1$	Plunging airfoil	[8]	<p>Comparison with Theodorsen on</p> <ul style="list-style-type: none"> - Time average of C_L - \tilde{C}_L first harmonic amplitude and phase φ_{C_L} - Phase average <p>Purpose : identify the limits of both theories imposed by the leading edge vortices developement</p>	Full
$\mathcal{U}\mathcal{A}-2$	Plunging wing	[7]	<p>Comparison with Theodorsen on</p> <ul style="list-style-type: none"> - Time average of C_L - \tilde{C}_L first harmonic amplitude and phase φ_{C_L} <p>Purpose : same as in the 2D case but also highlight the benefit of ASWING against Theodorsen in the 3D case</p>	Partial

at 10 spanwise locations. However, the pressure distribution was not integrated chordwise or spanwise, so the Webplot digitiser had to be used to obtain the local lift and drag coefficient distribution. The spanwise location of the pressure measurements is shown in figure 11. The ASWING airfoil parameters were calculated using XFOIL 6.99. As the boundary layer transition was forced, the XFOIL N_t parameter was adjusted to match the level of turbulence in the wind tunnel. When calculating the polar we ensured that the position of the transition was close to 5% of the chord as in the experiments. The airfoil parameters in the ASWING formalism were then: $cd_f = 0$, $cd_p = 0.01$, $cl_\alpha = 6.26 \sim 2\pi$, $\alpha_0 = 0$, $cl_{min} = -1.5$ and $cl_{max} = 1.5$. Note that cd_f is equal to 0. As the wing is straight and there is no side slip angle, pressure and skin friction drag will act in the same direction, we can consider $cd_f = 0$ without being conservative. Based on the mesh convergence analysis performed in the previous section, 40 nodes were used for the circulation distribution.

Figure 11 (a) and (b) show the total C_L and C_D predictions of ASWING 5-96 and the author's modified version, i.e. ASWING-m. A linear regression of C_L was performed on the linear domain. According to the slope errors, both versions show excellent agreement with the experimental data. Pre-stall is even captured. ASWING-m shows advantages in drag prediction, especially at high angles of attack. As predicted, the error in the drag prediction of ASWING is mainly determined by the constancy of the drag polar. When its variation with the angle of attack is taken into account, improvements are observed.

CASE SA-2 : 45° swept back wing

A second test case has been chosen to evaluate the lift and drag prediction of a highly swept wing. Note that a 45° sweep is very unlikely to be found in reality (for mini UAVs), so it is considered an extreme case. Experimental data come from J. Weber, Dr.rer.nat. and G. G. Brebner, M.A-1958. The tests were carried out in the No 2 11.5 by 8.5 ft Royal Aircraft Establishment wind tunnel. Three wing models were investigated, but only one case is presented here. The wing span is 98 inches (2.48 m). The chord is 20 inches (0.50 m) constant along the span up to 0.9b, then the wing tip has a curved leading edge and a straight trailing edge. Figure 12 shows the geometry. The airfoil was the RAE 101 (equivalent to NACA0012). Neither the turbulence level nor the location of the boundary layer transition were specified. Pressure measurements were taken on both the top and bottom sides of various spanwise locations (8 in total). The report provides spanwise and chordwise integration of the C_L and C_D values. Wall

corrections have been applied to the data so there is no raw data. The angle of incidence range is 0 to 10°. The wind speed was set to 163 ft/s (41.4528m/s) for an equivalent Reynolds number of 1.68E6. The case was numerically reproduced using the following parameters: $c_{l,\alpha} = 6.28$, $\alpha_0 = 0^\circ$ and $cd_p = 7.5 \cdot 10^{-4}$, $cd_f = 3.0 \cdot 10^{-3}$. As in the first case, 40 circulation nodes were used. Figure 12 (a) and (b) highlights the lift and drag predictions of ASWING and ASWING-m. Again, the proposed modification seems to have better performance, especially at high angles of attack for drag. According to the figure 12 (a) the second case shows for the first time the advantage of a viscous loop correction on the 2D c_l slope. The ASWING-m data agrees better with the experiment at high angles of attack. Despite these improvements, both versions show good agreement with the experimental data.

CASE SA-3 & 4: Quasi elliptical and crescent wing:

The aim of this validation process was to evaluate different chord and swept varying platforms. Consequently, experiments were chosen from the work of van Dam et al. (1991). Both wings were tested in NASA Langley's 7 x 10-foot high-speed wind tunnel. The first wing was a quasi-elliptical planform with an unswept quarter chord line as shown in figure 13. The second has a variable sweep angle as shown in figure 14. Both wings have an aspect ratio of 6 with a root chord and span of 8 inches (0.20 m) and 48 inches (1.22 m) respectively. The wings also have the same airfoil as the NASA NLF(1)-0416 with a maximum thickness of 16%. The models were mounted on a 6-component strain gauge balance supported by a straight string. The latter was chosen to match the maximum balance to the maximum expected load. The measurement accuracy was reported to be approximately 0.1% of full scale for normal force (lift) and 0.3% for axial force (drag). The accuracy of the angle of incidence was reported to be less than 0.01°. Finally, the uncertainty in the lift and drag coefficients was $9 \cdot 10^{-4}$ and $3 \cdot 10^{-4}$ respectively. The latter makes this experimental set highly reliable. The boundary layer transition was forced by the use of a 0.12-inch (0.3 cm) strip line placed on the top and bottom surfaces of the wing. A constant chordwise position was chosen to be 0.075c from the leading edge. Numerically, the geometries of the cases were reproduced using equations (2) and (3) of the van Dam et al. report (1991). As the boundary layer transition was reported at 0 angle of attack, XFOIL was used with N_t chosen to match the turbulence level of the configuration. The same number of circulation nodes was used as in the previous cases. Figures 13 (a) and 14 (a) show the lift predictions in the linear range of ASWING and ASWING-m. Again, the second seems to be more

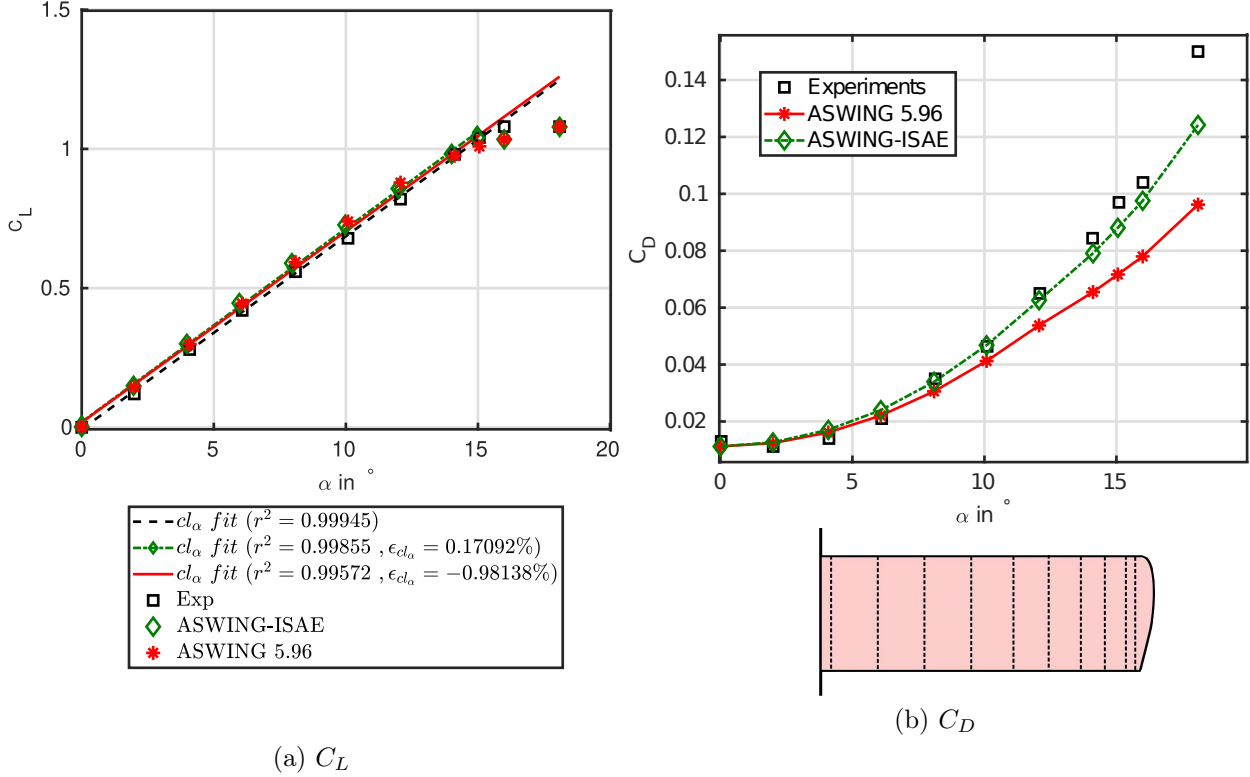


Figure 11: CASE SA-1 : Straight wing C_L and C_D predictions versus experimental from [1]. Improvement of C_L and C_D brought by a viscous loop and a quadratic varying 2D drag coefficient.

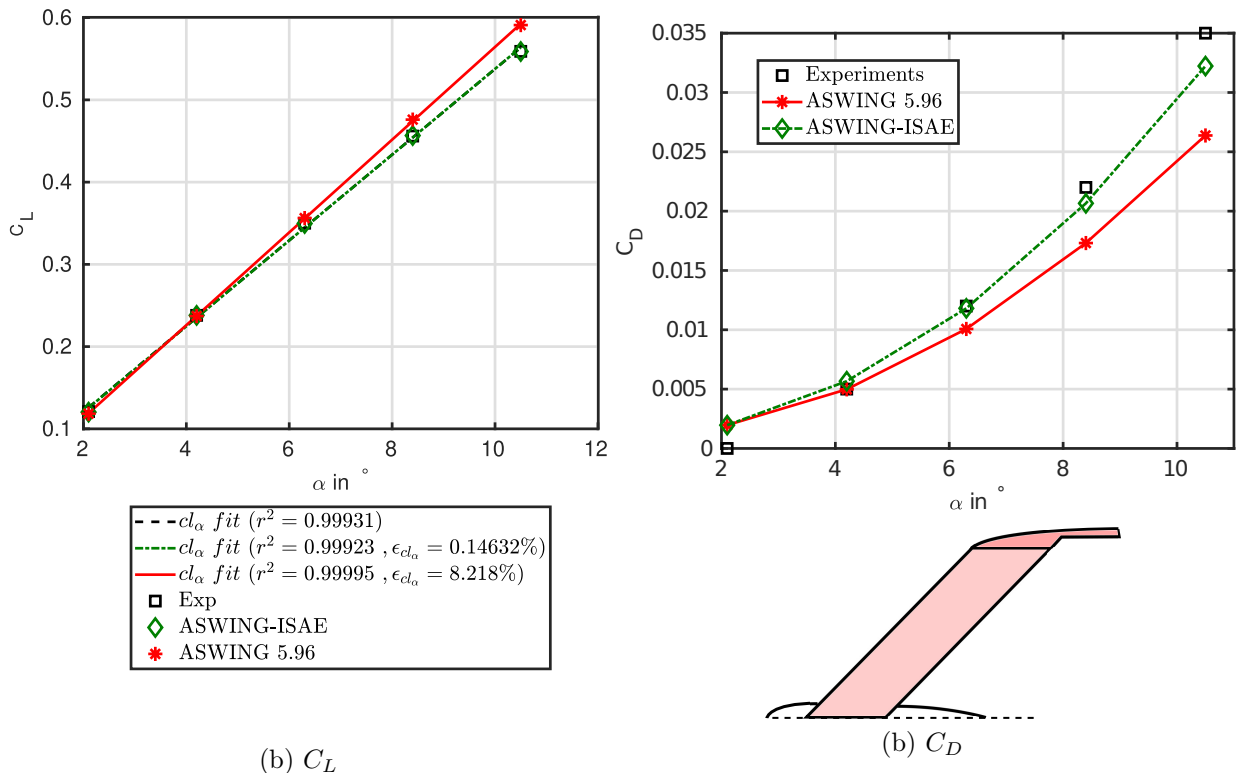


Figure 12: CASE SA-2 : 45° swept back wing C_L and C_D predictions versus experimental from J. Weber, Dr.rer.nat. and G. G. Brebner, M.A-1958. Improvement of C_L and C_D brought by a viscous loop and a quadratic varying 2D drag coefficient.

accurate, especially at high angles of attack. Both linear slope errors remain excellent. Figures 13 (b) and 14 (b) show the improvement obtained by taking into account the angle of attack dependence of the drag polar. The improved accuracy is not so obvious for the third case, but it is for the fourth. Note that if information about the transition of the boundary layer is provided when ASWING is mixed with XFOIL, it can predict the drag of a wing quite well.

CASE SA-5: Straight Wing with 45° Dihedral Angle

The last non-linear stress test for the lifting line is a straight wing with a dihedral angle of 45°. Again, as the second case, it is very unlikely to be seen, so it is considered a boundary case. This time no experimental data is available, so this is the first of a few high-fidelity CFD cases presented as stress tests. StarCCM+ was used to calculate the lift and drag coefficients of the wing. The aspect ratio of the wing was 5 with a NACA0012 airfoil. The Reynolds number was set to 100,000 (typical range for mini-UAVs). A structural grid mesh with a symmetry plan was used. The boundary layer was also discretised. For moderate angles of attack, a steady-state solver was sufficient to calculate the lift and drag coefficients. However, for angles of attack greater than 10° an unsteady solver had to be used due to the unsteady behaviour of the boundary layer. The C_L and C_D are computed along the z- and x-axis in STARCCM, while in ASWING they are computed along the planform normal and the chordwise vector. In order to respect the StarCCM+ formalism, the lift distribution has been integrated into ASWING and the lift coefficient has been calculated along the z-axis. The figures 15 (a) and (b) show the lift and drag predictions. Note that in figure 15 (a) we use the term "uncorrected LLT" to denote the previous comments on how the lift coefficient is calculated in ASWING. For the sake of clarity, only the lift prediction of the ASWING-m version is plotted. Again, excellent agreement is observed for the linear slope. With regard to drag, the better performance of ASWING-m in predicting drag is highlighted.

CASE SA-6: Effect of ailerons on rolling and yawing moment coefficients

As seen in the theoretical section, ASWING can take into account the effect of different ailerons or flaps on the lift and drag distribution. A lift asymmetry induced by deflected ailerons has 2 main effects, inducing rolling and yawing moments. To evaluate this feature, the experimental data of [Heald and Strother 1929](#) and [1930](#) have been used. In their work, they evaluated the rolling and yawing moments induced

by the anti-symmetric deflection of different ailerons. The wing was straight with an aspect ratio of 6, again a very good stress test for the lifting line model. The airfoil was the ClarkY. The test was carried out in the 10ft Bureau of Standards wind tunnel. Rolling moments were measured using a balance connected to the wing tip by a stiff wire at the quarter chord line. The yawing moments were measured using the same type of balance but connected to the tail of the fuselage. The moment coefficients were then calculated at the wing root on the quarter chord line. The accuracy of the measurements is given in the author's work and is excellent (about 1%). Various ailerons with different span and chord lengths were tested. Figure 16 (a) shows the different configurations (lower span variation, upper chord variation). The flap deflection range was 0 to 40° with an interval of 4°. The author also specified that the slots created by the deflected ailerons were filled with wax to ensure a certain smoothness of the geometry. In total, 3 wing incidences were tested, but we will present only 2 for the sake of this document readability.

Numerically, the ClarkY airfoil polars and flap derivatives were calculated in XFOIL and summarised in the table 4. Note that convergence failure was observed at high flap deflections in XFOIL, the range had to be reduced to calculate the flap derivatives. As ASWING can natively provide the roll and yaw moment coefficients, the bench was easily reproduced without the airframe. Again, 40 circulation point circulation variables were sufficient to obtain satisfactory results.

Figure 16(a)-(d) shows the ASWING predictions of the rolling and yawing moment coefficients for different aileron configurations and the level flight condition ($\alpha = 4^\circ$). [Heald and Strother](#) reported that there were 2 linear behaviours, from $\delta_F = 0^\circ$ to $\delta_F = 20^\circ$ and above. In the first, we compared the linear slopes. ASWING shows excellent agreement with experiments for the rolling moment coefficient as shown in figure 16(a) and (b), regardless of the aileron configuration. The average slope error is 4.4 %. The same conclusions cannot be drawn for the yawing moment coefficient predictions (figures 16(c) and (d)) where the slope error is above 50%. The yaw moment induced by a deflected aileron is mostly drag-related. Or ASWING assumes a symmetrical shift of the viscous/pressure drag polars when a flap is deflected negatively or positively. In reality, this is not the case. This can be easily seen in XFOIL. The asymmetry of the viscous/pressure drag is not taken into account, whereas the lift-induced one is. As a result, ASWING misses a large contribution to the yawing moment. The same tests were carried out but in the post-stall condition ($\alpha = 16^\circ$). These are interesting to show the limits

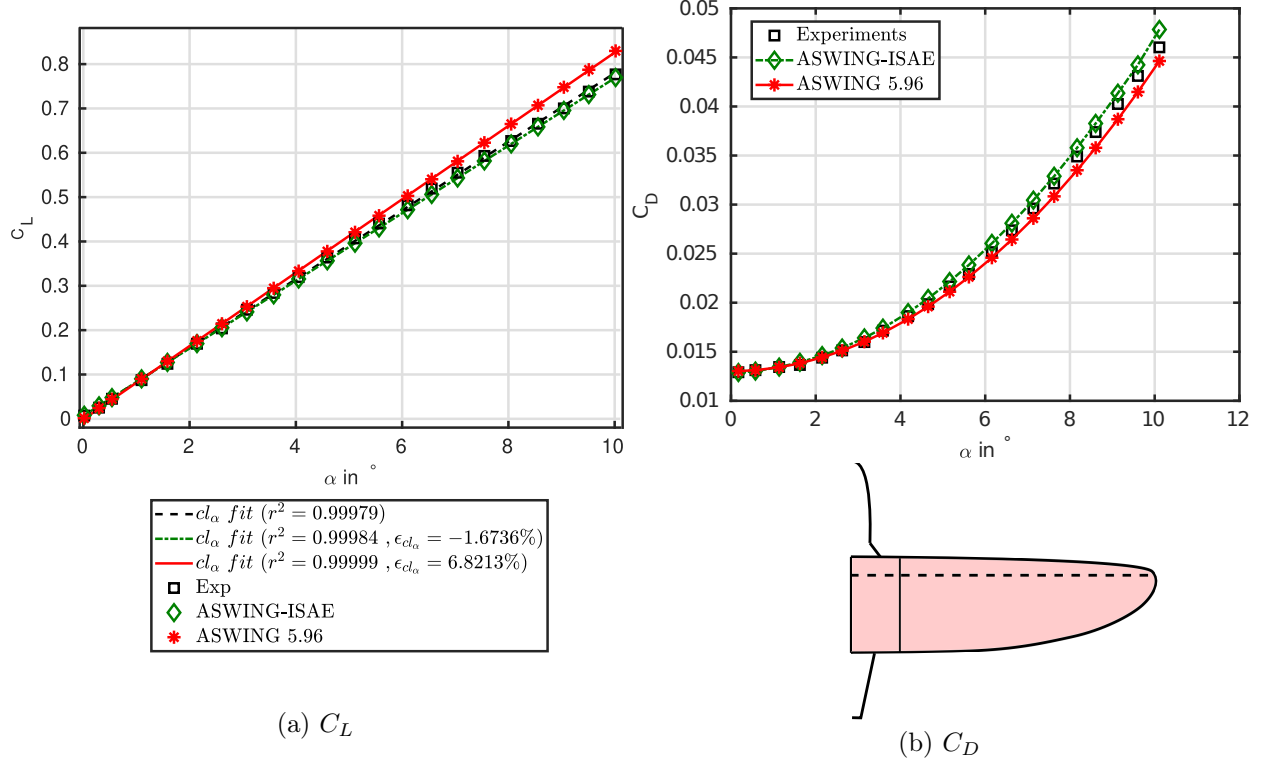


Figure 13: CASE SA-3 : Quasi-Elliptical wing C_L and C_D predictions versus experimental from van Dam et al. 1991). Improvement of C_L and C_D brought by a viscous loop and a quadratic varying 2D drag coefficient.

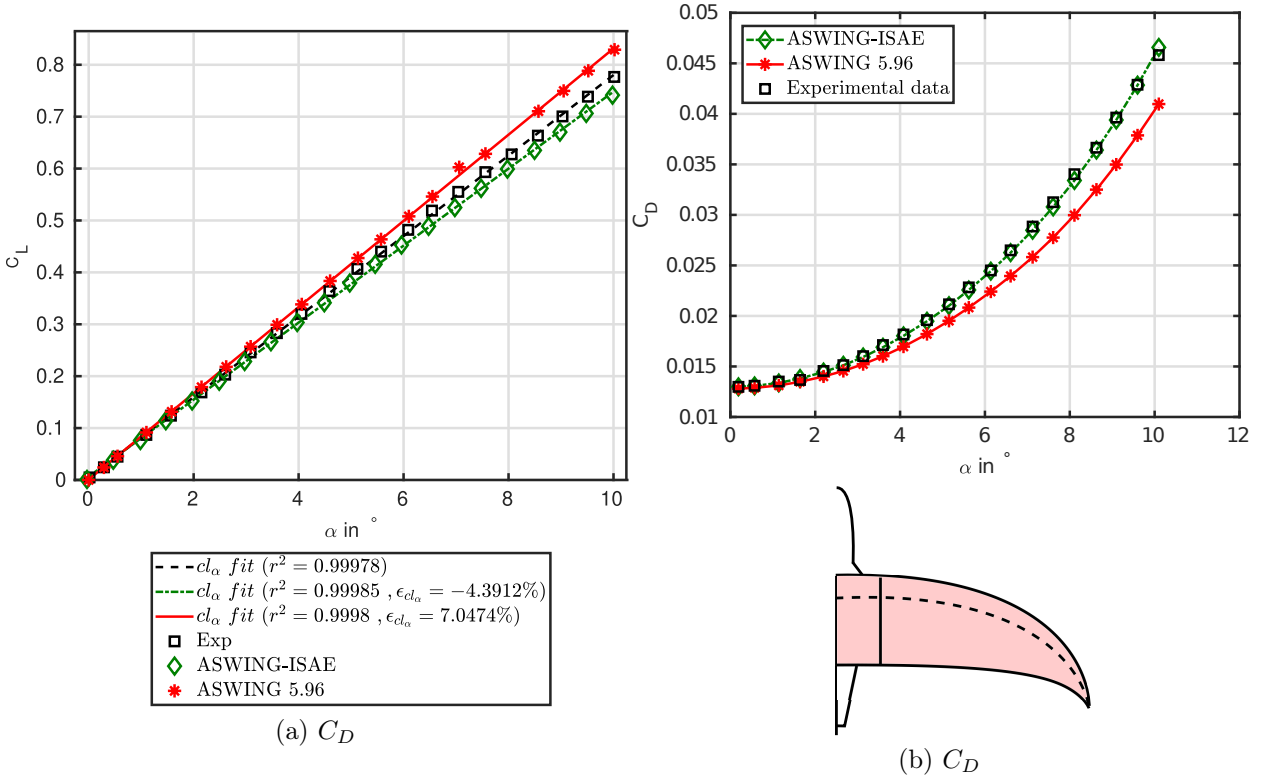
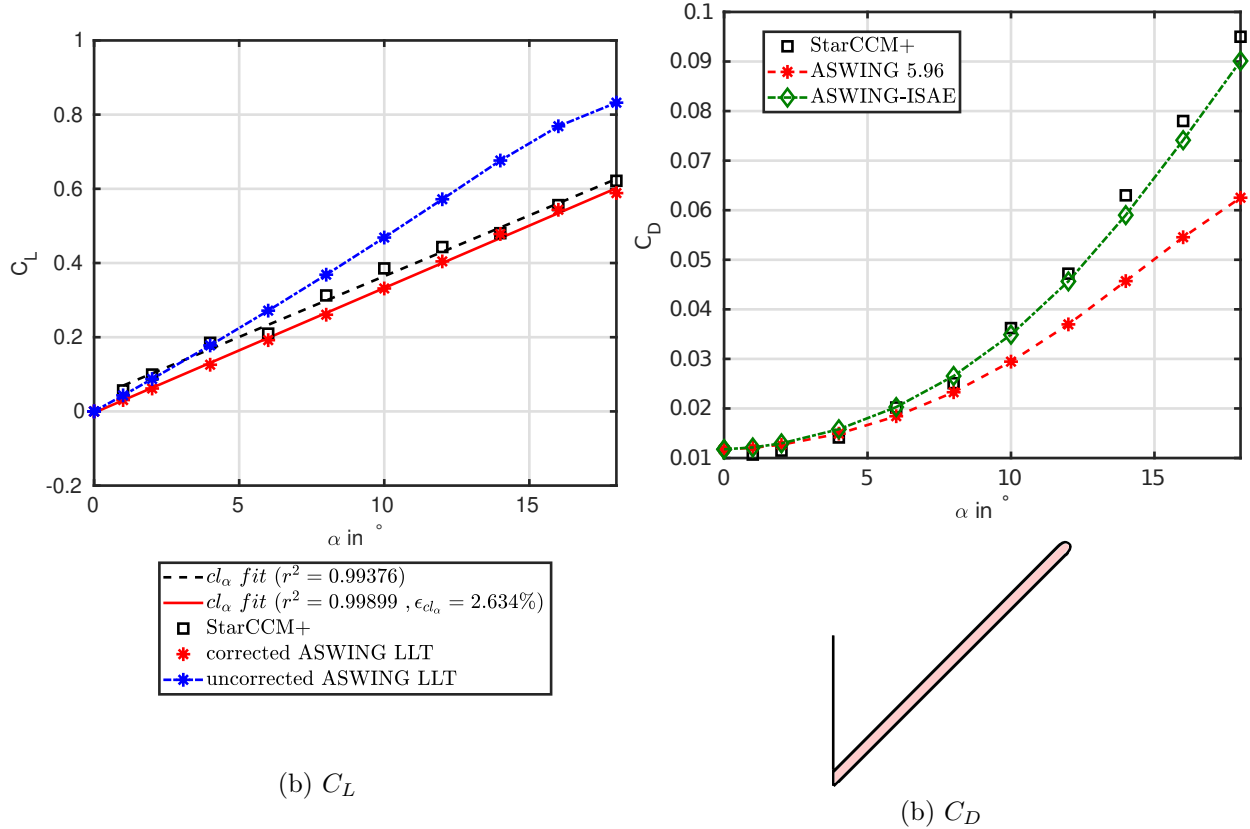


Figure 14: CASE SA-4 : Crescent wing C_L and C_D predictions versus experimental from van Dam et al. 1991). Improvement of C_L and C_D brought by a viscous loop and a quadratic varying 2D drag coefficient.

Figure 15: CASE SA-5 : Straight Wing with 45° dihedral angle C_L and C_D predictions

of the ASWING. Based on figures 17 (a) to (b), the framework is no longer able to predict the rolling moment coefficients even for moderate flap deflections. The average pitch error increases to 20%, which is unacceptable. For the yaw moment (figures 17 c and d) the same remarks are made as for the level flight case.

Finally, the last remarks are made for high-deflected ailerons (above 20°). Emphasis is placed on the level flight configuration and the predictions of the rolling moment coefficients. ASWING seems to capture the slope damping due to the local stall, but not enough. A first suggestion would be that the geometry becomes extremely sharp at high flap deflection, regardless of the hinge position. At a lower angle of attack, the airflow would be more likely to detach, which is not captured by ASWING. In conclusion, ASWING correctly predicts the rolling moment coefficient induced by the ailerons for moderate deflections and when the wing is in its linear lift range. It can also predict an induced yawing moment, but not accurately.

CASE SA-7 and 8: Multiple lifting surfaces, tandem aircraft

As seen in the theoretical sections, ASWING can take into account the wake interactions between multiple lifting surfaces. In this section, 2 different sets

of data from the literature have been used. The C_L predictions of each lifting surface in the linear and pre-stall range have been evaluated. Total C_L vs C_D predictions were also evaluated. CASE 7 is based on experimental data from the work of (Feistel et al., 1981) and compared to high fidelity and potential methods of (Cheng and Wang, 2018). CASE 8 is a high-fidelity CFD (RANS) case presented in the latter author's paper.

In case 7, the experiments were performed in the 7 x 10 ft wind tunnel at the Ames Research Center. The tandem configuration consists of 2 rectangular blades: one forward and one aft. Both were constructed based on the GA(W)-2 airfoil section and had the same aspect ratio, which is 6. The forward wing span and chord were $b_f = 1.29m$ (4.24ft) and $c_f = 0.22$ (0.71ft) respectively, while the rear wing span and chord were $b_b = 1.83m$ (6.0ft) and $c_b = 0.305m$ (1.0ft). In their work, the authors studied the influence of geometric parameters on the overall tandem performance. Among them, the vertical and horizontal gaps could be modified. In this paper, only the worst-case scenario is presented, where the wake interaction was the strongest. So the vertical gap was chosen to be positive from the front to the rear wing with a value of $G = 0.5c_f$. Similarly, the horizontal gap was chosen to be $1.63c$. The reader can get an overview of the geometry in figure 18. The tests were carried out at a Reynolds number of 1.6E6 and the angle of attack

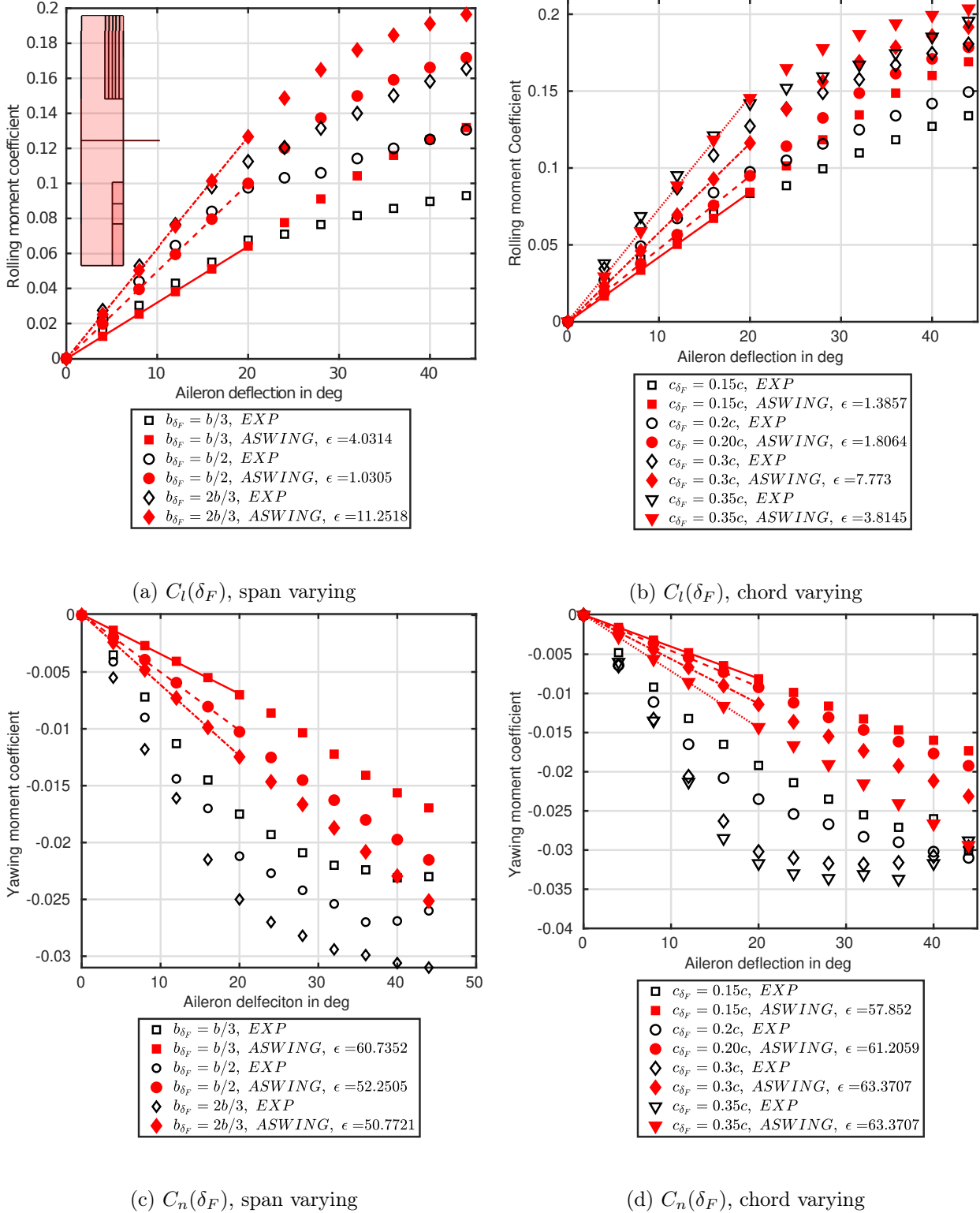


Figure 16: CASE SA-6: Effect of various deflected ailerons on the rolling and yawing moment coefficients. ASWING prediction against experimental data (Heald and Strother, 1929). Level flight condition (un-stalled $\alpha = 4^\circ$)

Table 4: ClarkY wing parameters ($Re = 3E5$)

Ailerons chord	0.15c	0.20c	0.25c	0.30c	0.35c
$dc_l/d\delta F$	-0.039	-0.045	-0.055	-0.061	-0.71
cl_α		5.77			
α_0			-3.77°		
ϑ				4°	

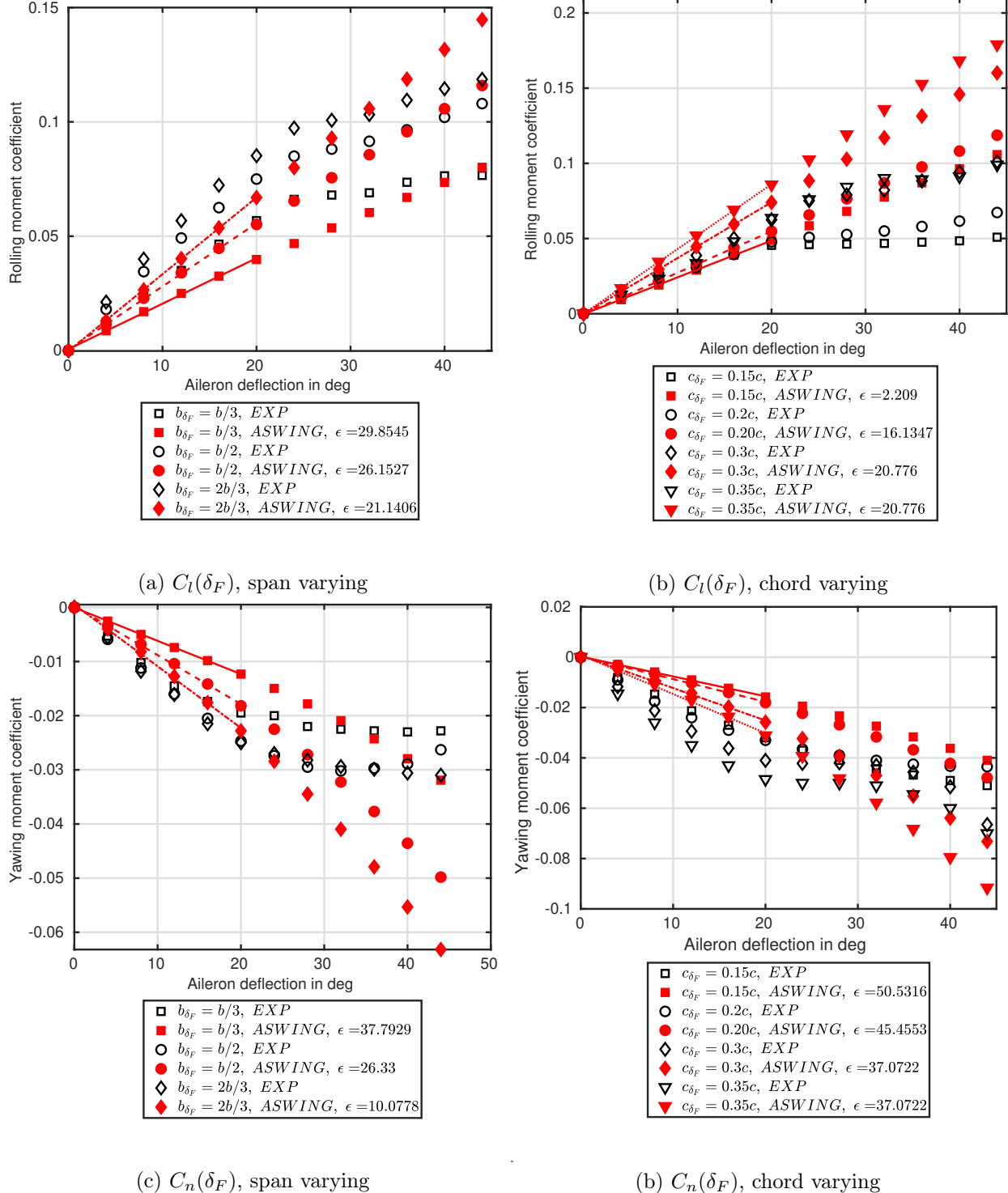


Figure 17: CASE SA-6: Effect of various deflected ailerons on the rolling and yawing moment coefficients. ASWING prediction against experimental data from Heald and Strother 1930. Level flight condition (post-stall $\alpha = 16^\circ$)

varied from -2 to 20°. Two balances were placed on each wing to measure each wing C_L and C_D .

In the 8th case, the geometry was slightly different as the wing spans were almost the same. The forward wing span is 2.1805 m, while the rear wing span is 2.0424 m. They have the same chord and airfoil, which is 0.129m and NACA4309. The horizontal and vertical distances are set to 0.89m and -0.101m. Note that a square section airframe is modelled with a length of 1.25m and a section size of 0.129 by 0.129m. The geometry is shown in figure 28. The flight speed is set to 30m/s for an equivalent Reynolds number of 265000. RANS calculations were performed in the linear and pre-stall domains. The latter was performed using a structured grid solving the 3D Navier-Stokes equations using the finite volume method and the SST $k - \omega$ turbulence model. The author provided the C_L of each lifting surface and the total lift. Note that the drag was not presented. The author also presented the previous set with and without the influence of the airframe.

Numerically, the same comments are made for both cases. The airframe influence was neglected on ASWING because it cannot model non-circular airframes. Furthermore, the exact dimensions of the latter have not been given. For each platform, 40 circulation nodes were selected using a cosine clustering function. Note that Cheng and Wang (2018) uses a slightly different clustering function for case 7. As the wingspans are not equal, i.e. the front wing is shorter, they suggested using a dual cosine clustering function on the rear wing. This, in fact, recovers more accurately the effect of the forward wing wake, as the circulation mesh on the rear wing is more refined where the wake gradient is important. In ASWING it is not possible to implement such clustering functions. However, it will be seen that this is not necessarily a problem.

In both cases, the predictions of ASWING-m are not presented. Instead, a comparison of ASWING predictions with other authors' potential methods and high-fidelity methods is proposed. In the linear domain, the slopes of the lift coefficients were calculated using linear regression. The results for case 7 are shown in figure 18(a)-(d). As with the single planform, the ASWING C_L predictions (Figures 18a-c) are in excellent agreement with the experiments. Note that the ASWING slopes errors are less than 8%. They are also equivalent to the results obtained by Cheng and Wang (2018). It is interesting to note that for C_L predictions, the high-fidelity CFD results are almost comparable to those of the LLT. Regarding the drag predictions (Figure 18-d), the ASWING predictions are in good agreement at a high angle of attack and

become weaker around zero lift.

Regarding the 8th case, again the C_L predictions (cf. Figures 28 a to c) are in excellent agreement with the CFD data. Note that Cheng and Wang's LLT error seems to be more important than ASWING. This could be due to the airfoil polar calculations. ASWING and Cheng and Wang's work is based on the same physics and assumptions. It is therefore very unlikely that ASWING is better than the author's work. Note that ASWING captures the pre-stall effect on both tandem wings, while [6]'s LLT doesn't.

In summary, we can conclude that ASWING can correctly predict the lift and drag of tandem configurations. Despite ASWING's horseshoe representation, which is straight and shed from the horseshoe boundary and not from the trailing edge of the airfoil, it has no or little effect on the wake interaction. Finally, the dual cosine clustering for the circulation mesh does not seem to have a major impact on the quality of the predictions. The last two examples conclude the section dedicated to the steady lift and drag predictions of the ASWING lifting line model and its proposed improvements.

CASE SA-9 A-E : Lift distribution and centre of pressure location

So far, the main problem that could be attributed to the previous cases is that they do not present local lift predictions, which is actually mandatory for a flexible aircraft framework. In fact, they have all presented total lift coefficient predictions. Despite for different lift distributions, the total lift coefficient can be the same. Therefore in this section 5 swept forward and backward wing lift distributions and loading predictions are compared with experimental data.

Experimental bench: The work of McCormack and Stevens Jr (1947) and VanDorn and DeYoung (1947) has been used. Five swept forward and backward wings were tested. The root and tip airfoils were NACA0015 and NACA23009 respectively. The wing dihedral angle was kept at 0 degrees. The twist in the chord plane of the wing was approximately 0.25 degrees. The main geometric parameters are summarised in the table 5. Note that the sweep angle is defined from the quarter chord line, with a negative angle defining a forward sweep angle. The wing was mounted on a faired string attached to a 3-strut support system. The tests were carried out in the AMES 40 x 80 ft wind tunnel at a Reynolds number of 9E6. Pressure sensors were placed at various spanwise and chordwise locations. The results were integrated and presented as local lift coefficients.

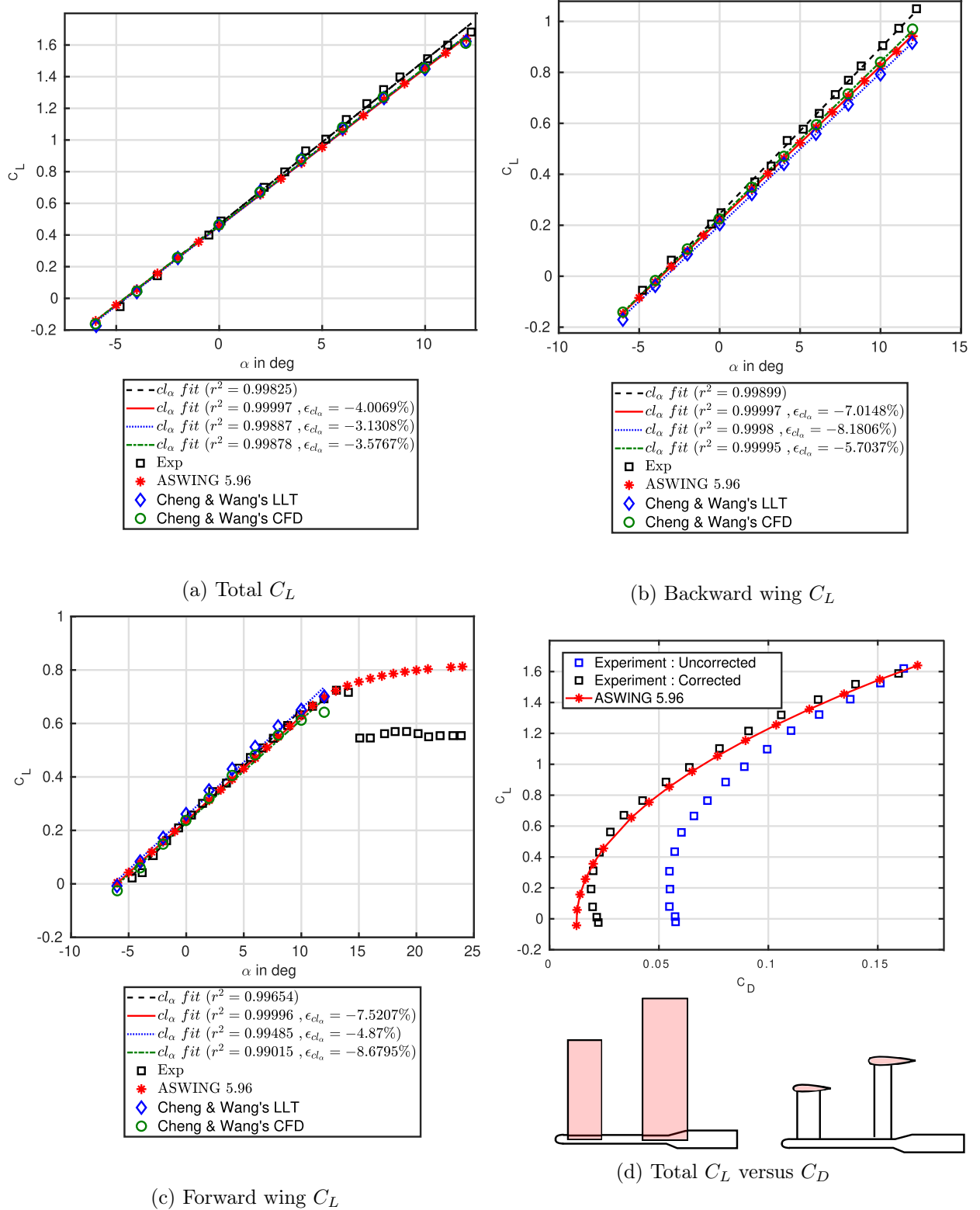


Figure 18: CASE SA-7 : Tandem #1, total, backward and forward wing C_L and C_D predictions versus experimental and CFD data from Feistel et al. (1981) and Cheng and Wang (2018))

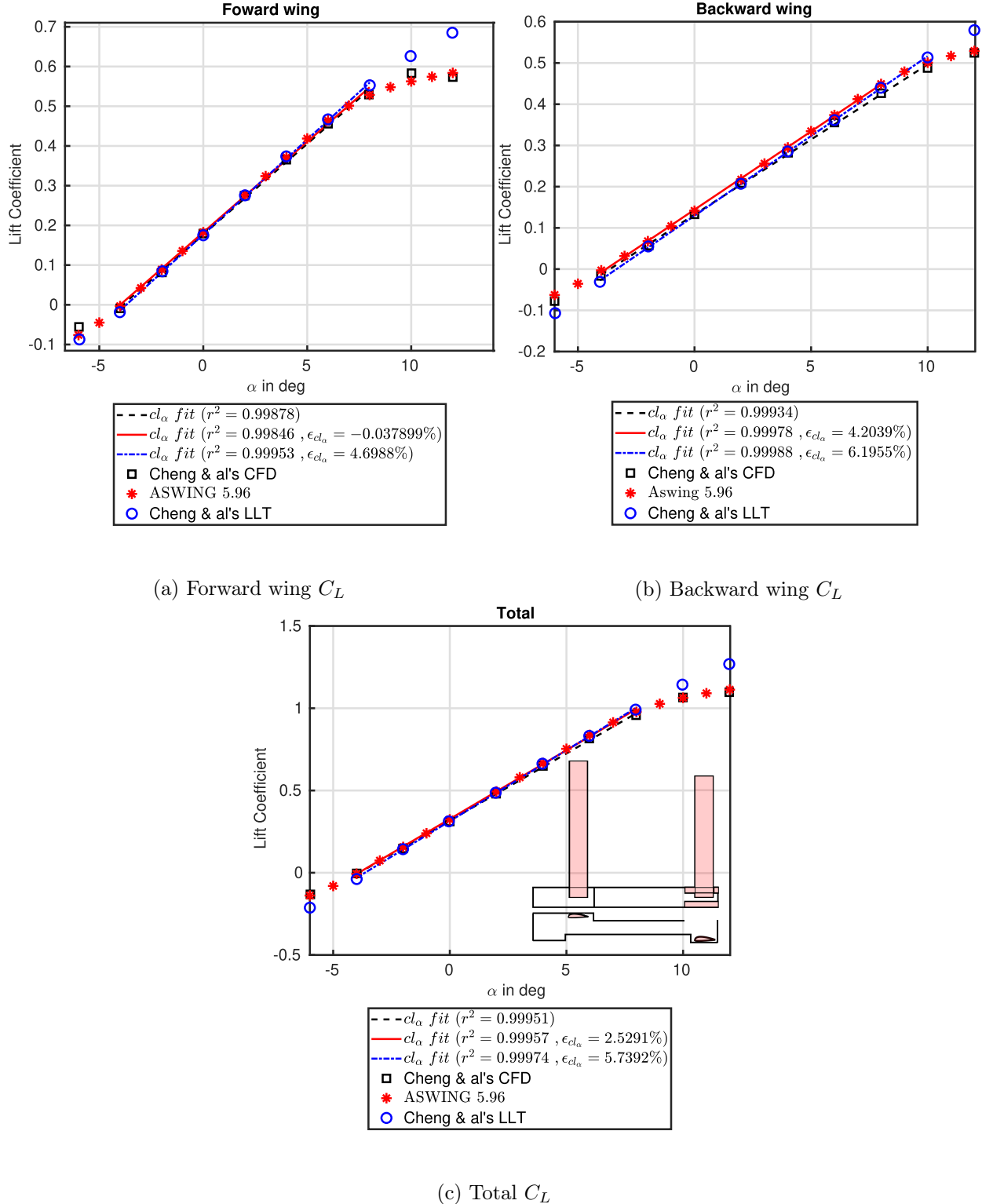


Figure 19: CASE SA-8 : Tandem #2, total and backward wing C_L predictions vs higher fidelity data from Cheng and Wang (2018)

Numerical bench: The benches were easily reproduced in ASWING. Due to the high Reynolds number, XFOIL analysis of NACA0015 and 23009 was not performed. The airfoil lift slope and zero lift angle of attack were set to 2π and 0° . During the simulations, a drop in the lift coefficient distribution at the wing root was observed. For some reason, this drop increases with the sweep angle regardless of its sign. No explanation has yet been found. In order to get rid of this problem, the circulation mesh was voluntarily refined. Thus, 200 instead of 40 circulation piece-wise variables were used for the simulations.

Results: The ASWING predictions are compared with the experimental data of [McCormack and Stevens Jr \(1947\)](#) in figure 20. Irrespective of the sweep angle, ASWING is able to correctly predict the lift distribution of low aspect ratio swept wings. It can also provide qualitative predictions of the spanwise location of the wing centre of pressure. For example, it can be seen that the centre of pressure tends to move towards the wing root at negative sweep angles and towards the wing tip at positive sweep angles. From a structural point of view, this would result in a lower root bending moment. Note that [VanDorn and DeYoung \(1947\)](#) have proposed a comparison between a lifting line model and a vortex grid model. Both have similar performance in predicting lift distributions. Therefore, it is clearly reasonable to use the lifting line theory for wings with these aspect ratio.

CASE SA-10 Wingtip and Tip Sails:

An interesting feature of ASWING is that it can model multiple lifting surfaces. Thus, experimental data from [Miklosovic \(2008\)](#) has been used to assess the predictions of the effects of wingtip devices. In their work they have tested various wingtip devices, from tip extensions to tip sails with different cant angles. The devices tested in this thesis are shown in figure 21 (a). These were chosen as they are the only ones for which lift and drag measurements have been provided. [Miklosovic](#) also provided the airfoil polars as they also compared their results with the Vortex Lattice predictions. Therefore, for the sake of readability, the numerical bench is not described here. Figure 21 (b) shows the lift predictions of ASWING 5-96 against the experimental data. Linear slopes have been calculated on the apparent linear region. As can be seen, ASWING does a is capturing well the increase in the linear lift slope due to a blended wingtip. Note that the lift measurements of the wingtip configuration have not been provided. For the other cases, which are planar wings, the prediction errors are quite consistent with the previous cases presented earlier in the report. Figure 21 (c) shows a comparison of the ASWING drag predictions with experimental mea-

surements. For the planar wings, the drag predictions are in good agreement with the experiments. It captures well the increase in zero lift drag coefficient for the extended tip configuration due to the increased wetted area. However, ASWING is not able to provide good predictions for the tip sails. In fact, during the simulations, some local lift divergences were observed at the connection between the tip sails and the wing. ASWING is not able to trigger the circulation continuity at the wing tip because of the 3 wing tips, so it does not manage the close interactions in this specific case. Thus, in this example, ASWING can capture the effect of the continuous wingtip, but not of the tip sails.

CASE SA-11: Discussion of transonic flight: KC-130 with Whitcomb winglets

The analysis of the single planform concludes with a discussion of transonic flight. ASWING is clearly not designed for this flow regime. However, it can provide interesting results on the effect of wingtip devices on the lift and drag predictions of a first-generation jet aircraft. To illustrate this, experimental data from [Jacobs et al. \(1977\)](#) has been used. They have tested different wingtip devices on a small-scale Boeing KC-135. In total we present 4 different configurations, the wing alone, the wing with a tip planar extension, the wing with an upper winglet and the wing with the Whitcomb winglet. The details of the geometry can be found in Appendix D of this report. We will not go into too much detail about the parameters used here, as we only want to show the tendency. Of course, reasonable values have been chosen as MSES was used to compute the airfoils polars. The figures 22 (a) and (b) show the lift predictions against the experimental data. The linear slopes have been calculated again. While the agreement is quite good at Mach number 0.7 (figure 22-a), the ASWING loses its way at higher Mach numbers. Although the Prandtl-Glauert correction factor is activated, the ASWING does not capture the Mach number effect on the lift slope well. Figures 22 (c) and (d) show the drag versus lift coefficient predictions and as expected, ASWING does not correctly capture the drag, especially at high lift coefficients. At higher Mach numbers the discrepancies are even worse. However, it does correctly capture the tendencies introduced by the use of winglets, which is a reduction in drag. Very small reductions, such as the one reported, have been observed in cruise conditions. A good improvement to ASWING would therefore be to make the airfoil parameters a function of Mach number and angle of attack. In fact, in transonic flight, the wave shock seems to have a large influence on the airfoil drag. The wave shock itself creates drag (momentum defect) and also has an effect on the boundary layer thickness

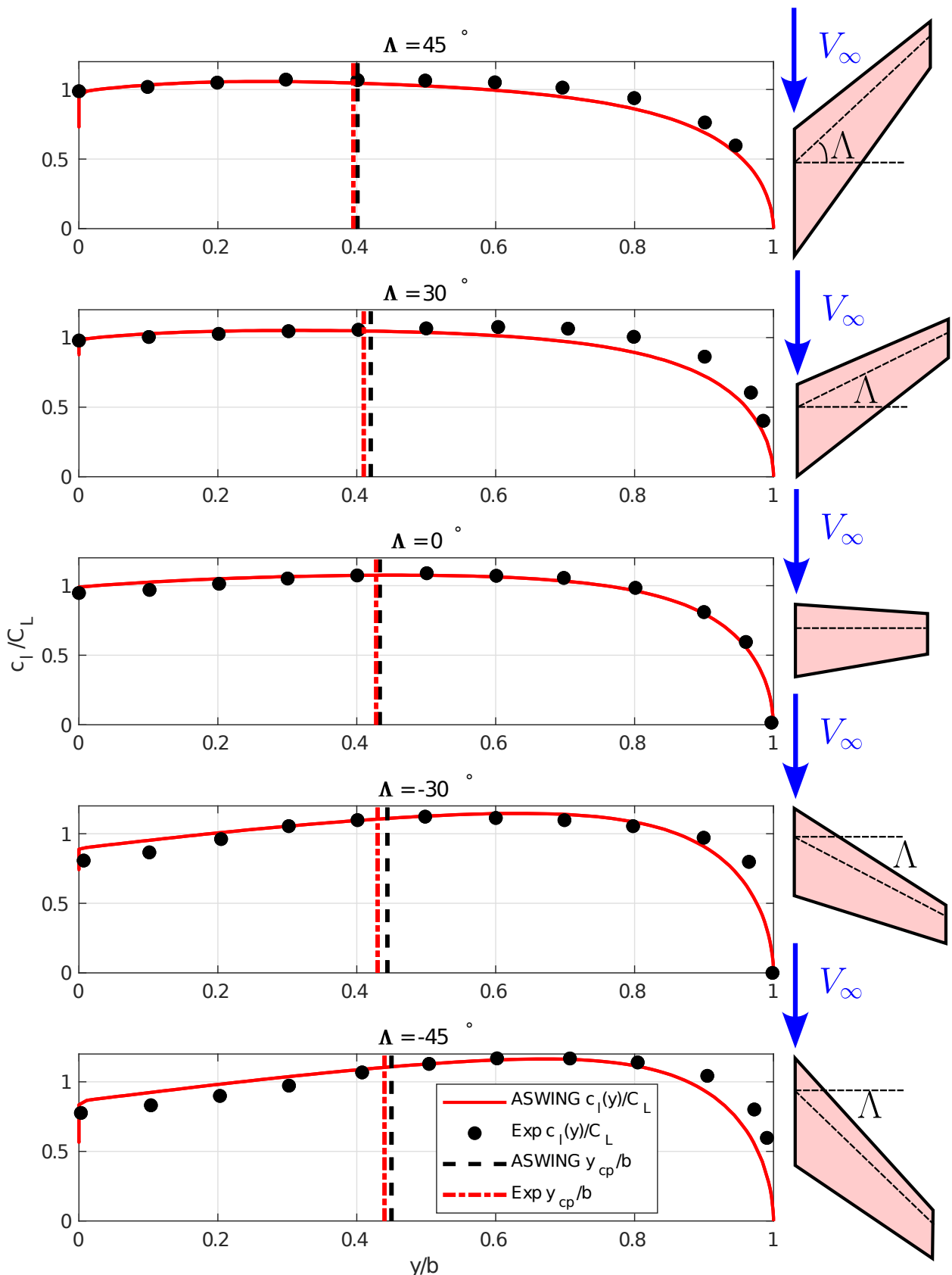


Figure 20: CASE UA-9 A-E: lift coefficient and centre of pressure location predictions for 5 swept forward and backward wing. Comparison with experiments from McCormack and Stevens Jr (1947)

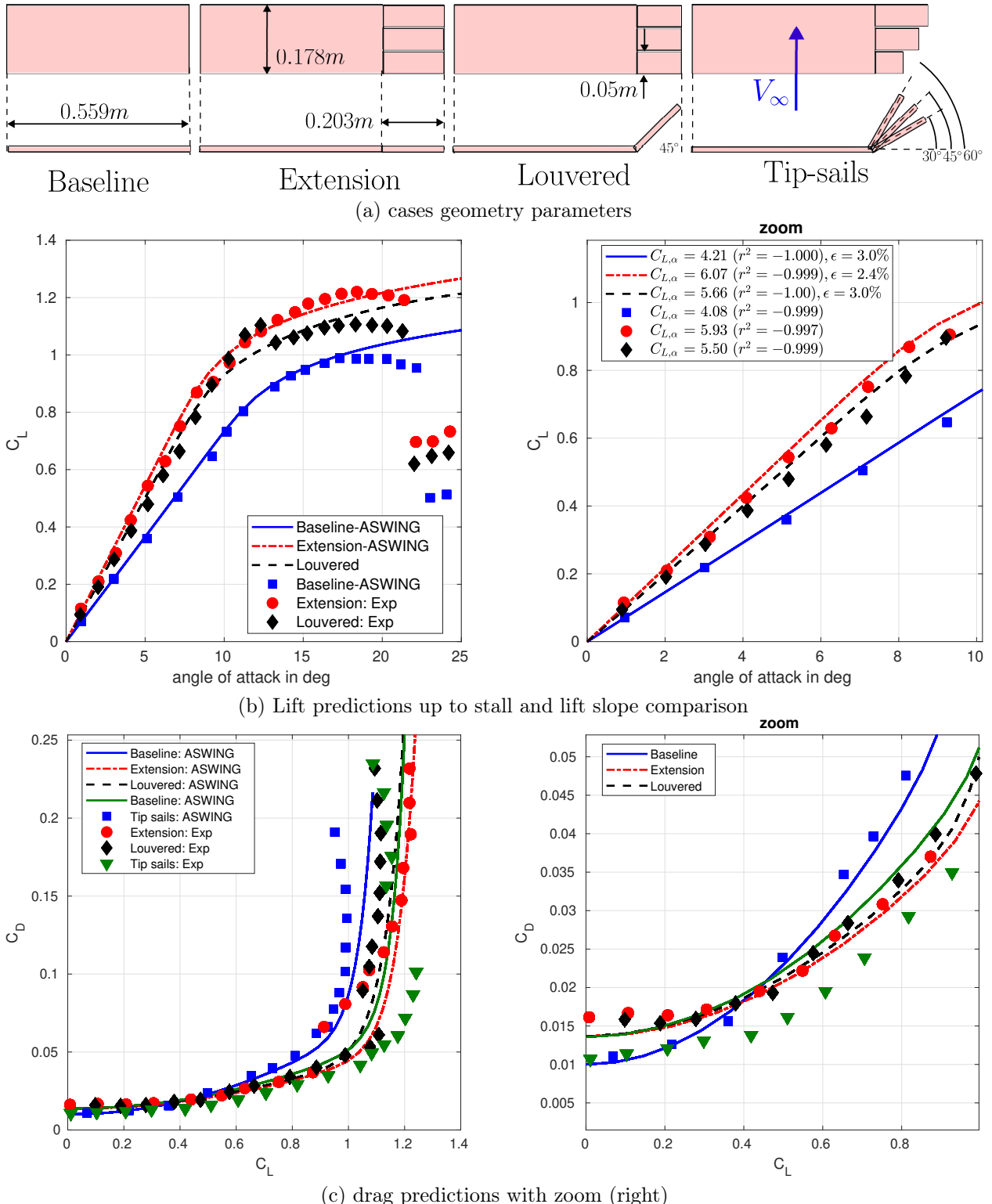


Figure 21: CASE SA-10: Lift and drag predictions of configurations with bent winglet and tip sails. Comparison with experimental data from (Miklosovic, 2008)

CASE	Λ (in°)	b (in m)	AR	c_R (in m)	c_T (in m)
9-A	-45	9.87	3.12	4.69	1.76
9-B	-30	11.09 m	4.69	3.46	1.40
9-C	0	9.31 m	4.66	2.65	1.44
9-D	30	10.99 m	4.84	3.23	1.42
9-E	45	10.23 m	3.84	4.07	1.70

Table 5: Swept forward and backward wings parameters ($\Lambda < 0$: swept forward)

and separation as shown in Appendix D, which drastically increases the profile drag (pressure and friction). Consequently, MSES could be used to generate transonic airfoil polars at different Mach numbers, which would be implemented as a bi-polynomial function in ASWING. Improvements in lift and drag predictions should be observed. Note that the Plandtl-Glauert correction factor should be disabled as the compressibility effects will be embedded in the polynomial functions.

Case SA-12 A-B: Ground effect on a rectangular wing with various flaps:

As presented in the theoretical section, ASWING can model two types of ground surfaces, solid and free. In this subsection, the experimental data of [Recant \(1939\)](#) have been used to evaluate the ASWING ground predictions on the lift and drag. This will highlight when the ground effects are strong. In their work, they tested several wings, a rectangular one and a tapered one with different flap configurations (plain and slotted). Similar comments have been made about the wing planform, so only the rectangular one is presented here. However, two configurations are shown, the wing without flaps and with slotted flaps. This choice has been made mainly to highlight the weakness of ASWING in predicting the ground effect on wings with slotted flaps.

Experimental bench:

The tests were carried out in the NACA 7 x 10 foot wind tunnel. The wing model was a rectangular wing with an aspect ratio of 6, a span of 60 inches (1.524 m) and a chord of 10 inches (0.254 m). The airfoil was a NACA23012 as shown in figure 23 (a). For the slotted flap version, the hinge axis was placed at 0.82 of the wing chord from the leading edge with a fixed flap down angle of 40 degrees. The wing was anchored to a balance at on the quarter chord line at the root. The altitude was then changed according to this position. For both configurations (no flap and slotted flap), drag and lift measurements were made at an effective Reynolds number of 900,000 over a range of angles of attack from -6 to 16 degrees. Several altitudes were tested, but due to the age and lack of clarity of the plots, only three are presented here. The height is given as the ratio of the chord h/c , where h is the

height of the wing.

Numerical Bench:

Unfortunately, [Recant's](#) paper does not give any information about the location of the wing transition or the level of turbulence in the wind tunnel. However, these experiments were part of a larger project where 2D experimental lift and drag measurements were made. Therefore, in this case, XFOIL was not used to obtain the aerodynamic profile parameters of ASWING. Instead, the experimental measurements provided by [Wenzinger and Harris \(1939\)](#) have been used to obtain the lift slope, zero lift drag and angle of attack of both configurations. A linear interpolation was used to obtain the 2D lift slope. For the wing without flaps the airfoil parameters are $c_{l,\alpha} = 6.0$, $c_{d,0} = 0.01$ and $\alpha_0 = -1.0^\circ$ while for the slotted version they are $c_{l,\alpha} = 7.44$, $c_{d,0} = 0.04$ and $\alpha_0 = -12.5^\circ$. Note that the lift plot for plain wing has been plotted with a shift of zero lift angle of attack at the origin, so the ASWING prediction results have also been shifted accordingly. As the slotted flap deflection was the same along the test, in ASWING the airfoil parameters were simply modified instead of implementing the flap derivative.

Results:

Figures 23 (a) to (d) show a comparison between the ASWING lift and drag predictions and the experiments for both configurations. For the wing without flaps, ASWING provides excellent agreement with the experiments for the lift slope increase due to the close proximity to the ground. The error of the lift slope prediction is less than 5 %. For the drag predictions, the results are in reasonable agreement with the experiments, the reduction of the lift-induced drag is well captured for positive lift coefficients. For high lift coefficients, the predictions start to show discrepancies. Note that when the wing was quite close to the ground the ASWING post-stall drag model was divergent, once deactivated the prediction results became better. This should be taken into account when investigating ground effects.

For the wing with slotted flaps, the ASWING predictions are not satisfactory for both drag and lift. It seems that the ground effect on the slotted flap physics is dominant compared to the ground effect on the wake vorticity. The former is not captured by

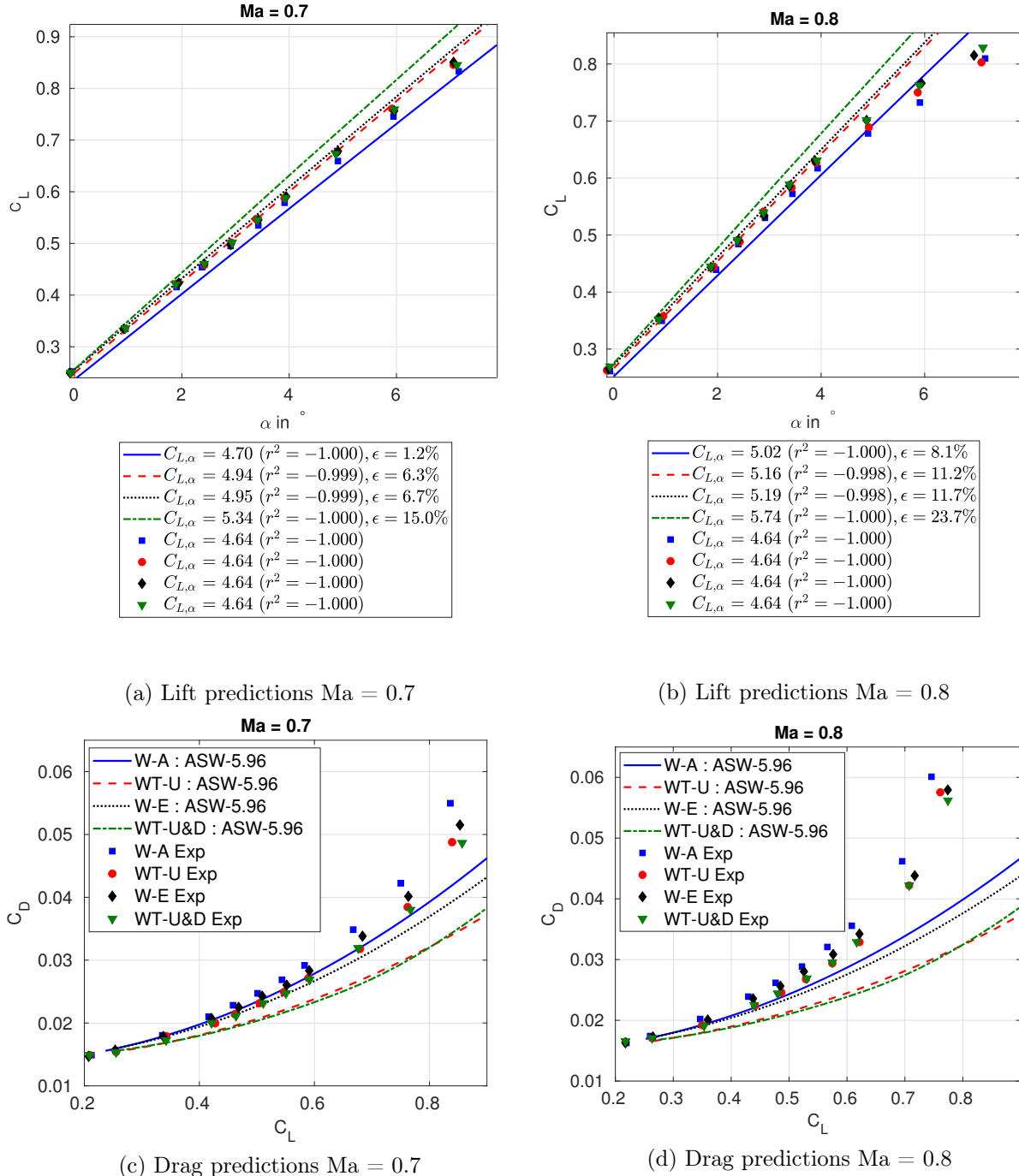


Figure 22: CASE SA-11. Lift and drag predictions of the KC-135 wing with various wingtip devices. W-A : Wing Alone, WT-U : Wingtip up only: W-E : Wing Extension, WT-U&D Wingtip Up and Down. Experimental data from Jacobs et al. (1977) part of the program Barber and Selegan (1982)

the ASWING theoretical model, hence the observed discrepancies.

In conclusion, ASWING can predict well the effect of ground proximity on lift and drag as long as the aircraft is not in a high lift configuration. For example, in a dynamic soaring trajectory, where the altitude can easily be low in order to capture the maximum strength of the wind gradient, the effect of the ground on the aerodynamic performance can be captured. It is important to note that the ground effects dissipate after 2 to 3 chord lengths, which is already a very critical altitude for a UAV. Therefore, their overall effect on a dynamic soaring cycle may be negligible.

6.2 The Slender Body Theory validation (Case SA-13)

This section looks at the accuracy of ASWING in predicting the lift distribution on a slender body such as a fuselage or an airship (Zeppelin). The steady part in the equation 44 actually derives from the work of Von Karman (1930) and we should invoke the experimental benchmark done to status on the accuracy of ASWING. However, looking at the source code and the technical documentation, only the radius distribution of the slender body needs to be provided. Its variation with the spanwise coordinate $\frac{dR}{ds}$ is computed internally by a first-order backward difference. Or the latter is quite sensitive to numerical noise and diverges rapidly as the mesh is refined, leading to a very noisy distribution. Or both the lift and the source-induced velocity depend on the spatial variation of the cross-section radius. Figures 24 (a), (b) and (c) illustrate such problem of predicting the lift distribution with this method. Three different airships with different aspect ratios ($AR = \frac{L}{2R}$) have been used as the divergence of the numerical discretisation seems to be related to the steepness of $\frac{dR}{ds}$. The same problem is observed for the pressure distribution induced by sources for an axial flow ($\alpha = 0^\circ$). Normally, the circular distribution of the fuselage cross-section is derived from ellipsoid functions which are differentiable in s . Consequently, by implementing a small modification so that the $\frac{dR}{ds}$ distribution is provided instead of computed, large improvements can be observed (cf. blue lines in figure 24 a-d). Note that the problem could be solved on ASWING (unmodified) with a coarser mesh for which the backward difference is more stable. Or a coarser mesh could lead to undesired numerical errors in other physical quantities justifying the change.

From figure 24 (a)-(d) some conclusions can be drawn as the experimental data are shown (adapted from Von Karman and Upson and Klikoff' works). Only the modified version of the ASWING results are

considered. From figures 24 (a) to (c) the lift predictions are in good agreement with the experiments from 0 to 80 % of the airship length. After ($x > 0.8L$) the lift, i.e. the pressure, is overestimated in absolute value by the slender body theory. The pitching moment of the fuselage is then slightly over-predicted. This discrepancy is due to the low-speed profile of the boundary layer, which reduces the pressure on the upper half disc of the fuselage. The slender body theory appears to be sensitive to this as the error increases for airships with lower aspect ratios where a thicker boundary layer is expected. A wall transpiration or displacement model could be used to correct this effect. This would result in a virtual thicker fuselage tail whose cross-section would vary more slowly than the real geometry, resulting in less lift produced. Overall, ASWING gives a good prediction of the lift distribution even at moderate angles of attack. From 24 (d) the source contribution to the pressure prediction is in excellent agreement with experimental data provided by Von Karman (1930). Note that ASWING cannot return the pressure due to the source distribution from the axisymmetry simplification made in the theoretical development (Appendix A). However, it can calculate the source-induced velocity field. Consequently, by judiciously placing numerical sensors on the fuselage surface, the velocity field can be recovered. Thus, by using the steady state Bernoulli equation, the dynamic pressure can be recovered and compared with the 1933 experiments so that the previous comment can be drawn.

Limitation of the Slender Body Theory:

From the previous observations and based on the literature, the limitation of the slender body theory for a good use of ASWING can be drawn. The commented cases are high angle of attack configurations. The ASWING SBT is not able to capture the fuselage rear tail pressure but is still accurate. The limits of the LLT SBT combined are therefore imposed by the wing stall limits of the aircraft. Note that we do not recommend the use of a fuselage with an aspect ratio of less than 6.

6.3 Steady wing-fuselage interference (Case SA-14)

The lifting line and slender body theories have been evaluated separately. They both show good agreement with the experiments. In this section, the interferences between the wing and fuselage are assessed. Indeed, when a wing is anchored to a fuselage, its lift distribution is no longer the same and is slightly distorted. First of all, the fuselage changes the flow field because of the cross component of the upcoming flow denoted

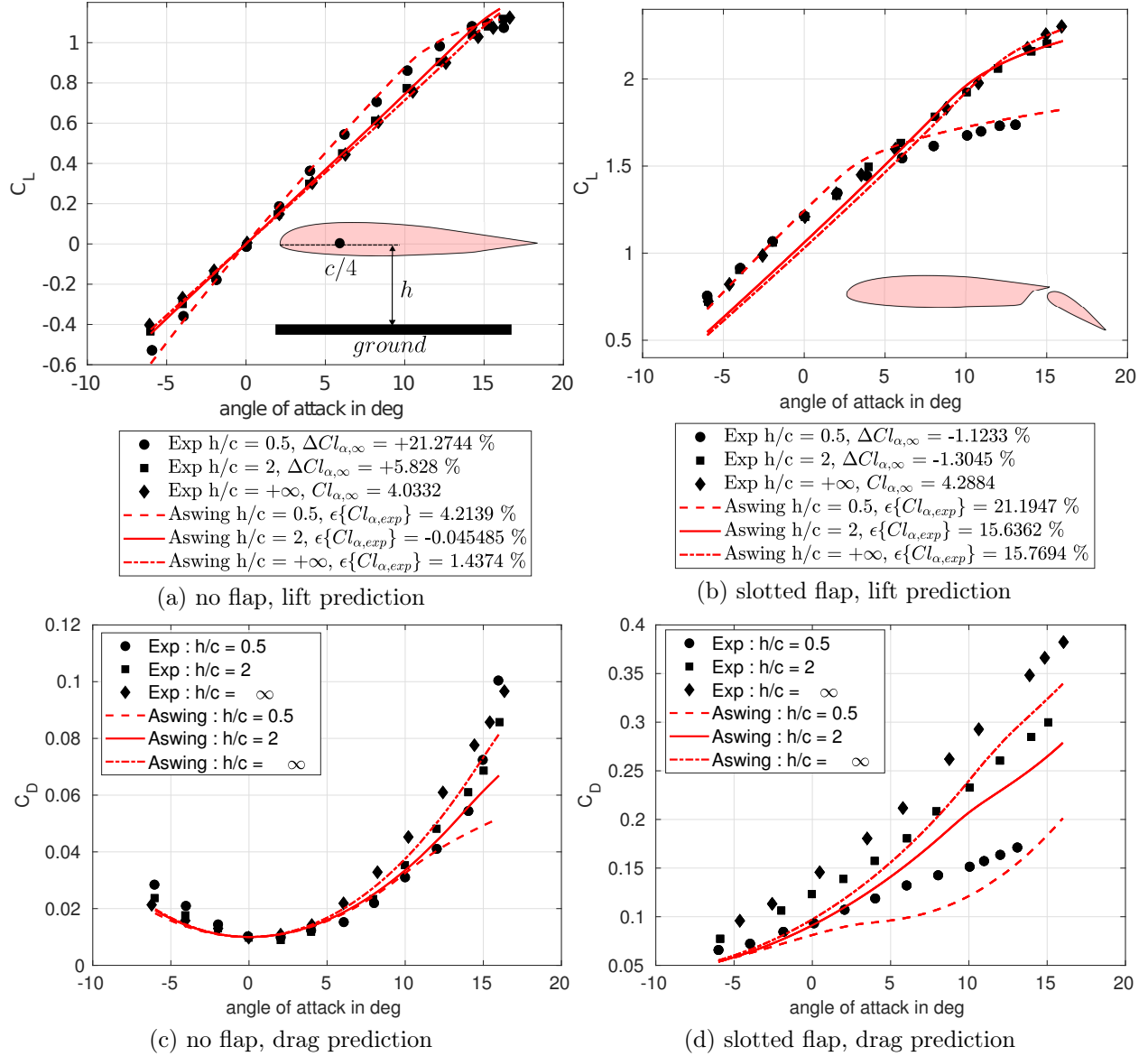


Figure 23: CASE SA-12 A-B: Ground effects on lift and drag predictions on a rectangular wing with no flaps and slotted one. Experimental data adapted from Recant (1939)

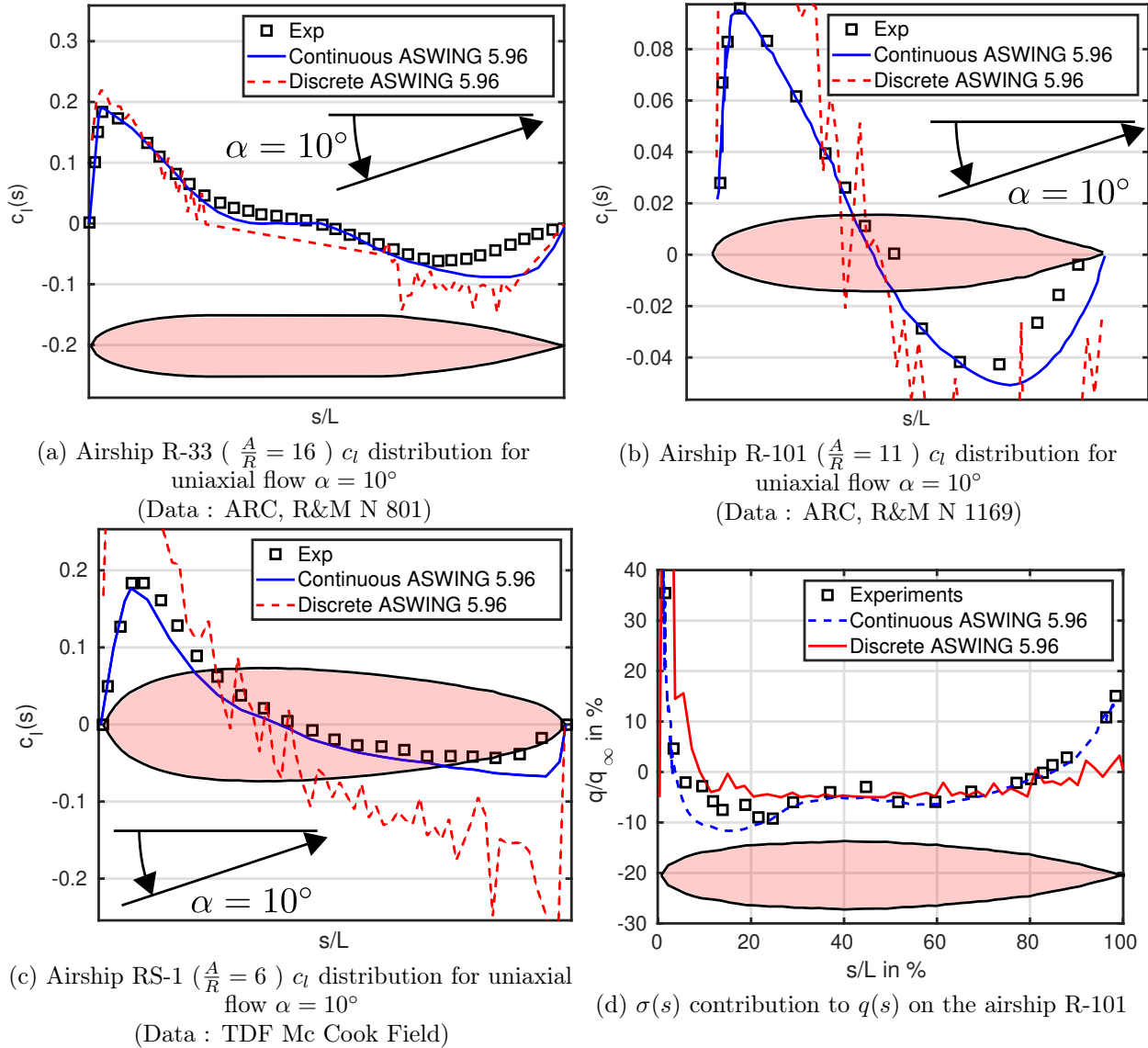


Figure 24: CASE SA-13 A-D: Lift and dynamic pressure distribution ASWING predictions on different airship against experimental data from Von Karman (1930)

as $V_\infty \sin\alpha$. This can be easily modelled through a doublet in which strength ϑ is computed to ensure the impermeability condition on the fuselage cross section (cf figure 25-a). The flow field induced by the doublet tends to increase the angle of attack seen by the wing. So as observed by [Martina-1956](#), a wing connected to a fuselage produces more local lift than the wing alone at the same angle of attack. The second effect brought by the fuselage is the interaction between the wing wake and the body. The latter drastically impacts the aircraft wake vorticity especially at the wing root. A counter root vortex is generated that is not captured by the lifting line alone. Those counter vortices are known to trap the jet exhaust gas, favourable to contrail formations. From a singular method point of view, this counter vortex can be modelled using the Theorem of the circle (cf chapter 3 of [Milne-Thomson-1973](#)) where a set of image vortices are created to ensure the impermeability condition on the fuselage cross-section. This method can be applied to no circular cross section using conformal mapping (cf chapter 5 of [Milne-Thomson-1973](#)) but it is out of the scope of this thesis.

ASWING only models the doublet distribution mentioned above, and so does not capture the wake vorticity change. To evaluate ASWING on this feature the experimental work of [Martina-1956](#) has been used.

Experimental bench :

A 45-degree swept wing of aspect and taper ratio 8.05 and 0.45 was placed into a wind tunnel. The wing was attached to a fuselage whose shape is described in figure 25 (b). A balance was fixed to the fuselage for total lift measurement, while pressure sensor lines, were placed at various spanwise locations (see figure 25 (b)). The wind tunnel speed was 70m/s for an equivalent Mach number of 0.2. Reynolds's number was 4 million. Local lift measurements were performed at 4 different angles of attack but only 3 are presented here (only the one on the linear range). The total lift was measured on a wider range of angle of attack from 0 to 30 degrees. Two configurations were tested, with and without the body. The wing root twist was also changed in the author's work, but this is not presented here.

Numerical bench:

In ASWING, three files have been created, the wing only, the wing + body and the wing + infinite body configurations. The third one has been created to highlight a problem described in the results section. The airfoil (NACA63A0012) polars have been generated by XFOIL at the equivalent wind tunnel condition.

Results:

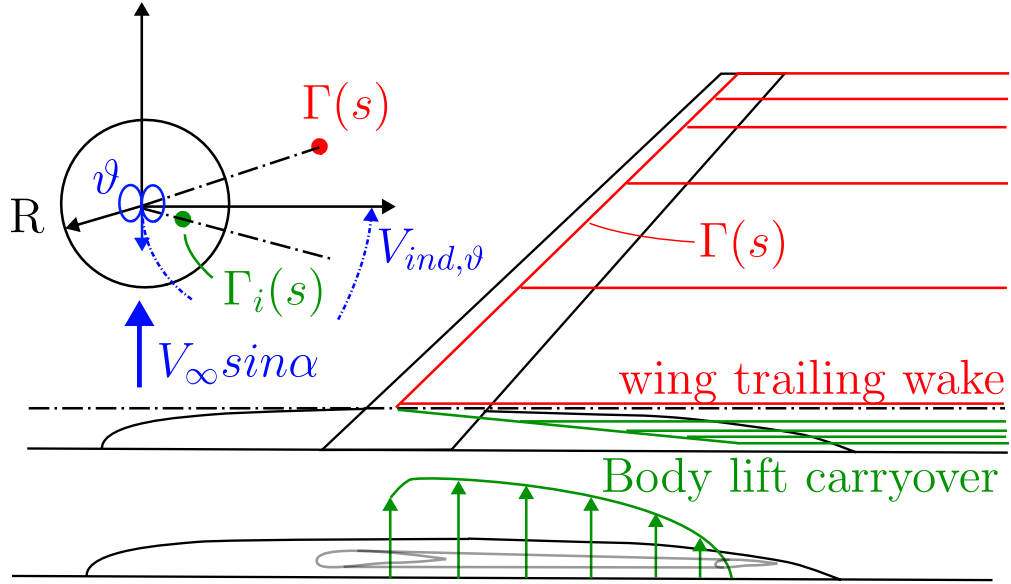
Figures 25 (a) to (c) present the comparison between the ASWING predictions and the experimental mea-

surements of [Martina](#) for the lift distribution. The results are pretty clear, ASWING does not capture the wing body interference. Actually, almost nothing happens when the fuselage is added. The configuration with the infinite fuselage was also tested, and the lift prediction is exactly the same as if the fuselage is not there. Figure 25 (e) particularly highlights this observation for the total lift (green and blue lines are the same). After looking at the source code, it seems that in the induced velocity subroutine, the doublet strength is set to zero, if there is no variation of the fuselage cross section (cf aic.f in subroutine AICVL, the command line: IF(ARAD.EQ.0.0 .AND. DRAD .EQ.0.0)). When this error is corrected, the doublet strength is computed. Results are not presented here, as some instabilities issues (not solved yet) have been witnessed.

In consequence, ASWING should be able to capture the local lift increase due to the fuselage but is not because of encoding issues. Moreover, ASWING is definitively not able to capture the counter root vortex generated by the fuselage and the associated carry-over lift. Discrepancies in the aircraft lift-induced drag predictions are to be expected. By implementing the theorem of the circle of [Milne-Thomson](#), this problem could be solved.

6.4 Lifting surfaces close interaction: rear wing induced upstream curvature (Case SA-15)

A very specific type of interaction can occur on Diamond or joined wings such as the one depicted in figure 26-(a). When two lifting surfaces cross section are near enough, the rear wing can influence the flow curvature of the forward wing because of its own circulation as illustrated in figure 26-(b). This in consequence modify the local lift of the forward wing and can drastically distort it. On a conventional aircraft, the main wing geometry is initially optimised, its wake is computed and prescribe as an upstream condition of the horizontal stabilizer so that it can be optimized. Its effect on the forward wing is neglected as it is far downstream. On joined wings aircraft, both the forward and rear wing must be optimized in the same time as reported and verified experimentally by [Wolkovitch](#) ([48, 49]). He showed that the complete flow field induced by every lifting surface of a joined wing must be solved simultaneously to provide good agreement with experiments where the Prandtl Bi-plane theory is showing weakness in this case. [Wolkovitch](#) also showed that its numerical simultaneous optimisation of the joined wing forward and rear geometry was showing real benefit experimentally.



(a) Modeling wing-fuselage interference using singularities. A doublet is used to ensure impermeability on the fuselage cross section due to the upcoming cross flow component $V_{\infty} \sin \alpha$. If a vortex line $\Gamma(s)$ is present in the cross plane, a imaginary vortex $\Gamma_i(s)$ is lumped into the fuselage. The latter ensures impermeability condition on the cross section. ASWING only use the doublet distribution. The fuselage lift carryover is computed by integrating the Kutta Joukowsky theorem along the (green) lifting line.

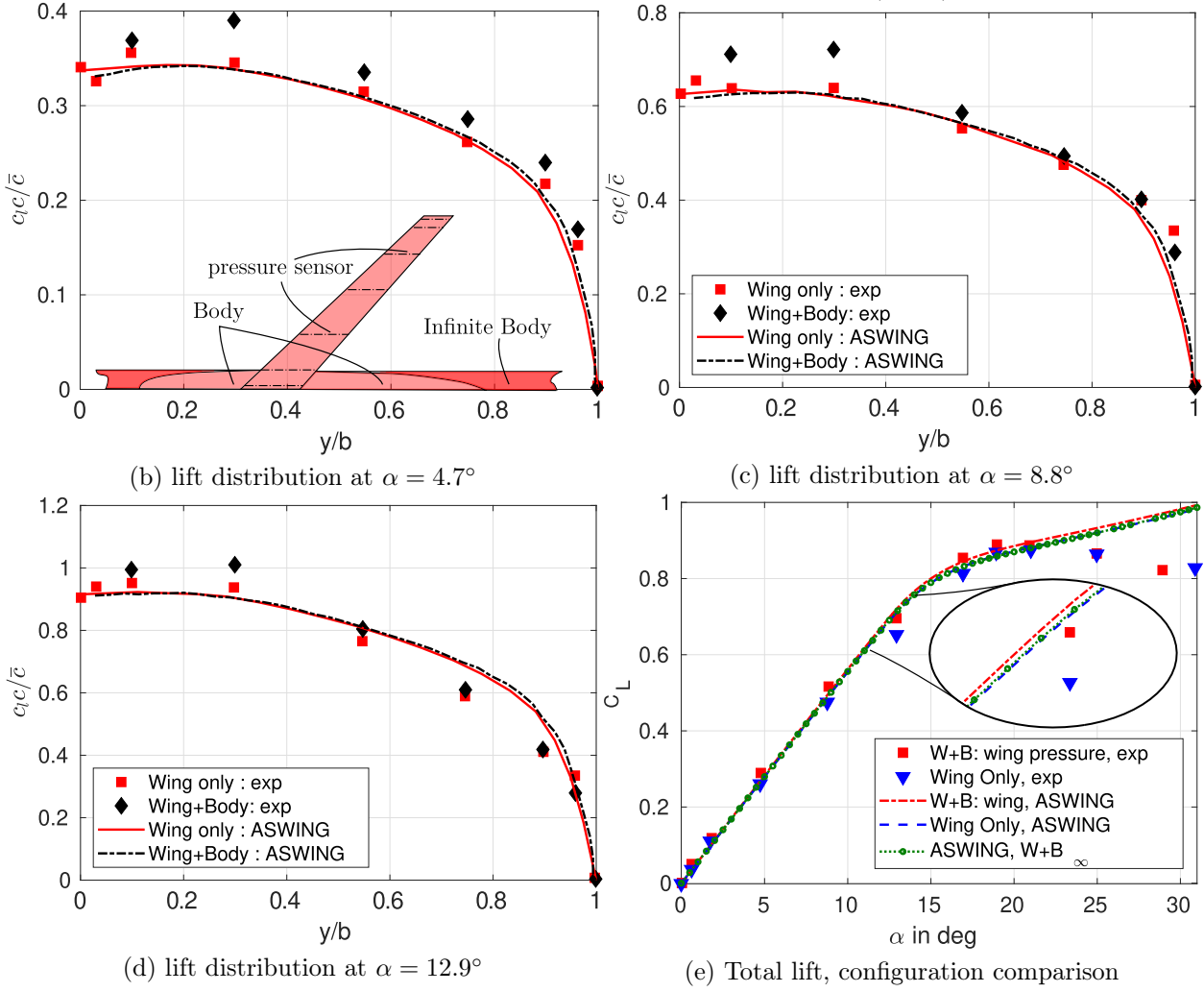


Figure 25: CASE SA-14: Wing body interference illustration and comparison with experiments. ASWING predictions against data from [Martina-1956](#)

Aswing is able to model and solve the flow field induced by numerous lifting surfaces as discussed in the theoretical section. However despite Wolkovitch's numerical model that was a vortex lattice panel method (VLM), Aswing uses a lifting line model (very coarse VLM). Thus the comparison with experiments provided by Wolkovitch ([49]) can not be invoked to assess the Aswing precision on this type of geometries.

Even if the latter are very rare, they present real bene-

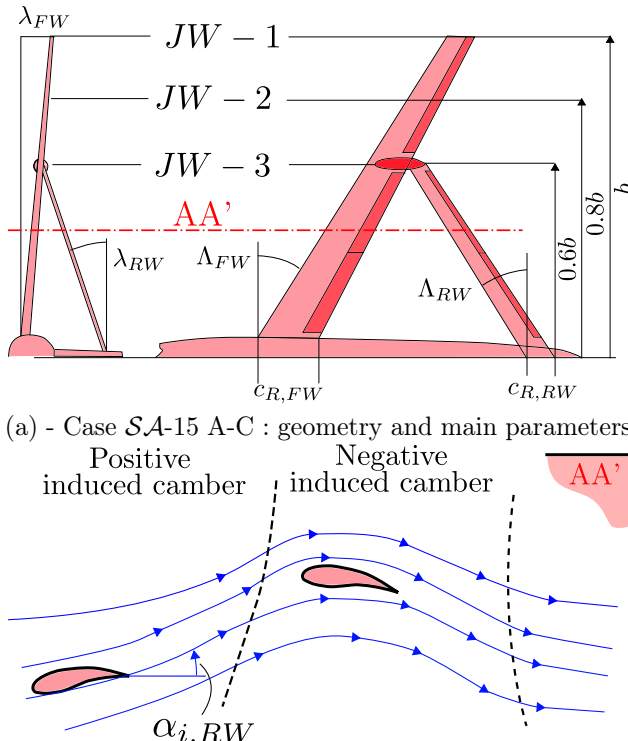


Figure 26: Case SA-15 A-C : Diamond joined wing geometry and proximity effect

fits either from an aerodynamic or weight saving point of view in comparison to conventional wings (tapered swept wings and horizontal stabilizer). Wolkovitch showed particularly that at Iso-structural weight, a diamond joined wing can show significant drag saving. While Kroo et al. has shown that at Iso-aerodynamic performance, a joined wing could provide a structural mass saving of 40%. Predictions also verified experimentally by Lin et al.. Both advantage are incompatible in terms of joint location but a tradeoff can be found. So its important to capture and model accurately both advantages in a framework. Joined wings also delays the flutter onset in comparison to conventional wing as reported by [38] for example. In consequence joined wing, might be a serious candidate for future aircraft design. An evaluation of Aswing on this type of layout is thus proposed, as its main initial

purpose was to be an aircraft pre-design software. To do so, the experimental data of Smith and Stonum have been used. In their work, they studied experimentally the longitudinal/lateral characteristic and controllability of a joined wings aircraft prototype. Three versions of the NASA joined wing prototype denoted as JWRA have been studied and are refereed as JW-1 to 3. Their geometries are illustrated in figure 26 (a) where the only difference in the version is the forward wing span length with JW-3 having the shortest. A complete detail of the geometric parameters and airfoils of each version can be found in table I and II of Smith and Stonum's technical report.

The experiments took place in a 12 foot pressure wind tunnel at a fixed dynamic pressure of $170lb/ft^2$ for longitudinal measurements and $90lb/ft^2$ for lateral measurement because of rolling moment constraint on the measurements balance. The equivalent Reynolds number were $1E6$ and $0.625E6$. The transition of the boundary layer of each lifting surfaces boundary layer were tripped at $0.35c$. Overall, many tests have been performed and every data have been digitalized using webplotdigitalizer. In this report, only the longitudinal characteristic and control of the JW1 to 3 are presented, as too much geometric parameters are missing to model accurately the lateral behaviour of the JWRA prototypes.

Numerically, each bench have been reproduced and XFOIL analysis of each airfoil have been performed at the wind tunnel condition. For more detail please see Appendix E of this report. Figures 26 (a) to (c) present the lift, drag and pitching moment comparison between the Aswing 5.98 predictions and Smith and Stonum's measurements for each JW prototype.

For the lift no matter the version, the Aswing predictions are in excellent agreement with the experiments on the linear range, with a slope error below 7% in the worst case. Aswing also captures the early stall of each configuration. Out of the linear range, Aswing is not able to capture the drop in lift and thus present a constant offset for the upper value of angle of attack for which the lift starts to rise again.

Regarding drag, similar observations as for all the previous single planform cases. Aswing captures well the drag of each configuration as long as a perfect knowledge of the wind tunnel condition is provided. The small rise in discrepancies at moderate angle of attack are due to the constant profile drag coefficient, that has been corrected in our modified version of the code. At post stall angle of attack, Aswing loses the track with the measurements.

For the pitching moment, Aswing captures well

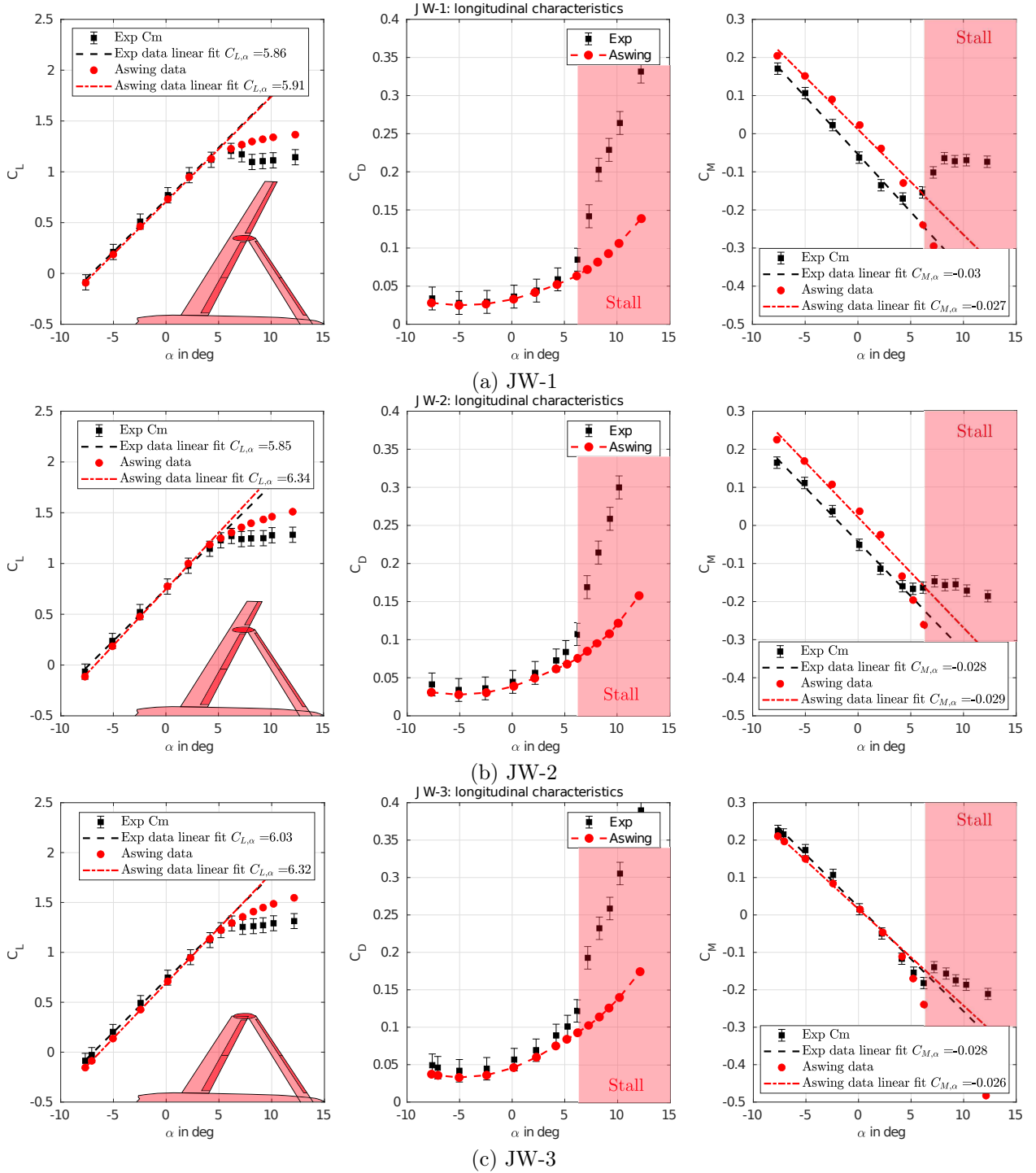


Figure 27: CASE SA-15 A-C : Joined wing JW-1 to 3 longitudinal characteristics. Aswing 5.98 prediction against experimental data from Smith and Stonum-1989

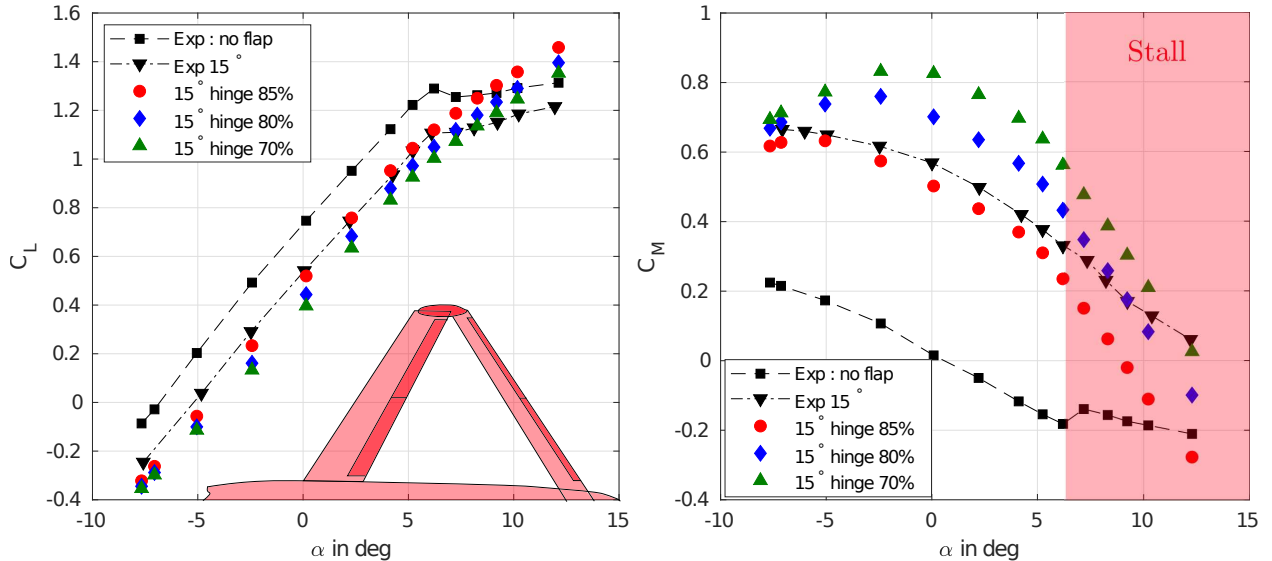


Figure 28: CASE SA-15 C : Joined wing JW-3 Longitudinal control. Rear wing inboard and outboard flap deflected at 15°. Aswing 5.98 prediction for various hinge location against experimental data from Smith and Stonum-1989

the linear moment slope $C_{M,\alpha}$ with the same level of error as for the linear lift slope $C_{L\alpha}$. Thus Aswing will provide good stability prediction. However, on the JW-1 and 2 prototype, Aswing present a constant offset with the measurements while for the third case, the predictions are in excellent agreements.

This is due to the fuselage lift carry over. Indeed as already explained in the fuselage wing interaction section, the fuselage carry a part of the wing lift because the wing flowfield tends to change the pressure distribution on the fuselage cross section. The theorem of the circle states that an antisymmetric imaginary shrunk vortex sheet placed inside the fuselage to ensure a impermeability condition on its section can be used to model this interaction. If the positions of a lifting line segment points are denoted as the complex Z_1 and Z_1 in the (z,y) plane, their image location in the fuselage are given as $Z_{i,1} = R^2/Z_1$ and $Z_{i,1} = R^2/Z_2$ where R^2 . The Kutta-Joukowski theorem is then integrated on the image vortex sheet to get the lift carry over by the fuselage. From the definition of $Z_{i,1}$, the latte scales with $1/Z_1$ so farthest is a vortex segment from the fuselage, smaller its image will be inside it. In the joined wing case JW-1 and JW-2, as the forward wing span is bigger, the lift carry over by the fuselage is lower than the one from the rear wing. This positive difference of lift between the rear and the front wing tend to induce a pitching moment. As the fuselage lift carry over is a direct image of each lifting surfaces lift, the difference in lift is constant with the angle of attack, so the constant offset in the pitching moment. As Aswing is not modelling the fuselage lift carry over, it tends to overestimate the pitching moment of the JW-1 and 2

models. As for the JW-3 the wings spans are equal, no difference in lift is generated by the fuselage, so the good agreements with the experiments. This test case is thus very interesting to show how important can be the effect of the fuselage/wing interference on the longitudinal characteristics of joined wings aircraft. For example, in a pre-design analysis, such an offset in the pitching moment will tend to underestimate the rear wing elevator deflection to trim the aircraft at cruise condition and so underestimate the trim drag.

Smith and Stonum provided measurements of the longitudinal and lateral control derivatives. Unfortunately they did not give the hinge location of each flaps. Or the flap derivatives are very sensitive to it. Thus several XFOIL analysis have been performed for various hinge location that are $h/c = 0.7, 0.80$, and 0.85 . The latter are the most likely to fit the real one from a coarse analysis of the geometry images in the report. Please refer to Appendix E for the XFOIL analysis results. Also only the comparisons on the JW-3 case are presented as, it would accumulate to much error from the pitching moment offset observed on the JW1 and JW2 prototype. Figures 28 left and right present the comparison between the Aswing prediction and the measurements of the effect of a deflected elevator on the lift and moment. It seems that the flap derivatives for the hinge location of 85% provides the best agreements with the experiments for both lift and moment on the linear range. From our analysis on ailerons effects in case SA - 6, those results are quite comforting. However the reader is invited to be carefully about the conclusions as not all the necessary parameters were available. From the latter, assuming that the

lift carry over will be modeled in the future, Aswing should be able to trim correctly Joined wing aircraft with good trim drag predictions.

In conclusion, Aswing captures well the main effect which is dominant on joined wing aircraft that is the change of the forward wing flow curvature because of the rear wing circulation. Aswing can predict well, the lift and drag of such configurations, however, pitching moment tend to be over-predicted when the wing span are different. This offset can be solved by modeling the fuselage lift carry over using the Theorem of the circle previously discussed in this report.

6.5 Unsteady aerodynamics validation (Cases UA-1 to 2)

This section is dedicated to the unsteady aerodynamic validation cases. The 2D case has been retained, despite its very fundamental aspect, because it allows a rigorous comparison between the ASWING model and the Theodorsen formalism. Furthermore, the limitations of these two models are highlighted. By validating the aerodynamic and structural unsteady models separately, it is easier to identify which model is faulty in the case of dynamic and unsteady aeroelastic analysis (flutter, whirl flutter, limit cycle oscillations, etc.). The result is a better identification of the improvements to be made to the model.

6.5.1 Case UA-1: 2D unsteady aerodynamic

To benchmark the ASWING unsteady lift coefficient prediction, the experimental data set presented by Chiereghin et al. (2017b) was used.

Experimental bench: As reported by Chiereghin et al. in sections A and B, the experiments were performed at $Re = 20\,000$ in a closed loop free surface water tunnel with a working section of $0.381 \times 0.508 \times 1.530$ metres. The blade was mounted vertically on a linear motion mechanism. The wing profile and chord are a NACA0012 and $c = 0.0627$ m respectively. It has been designed voluntarily to avoid any structural influence, i.e. it can be considered rigid. To avoid any wing tip vortices and to restore a 2D case, 2 plates have been attached to the root and tip. Both act as symmetry planes, effectively extending the wing span to infinity. Only the plunging motion was studied and followed a sinusoidal function with a reported accuracy of less than 2%. The static wing incidence could be modified, in total 4 different angles of attack were studied ($\alpha \in [0, 5, 9, 15]$) for linear range pre- and post-stall behaviour studies. Transient c_l measurements were made using a balance attached to the diving mechanism. Inertial terms were subtracted from the data set to obtain the 2D c_l first harmonic, denoted \tilde{c}_l , via a Fast Fourier Transform (FFT). The time-averaged 2D \bar{c}_l is also provided. Finally, some Particle Image Velocimetry (PIV) analyses were performed at half-span locations to provide physical insight into the change in the time-averaged lift coefficient. In total, 12 reduced frequencies k and 4 different reduced amplitudes $\frac{a}{c}$ were studied for each wing incidence angle α . In our study, we have decided not to study the highest angle of attack set $\alpha = 15^\circ$ as it corresponds to a post-stall condition. In fact, from the continuous results on the prediction accuracy of the ASWING near and after stall, it is not possible to predict such behaviour as it is not able to capture the drop in lift after stall or

the hysteresis phenomenon. Chiereghin et al.'s data set (2017b) is the most modern we have found in the literature. This data is also particularly interesting as it examines a range of reduced frequencies up to 1, where the error of the ASWING 2D unsteady lift function to Theodorsen's is the most important (cf. Fig. 6). We will finish the analysis by calling Theodore Theodorsen's results (1935) for higher reduced frequencies as both functions tend to be equivalent.

Numerical Methodology: In practice, it is not possible to achieve a perfect 2D case in ASWING. We first tried to increase the span until the 3D effects were negligible, but after a few tests, we noticed a small error in the theoretical function (Eq 29). Therefore, to avoid the accumulation of prediction errors, we decided to compare the experimental data with the theoretical ASWING function augmented with additional mass terms implemented in MATLAB:

$$c_{l,ASW}(t) = (29)$$

$$(c_{l_\alpha} k j C_{ASW}(k) - \pi k^2) \frac{A}{c} e^{j2\pi ft} + c_{l_\alpha} \alpha$$

where $C_{ASW}(k)$ is the 67th equation of [14]. Unsteady lift coefficient $c_{l,ASW}(t)$ is evaluated against Theodorsen's:

$$c_{l,\text{Theodorsen}}(t) = (30)$$

$$(2\pi k j C_{\text{Theodorsen}}(k) - \pi k^2) \frac{A}{c} e^{j2\pi ft} + 2\pi\alpha$$

Note that the equations 29 and 30 are only valid for plunging motion. Both second terms in parentheses account for the added mass term. The term in brackets in both equations represents the first harmonic of the signal. Its amplitude \tilde{c}_l and decay ϕ_{c_l} can be calculated directly if $C_{ASW}(k)$ and $C_{\text{Theodorsen}}(k)$ are known. The time averaged lift coefficient \bar{c}_l is simply $c_{l_\alpha} \alpha$ and $2\pi\alpha$ in 29 and 30. Finally, in both equations ϕ_{c_l} does not depend on the reduced amplitude, so the results for the phase lags are only a function of the reduced frequency.

Results and comparison with Theodorsen theory:

The first harmonic \tilde{c}_l predictions are shown in figures 29(a), 30(a) and 31(a). When the wing has no root incidence ($\alpha = 0^\circ$), both Theodorsen and ASWING \tilde{c}_l are in excellent agreement with the experiments. Note that despite the error between Theodorsen's lag function and ASWING, the difference in prediction is not so obvious. At $\alpha = 5^\circ$ (Figure 30 (a)) the agreement is still good over the whole reduced frequency and amplitude range. However, near the stall angle of attack ($\alpha = 9^\circ$) both functions become weaker but still reasonably accurate. Near the stall, the flow around the airfoil is more likely to be detached, especially at low reduced frequencies. Or in

this region the circulation terms in the equations 30 and 29 dominate and are derived from an attached flow assumption. This phenomenon is particularly emphasised at high reduced amplitudes as shown in figure 31(a). After $k = 0.6$ the apparent/added mass terms become dominant and "the forces depend more on the pressure field of the airfoil and less on the flow separation" as claimed by the author. As a result, both theories become accurate again at high reduced frequencies.

There is less comment on the predictions of the phase lag ϕ_{c_l} . Both the Theodorsen and ASWING theories show good agreement regardless of the angle of incidence of the airfoil, as shown in figures 29(b), 30(b) and 31(b). The small discrepancies at lower reduced frequencies are explained by the author as a lack of accuracy of the balance as the perturbation lift is very small. Overall, it is quite difficult to judge which theory performs best for phase lag prediction, so we will consider them equivalent in this frequency range.

Time average displacement due to Leading Edge Vortices (LEV):

The analysis could stop there and conclude that both ASWING and Theodorsen have similar performance in predicting reasonably well the amplitude of the first harmonic of lift and the displacement up to the wing stall. However, when looking at the time average of lift as a function of reduced amplitudes, frequencies and angle of attack as shown in figure 36(a). There is an unsteady frequency phenomenon which leads to a positive or negative offset in the time average lift which is not captured by either the ASWING or Theodorsen formalism.

Phase average results:

According to the shape of the phase average lift (Figure 32 (a)-(f)), the LEVs have a higher bandwidth than the pluning frequency. Neither ASWING nor Theodorsen functions can predict them. For aeroelasticity analysis, this would not necessarily be a problem as they would excite higher frequency modes which are usually less dominant in the transient response of the structure. In reality, the biggest problem caused by leading-edge vortices is the positive or negative offset in the time average lift. In the case of a flutter analysis, this would lead to an over- or under-estimation of the lift, i.e. the flutter boundary. Figure 32(b), (c), (e) and (f) show modified theories that assume the time average lift offsets are known. Under this strong assumption, ASWING is able to correctly predict the peak-to-peak amplitude. We consider this hypothesis to be too strong and stick to the conclusion that for low Reynolds number flow at high angle of attack and Stouhal number, ASWING and Theodorsen are more likely to underpredict the peak-to-peak lift amplitude and the time average lift.

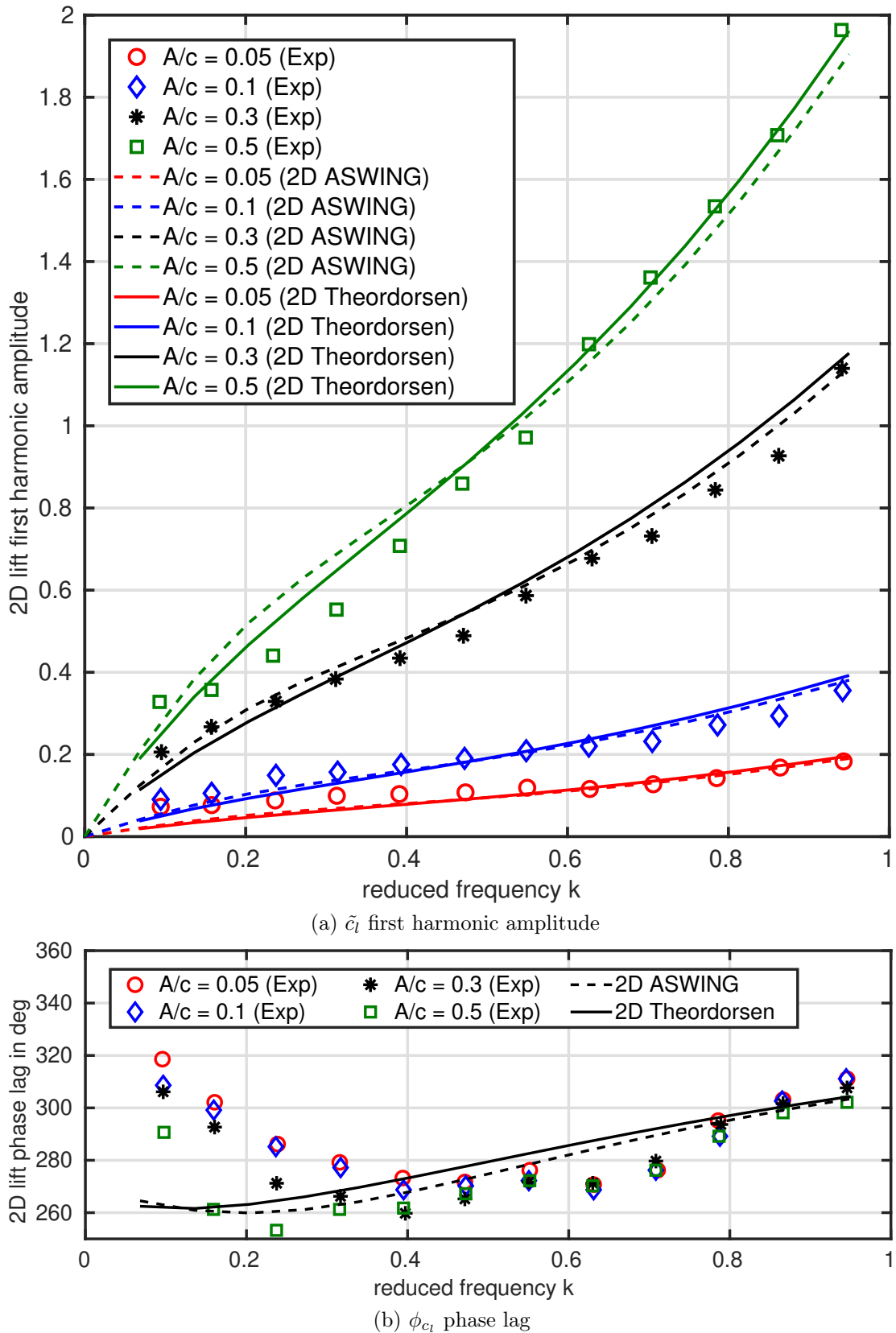


Figure 29: Case UA-1: 2D lift coefficient first harmonic amplitude and phase lag at $\alpha = 0^\circ$, effect of the reduced amplitude and frequency. ASWING prediction comparison with experiments (Chiereghin et al. 2017b)

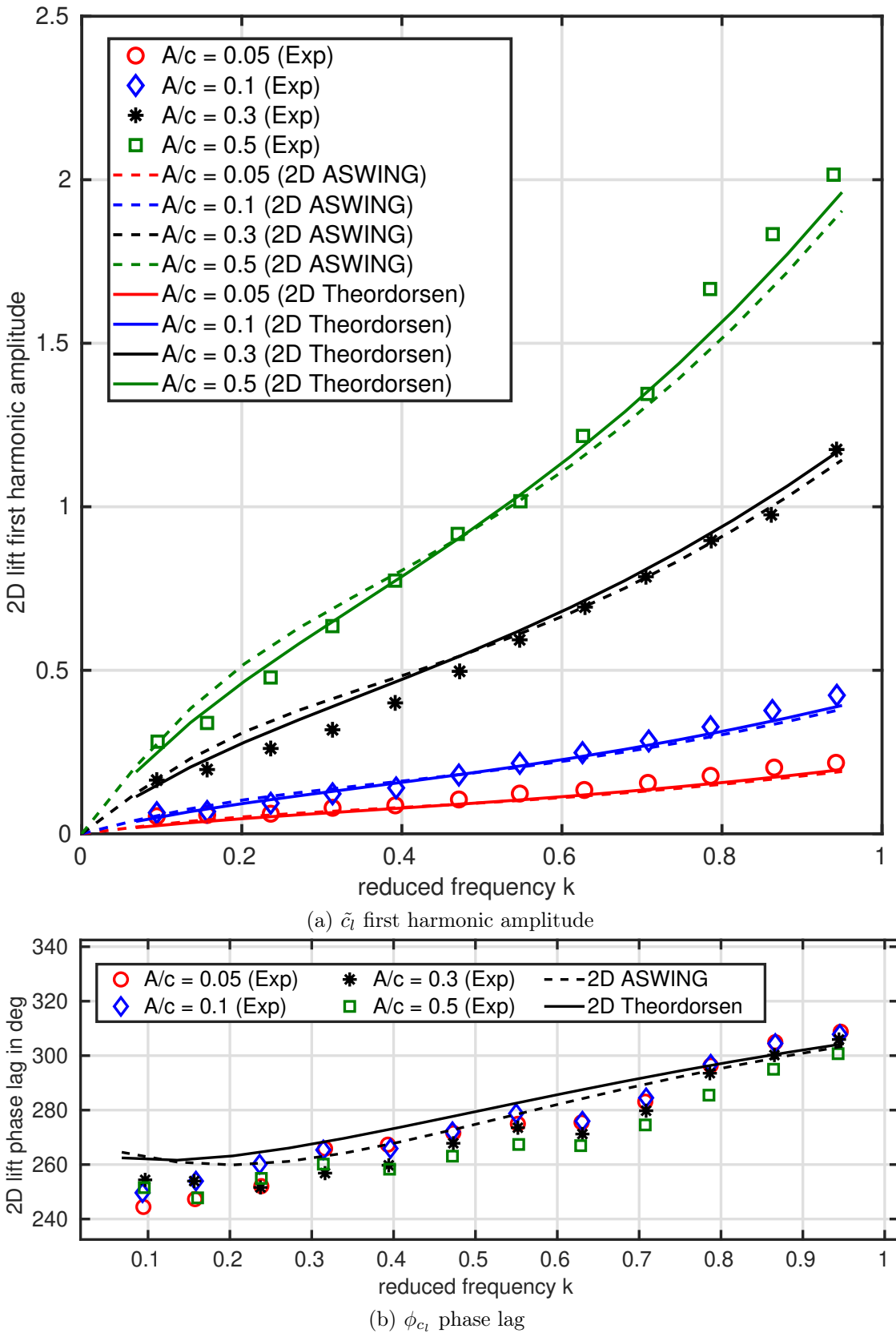


Figure 30: Case UA-1: 2D lift coefficient first harmonic amplitude and phase lag at $\alpha = 5^\circ$, effect of the reduced amplitude and frequency. ASWING prediction comparison with experiments (Chiereghin et al. 2017b)

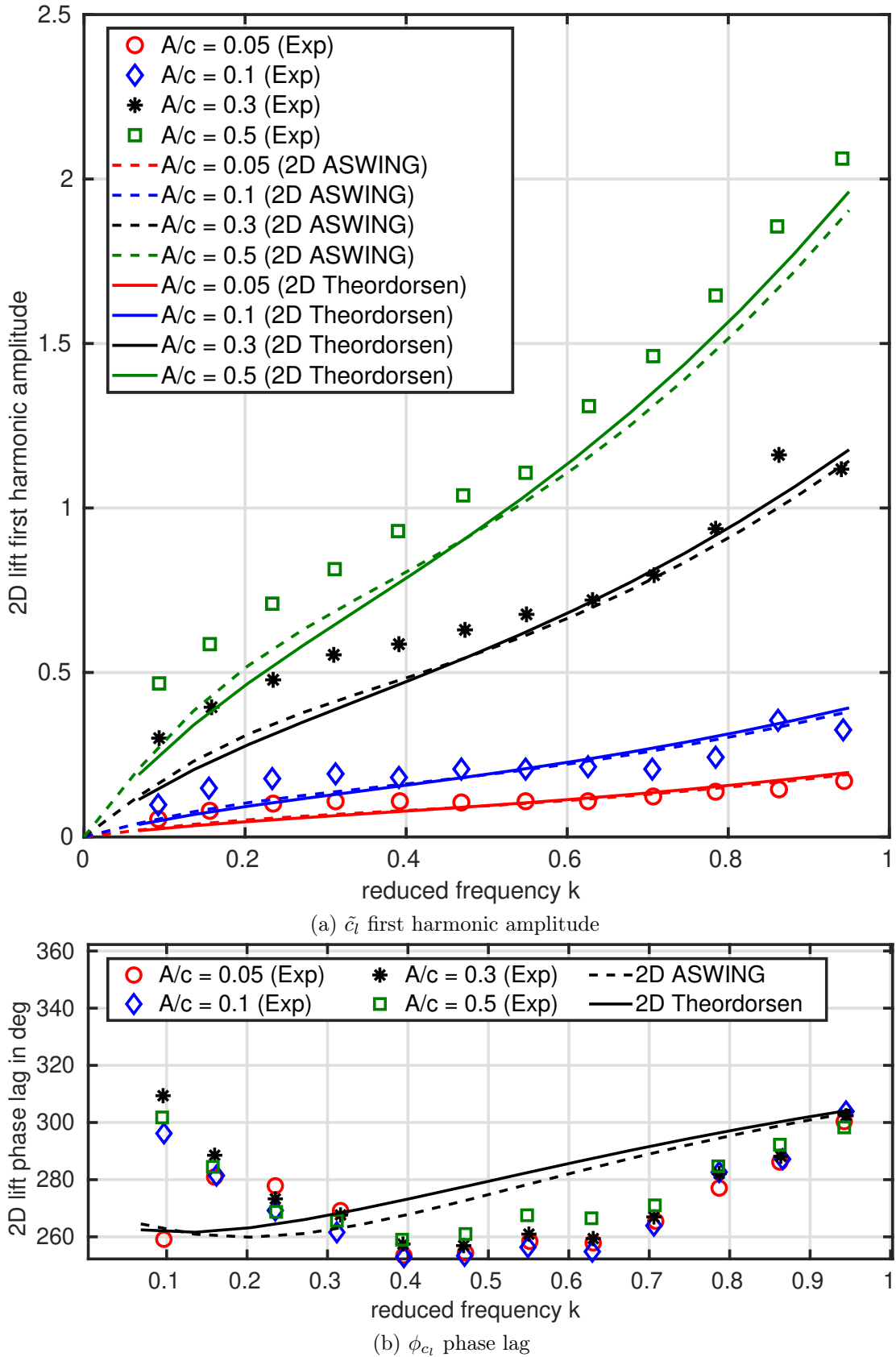


Figure 31: Case UA-1: 2D lift coefficient first harmonic amplitude and phase lag at $\alpha = 9^\circ$, effect of the reduced amplitude and frequency. ASWING prediction comparison with experiments (Chiereghin et al. 2017b)

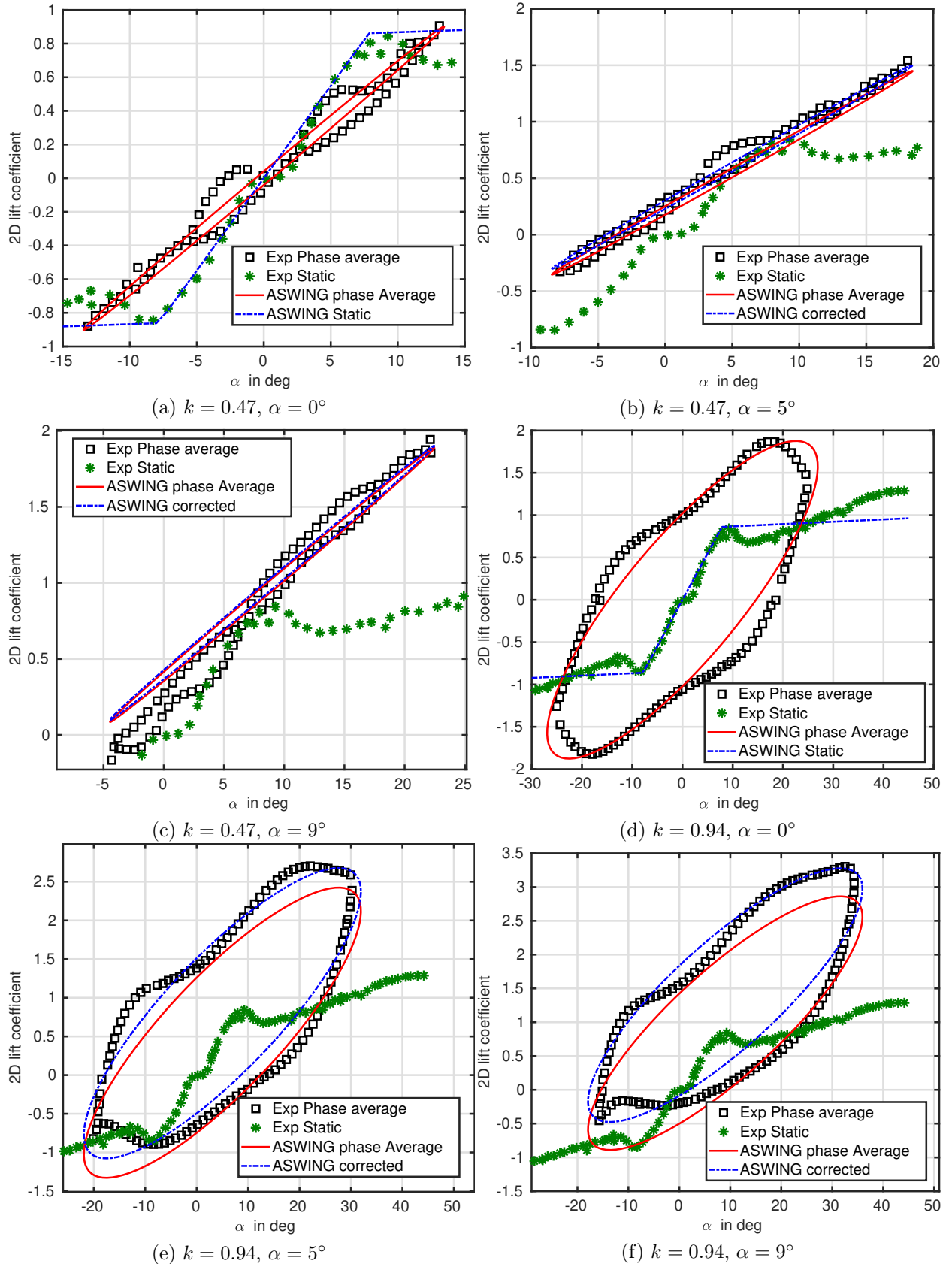


Figure 32: Case UA-1: Phase lag average for 2 reduced frequencies and 3 angles of attack. ASWING predictions versus experiments (Chiereghin et al. 2017b). Comparison with a corrected function taking into account the time average experimental data.

6.5.2 Case UA-2: 3D unsteady

The unsteady 3D aerodynamics has been studied using the experimental data from Chiereghin et al. (2017a).

Experimental bench: The experimental bench is the same as in the 2D case except that the end plate has been removed. Enough space was left between the water tunnel wall and the wing tip to ensure the development of tip vortices and to correctly capture the 3D effects. Note that the aspect ratio of the wing is 5, which makes this set a stress test for the lifting line. The author's paper presents the time average, first harmonic amplitude and phase lag of the lift. 3D PIV analyses are also provided for physical insight into the 3D leading edge vortex development. Finally, phase average lift analysis was not performed. The same angle of attack reduced amplitudes and frequencies were investigated.

Numerical Methodology: Despite the 2D case, this time it is not possible to implement a theoretical function in MATLAB for the variation of the lift. Consequently, offline simulations were not possible and each case has to be run under ASWING. A slight modification of the code has to be made in order to be able to prescribe a plunging motion. Mesh and time convergence have been studied and we have used 40 circulation nodes and a time step $Te = T/40$, where T is the equivalent period of the reduced frequency to be studied. To save computational time, we ran the simulations over a single period. Instead of performing an FFT analysis, the time average was obtained by calculating the mean value of the signal, the peak-to-peak value was obtained by spotting the minimum/maximum values, and the phase lag was obtained by spotting the temporal position of the first maximum peak. This has been compared with a multi-period FFT analysis (10) and similar results have been observed. This holds as long as the march step is small enough, which is our choice. In the post-processing, we have highlighted that the phase lag does not vary with the reduced amplitude, so as in the 2D case, it is presented as varying only with the reduced frequency.

Results: The time averaged lift coefficient predictions are shown in figure 36(b). Offset is still present at moderate to pre-stall angles of attack, but as reported by the author, the leading edge vortices have been damped by the 3D effects. The induced velocity tends to reduce the effective angle of attack, delaying the appearance of LEVs. 3D cases appear to be less sensitive to Leading Edge Vortices for the same range of parameters. However, we do not recommend using it for near-stall configurations and high Strouhal number unsteady flows as the offset is still quite large.

The first harmonic amplitude function of the reduced amplitude, frequency and angle of attack are shown in figures 33, 34 and 35 (a). Comparisons are made with Theodorsen's 2D function. For high reduced amplitudes (0.3, 0.5) ASWING agrees better with experimental data than Theodorsen, especially at high reduced frequency. When the angle of attack reaches 9°, the conclusion is no longer straightforward. Especially at a moderately reduced frequency (0.3 to 0.6) ASWING seems to underestimate the peak-to-peak amplitude of the lift. Note that by making a small correction to the 2D Theodorsen function using a 3D corrected lift slope, we obtain similar results to ASWING. However, the latter remains more interesting as it provides information on the aerodynamic spanwise force distribution, which is essential for aeroelasticity analysis. The phase lag predictions are shown in figures 33, 34 and 35 (b). The conclusion remains the same, at small Stouhal numbers (i.e. small k and $\frac{a}{c}$) discrepancies are due to sensor resolution. Otherwise, both ASWING and Theodorsen show good agreement with experimental data, whatever the angle of attack.

Recommendations: From the 2D and 3D validation cases we can draw conclusions about the prediction quality of ASWING. It shows excellent agreement with experiments for a range of Strouhal numbers when the wing incidence is in the non-stall region. Near stall ASWING still provides interesting results, but the results have to be interpreted carefully.

7 Computational performance

To evaluate the computational cost of ASWNG, the work of Fernandez-Escudero et al. (2019) has been used (with more details *in chapter 4* of the PhD manuscript of ESCUDERO). Theodorsen computation times against higher fidelity solutions were provided by the author. The tests were performed on the same single-core machine. The processor used was an Intel i7-3970K with an assumed clock speed of 3.8 GHz. All simulations were performed in 2D configurations over 10 pitch/plunge cycles. A comparison with the ASWING performance is proposed in the table 6. The programming language is also given for each case. The ASWING tests were carried out on a single core of an Intel Core i57360U with a fixed clock speed of 2.8GHz (lower than the i7-3970K). For medium to high fidelity codes (UVLM, Euler NLFD, Euler DTS, URANS NLFD), mesh and time step convergence studies were performed and reported by the author. Despite this tab sums up the computational cost for the 2D case, we have studied the 3D case of the previous section and implemented

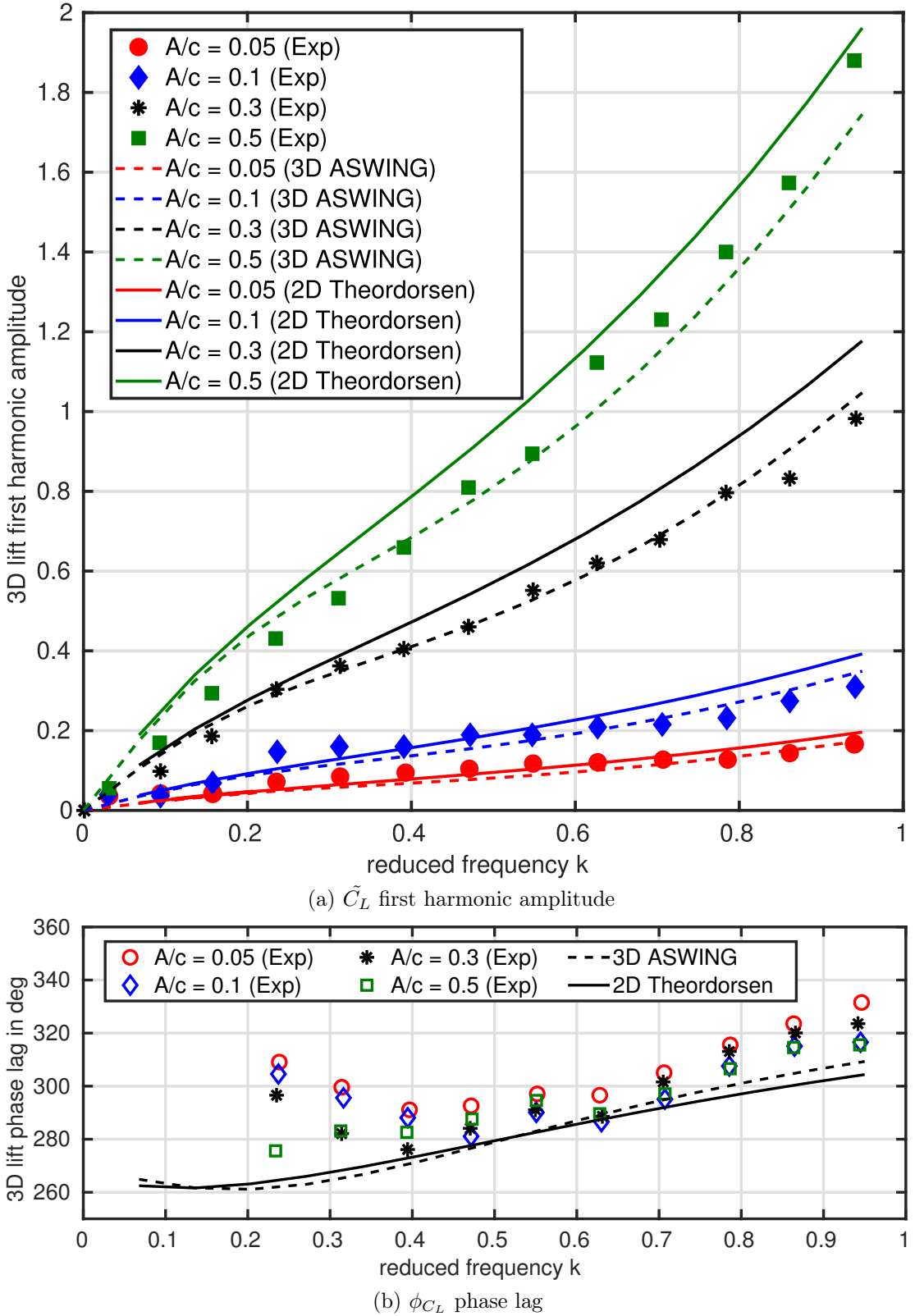


Figure 33: Case UA-2: 3D lift coefficient first harmonic amplitude and phase lag at $\alpha = 0^\circ$, effect of the reduced amplitude and frequency. ASWING prediction comparison with experiments from Chiereghin et al. (2017a)

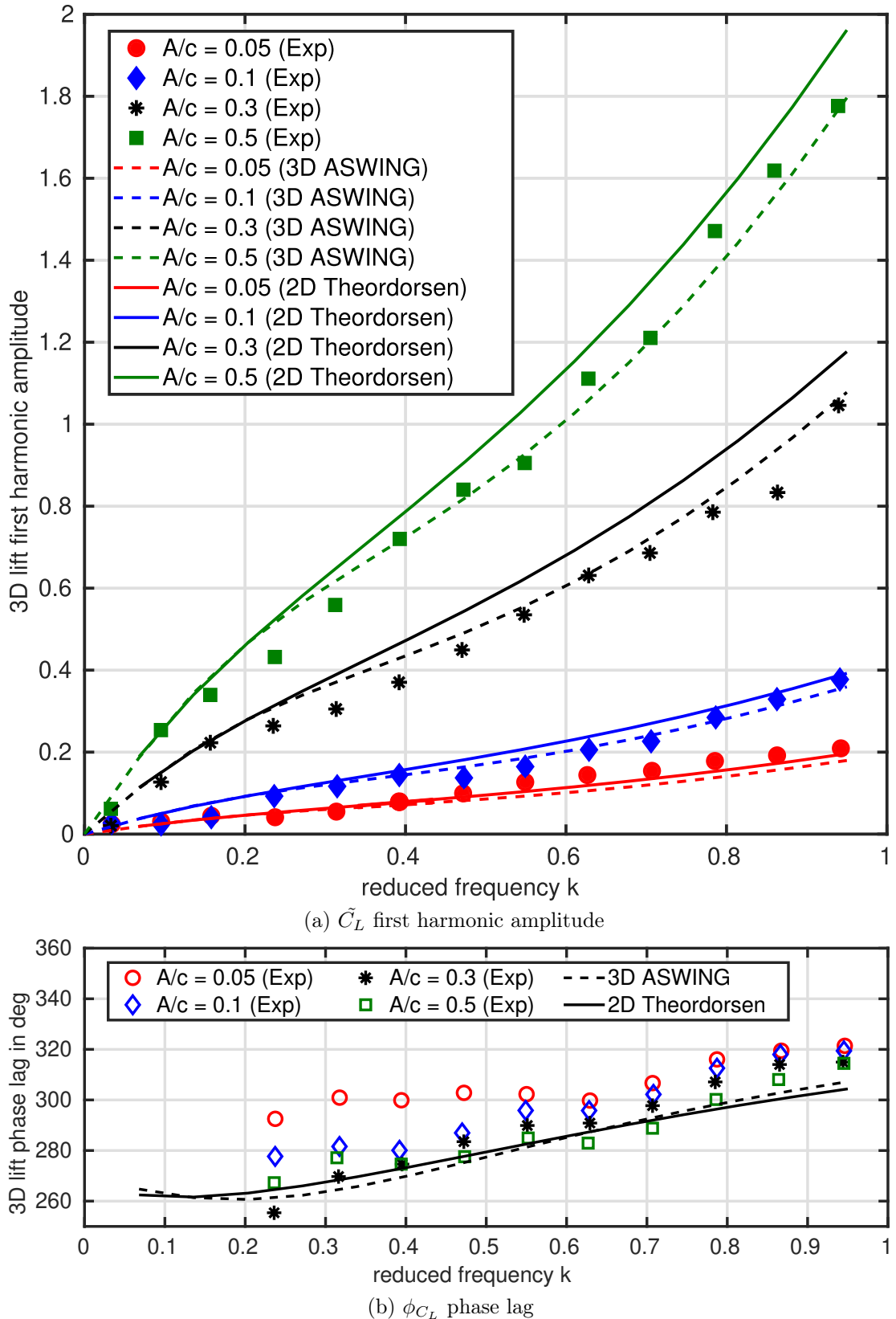


Figure 34: Case UA-2: 3D lift coefficient first harmonic amplitude and phase lag at $\alpha = 5^\circ$, effect of the reduced amplitude and frequency. ASWING prediction comparison with experiments from Chiereghin et al. (2017a)

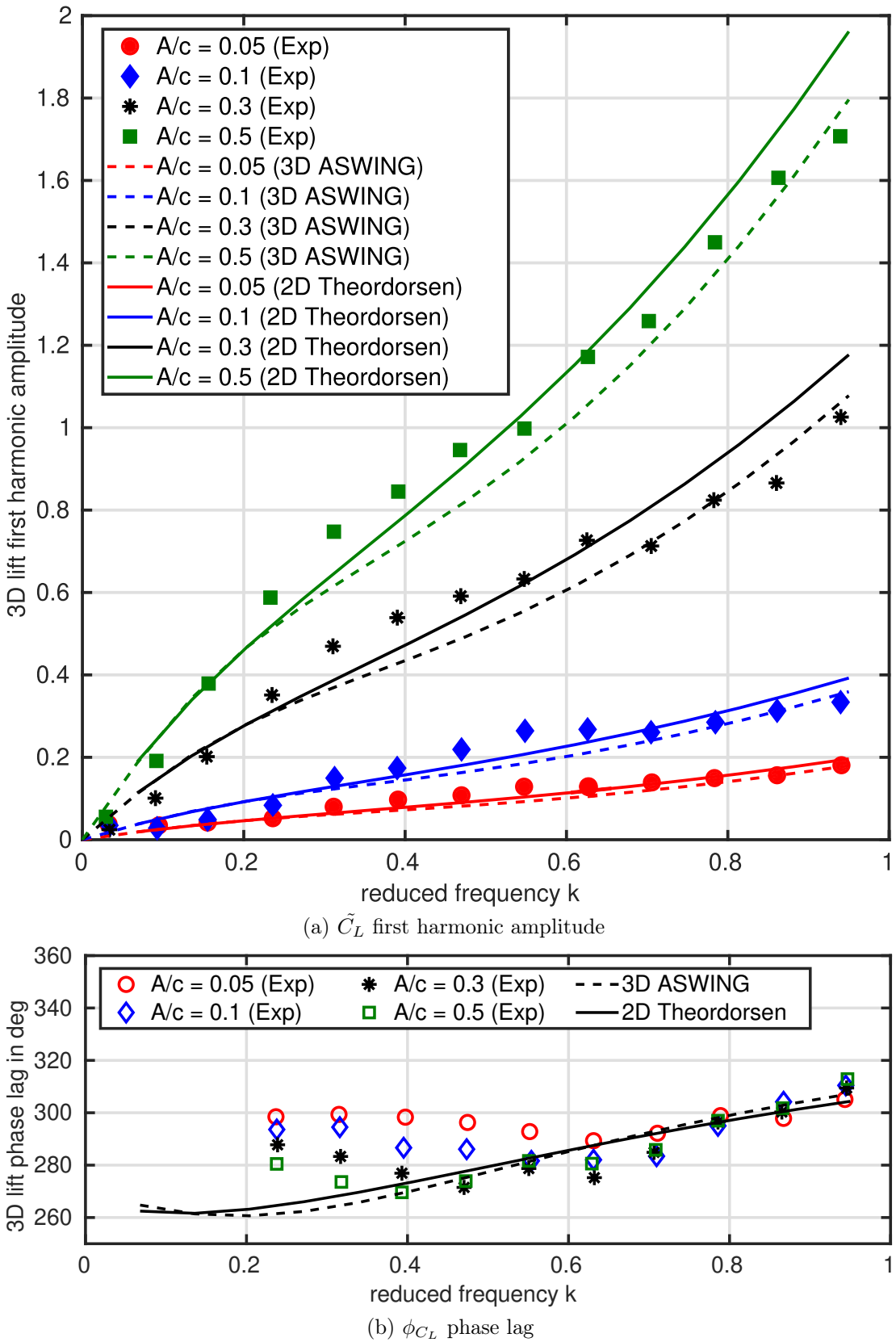


Figure 35: Case UA-2: 3D lift coefficient first harmonic amplitude and phase lag at $\alpha = 9^\circ$, effect of the reduced amplitude and frequency. ASWING prediction comparison with experiments from Chiereghin et al. (2017a)

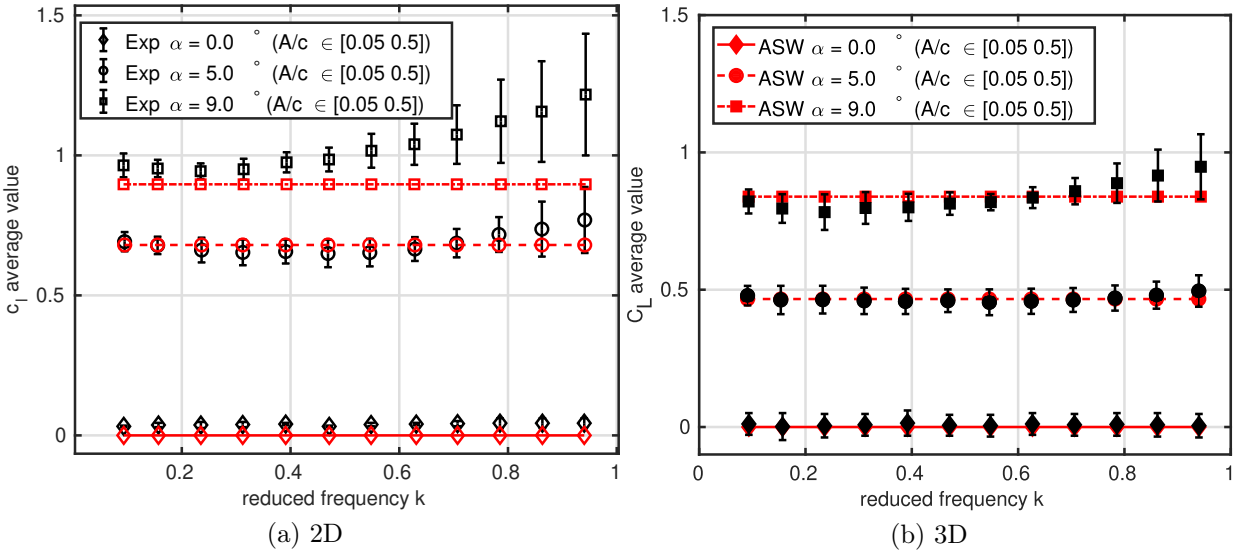


Figure 36: Case UA-1&2: Leading Edge Vortices effect on the time average 2D and 3D lift coefficient versus ASWING predictions. Comparison with experimental data from Chiereghin et al. 2017b and 2017a

the flexible dynamics of the wing. Forty structure nodes and 40 circulations variables were sufficient to obtain a good mesh convergence. The time step used in the previous section was also sufficient. Given the table, ASWING is very attractive as it is very efficient. There is a difference of 2 to 3 orders of magnitude with the 2D unsteady vortex lattice method, which cannot model leading edge vortices but only a nonlinear free wake. In other words, if the objective is only to study the effect of unsteady aerodynamics on the whole aircraft structure or vice versa, and we stay within the assumptions of ASWING, the latter is an excellent solution to perform heavy parametric studies such as multi-disciplinary analysis and optimisations.

8 Conclusions

In this report, an experimental evaluation of the ASWING aerodynamic model has been carried out. The various results are summarised as follows:

- ASWING can correctly capture the total lift and drag coefficients of various single planform geometries up to the early stall. The linear lift coefficients are in good agreement with the experiments.
- The drag prediction can be slightly improved when 2D airfoil polars are considered in a viscous loop, taking into account the quadratic variation of 2D viscous and pressure drag coefficients with lift. The quality of the predictions is strongly dependent on the airfoil polars. Important knowledge of the flow and experimental con-
- ditions is essential to obtain results equivalent to those presented. For real flight conditions, some discrepancies must be expected.
- ASWING can correctly capture the rolling moments induced by different ailerons on a straight wing for moderate flap deflections (up to 20 degrees). For larger deflections, ASWING detects a tendency but overestimates the rolling moment. When the wing is in a post-stall condition, the predictions are no longer accurate. In linear and post-stall conditions, ASWING underestimates the yaw moment generated by the ailerons, mainly because it cannot capture the increase in viscous and pressure asymmetric drag generated by sharp geometries.
- ASWING can capture the wake interactions between multiple lifting surfaces. In particular, it correctly predicts the loss of lift of a downstream surface due to a strong wake downwash. It also provides good predictions of the stall of each surface.
- The lift distribution prediction has been investigated on various swept forward and backward wings. The ASWING predictions are in good agreement with the experiments. It captures well the effect of the sweep angle on the spanwise displacement of the aerodynamic centre of the wing.
- The effect of wingtip devices on lift-induced drag is well captured as long as the wingtip is a single lifting surface. When tip sails are considered, ASWING shows significant discrepancies with experiments. Otherwise, it captures well the

Table 6: Computational time comparison with higher fidelity methods adapted from the work of Fernandez-Escudero et al. (2019)

Method	Language	Computational time (in s)
Theodorsen 2D	Matlab	30
ASWING 2D	Matlab	30
ASWING 3D	Fortran 77	60
UVLM (2D)	C++	2.7E3 ~45 min
Euler NLFD (2D)	C++	2.1E5 ~ 6 h
Euler DTS (2D)	C++	2.8E5 ~ 6h
URANS NLFD (2D)	C++	8.6E5 ~ 1 day

order of magnitude of the drag reduction in cruise conditions.

- Transonic flow has been studied. Thanks to the Prandtl-Glauert compressibility correction factor, the lift slope of a commercial airliner wing is reasonably well captured. For drag, ASWING is weak and does not capture the strong dependence on the Mach number. However, the source code could be modified to account for transonic airfoil polars as a polynomial function of lift coefficient and Mach number. The use of MSES is recommended as it provides a decomposition of the drag into pressure and viscous contributions which is consistent with the ASWING formalism.
- The ground effects on lift and drag can be captured for a wing with no slotted flaps deployed. The increase in lift slope and decrease in drag are well predicted for altitudes up to half the wing chord from the ground. For configurations with slotted flaps, the effects of the ground on the flap physics are dominant and are of course not captured by ASWING. Therefore, this function must be used with caution.
- Thanks to the slender body theory, the lift distribution on the fuselage with a circular cross-section is well captured, except near the tail where flow separation usually occurs. As a result, ASWING overestimates the pitch-up moment induced by the fuselage. The slender body theory gives excellent results for flow deflection.
- ASWING should be able to capture the local lift increase due to the fuselage but is not because of encoding issues. Moreover, ASWING is definitively not able to capture the counter root vortex generated by the fuselage and the associated carry-over lift. Discrepancies in the aircraft lift-induced drag predictions are to be expected. By implementing the theorem of the circle of Milne-Thomson, this problem could be solved.

- 2D unsteady aerodynamics have been studied. For a plunging wing, ASWING performs similarly to Theodorsen's theory, regardless of the reduced frequency and amplitude considered. Both capture well the pick-to-pick amplitude and the phase lag of the lift. However, when the airfoil has a significant incidence and faces a high reduced frequency or amplitude, leading-edge vortices appear. The latter, appearing on only one descending phase (down), modifies the mean value of the lift, which is not captured by ASWING or Theodorsen theory, as they are boundary layer phenomena.
- For 3D unsteady aerodynamics, the same remark can be made as for the 2D case. However, ASWING seems to capture the peak-to-peak amplitude of lift better than Theodorsen theory because it captures the 3D lift effects. This change is attenuated at higher reduced frequencies and amplitudes as the added mass terms dominate.
- In terms of computational time, ASWING is 2-4 orders of magnitude faster than higher fidelity models, and in terms of prediction quality, ASWING can clearly compete with them for macroscopic physical variables predictions (lift, drag, pitching moment etc).

This work has allowed us to converge on bounded parameters that ensure good predictions. The wings and fuselage must have an aspect ratio greater than 5. The wings must have a dihedral and sweep angle of less than 45 degrees. It is also recommended not to abuse the use of the stall function, as it will deteriorate quickly. Finally, it is recommended to consider flows with an average Reynolds number higher than 100 000 (typical for mini UAVs). In its current version, care must be taken with the predictions made in the transonic condition. Under this perspective, several modifications of the ASWING source code could be considered and are summarised as follows

- Close lifting surface interactions can be improved to more accurately model wing/body interactions. The theorem of the circle and conformal mapping could be adapted to the ASWING formalism.
- Transonic airfoil polars could be integrated as bi-polynomial functions of local lift coefficient and freestream Mach number to provide more accurate lift and drag predictions, thus extending the range of ASWING to transonic flight.
- An axisymmetric boundary layer model could be implemented in the slender body theory to capture the flow separation at the tail. For example, a wall transpiration model could be used to reasonably increase the computational cost. It would give better predictions of fuselage drag and pitch-up torque.
- The slender body theory could be extended to non-axisymmetric bodies in order to model double bubble fuselages such as the one of Aurora D8. Again the theorem of circle and conformal mapping could be used to solve it.
- A prescribed helicoidal wake could be integrated, extending and allowing the study of flexible rotor blades.

As far as the funding is concerned, ASWING answers all the numerical aerodynamic needs of the thesis and even more. It is perfectly suited to multidisciplinary analysis. In the next report, the propeller model is studied and coupled with the aerodynamic model to provide more analysis capabilities.

Appendix A: Unsteady vectorial formulation of the slender body theory

This section aims to provide some theoretical insight into how aerodynamic unsteady forces are derived in Drela's work (2008 and 2009). The latter considers only a fuselage with symmetry of revolution, i.e. a circular cross-section. From the unsteady Bernoulli equation, we know that the local pressure in the flow field can be expressed as a function of the local dynamic pressure and the time variation of the velocity potential, as long as they are known. The aerodynamic forces acting on a fuselage are calculated by integrating the normal pressure contributions. Note that the aerodynamic model is coupled to a structural model. In other words, the geometry of a fuselage can vary with loads. Consequently, the slender body theory must be derived in a distributed form.

The unsteady slender body theory is derived from 2 main assumptions:

- The cross-sectional area varies slowly with the spanwise coordinate s , implying that the flow is mostly 2D.
- The slender body theory assumes that the incoming flow of velocity V at each disc centre is constant over the cross-section.

Consider a slice of a fuselage of length ds immersed in a fluid of velocity V . The geometry imposes an impermeability, i.e. a flow tangency condition, on the elementary surface. Let us denote by V_{\perp} the component of the local velocity lying in the cross-sectional plane (c, n) , expressed as $V_{\perp} = \vec{V} - \vec{V} \cdot \vec{s}$ and shown in figure 7. Note that $\vec{V} \cdot \vec{s}$ is the projected axial velocity. For convenience, we now define a new local cross-section frame $(c_{\perp}, s, n_{\perp})$ such that the cross-section velocity \vec{V}_{\perp} is aligned with n_{\perp} , i.e. $\vec{V}_{\perp} = V_{\perp} n_{\perp}$. To ensure tightness we use 2 types of singularities. A source of strength $\sigma(s)$ to ensure the tightness of the projected normal velocity component of the axial velocity $\vec{V} \cdot \vec{s}$. In fact, the normal vector n_i is not orthogonal to the axis. This is due to a change in the cross-section radius. As a consequence, the axial velocity must be distributed radially outwards or inwards as shown in figure 7. Note that the correction has to be radially directed, as the source choice.

The velocity potential of a source of strength $\sigma(s)$ is given as follows

$$\varphi_{\sigma}(s, c, n) = \sigma(s) \frac{\ln(\sqrt{c^2 + n^2})}{2\pi} \quad (31)$$

As the previous expression is not convenient we will prefer the cylindric coordinate

$$\varphi_{\sigma}(s, \theta, r) = \sigma(s) \frac{\ln(r)}{2\pi} \quad (32)$$

The velocity field due to a source placed at the centre of the cross-sectional disk is then given in the cylindric coordinates:

$$\vec{V}_{\sigma}(s, \theta, r) = \begin{pmatrix} \frac{\partial \varphi_{\sigma}}{\partial s} \\ \frac{\partial \varphi_{\sigma}}{\partial r} \\ \frac{\partial \varphi_{\sigma}}{\partial \theta} \end{pmatrix} = \begin{pmatrix} \frac{\partial \sigma}{\partial s} \frac{\ln(r)}{2\pi} \\ \sigma(s) \frac{1}{2\pi r} \\ 0 \end{pmatrix}_{(s, u_r, u_{\theta})} \quad (33)$$

Now consider the small element of the cylinder and its normal vector \vec{n}_i . Let us define ψ as the angle between \vec{n}_i and the cross-sectional plane (c, n) as shown in the figure 7. Due to the asymmetry of the problem, we will apply the single-point tightness condition. For the small angle approximation, ψ is equal to $\frac{dR}{ds}$, where R is the cross-section radius. The flow impermeability is then applied against \vec{n}_i and at R as follows

$$(\vec{V} \cdot \vec{s}) \cdot \vec{n}_i + \frac{\partial \phi}{\partial r}(R) \cdot \vec{s} = 0$$

When projected

$$-\vec{V} \cdot \vec{s} \sin(\psi) + \frac{\partial \phi}{\partial r}(R) \cos(\psi) = \frac{dR}{ds} \vec{V} \cdot \vec{s} + \frac{\partial \phi}{\partial r}(R)$$

Comes the source strength ensuring partial impermeability

$$\sigma(s) = 2\pi R \frac{dR}{ds} \vec{V} \cdot \vec{s} \quad (34)$$

The latter development shows that the source term does not contribute to the lift, but it provides better accuracy in the near flow modelling and captures the thickness of the fuselage. The impermeability of the flow at the cylinder surface is not fully taken into account as the cross-section velocity term V_{\perp} is not yet cancelled. Let us then consider a new singular element called the doublet of strength $\vartheta(s)$ with velocity potential expressed as

$$\phi_{\vartheta}(r, \theta, s) = \vartheta(s) \frac{\sin(\theta)}{2\pi r} \quad (35)$$

The resulting velocity field is expressed as :

$$\vec{V}_{\vartheta}(s, \theta, r) = \begin{pmatrix} \frac{\partial \varphi_{\vartheta}}{\partial s} \\ \frac{\partial \varphi_{\vartheta}}{\partial r} \\ \frac{\partial \varphi_{\vartheta}}{\partial \theta} \end{pmatrix} = \begin{pmatrix} \frac{\partial \vartheta}{\partial s} \frac{\sin(\theta)}{2\pi r} \\ -\vartheta(s) \frac{\sin(\theta)}{2\pi r^2} \\ -\vartheta(s) \frac{\cos(\theta)}{2\pi r^2} \end{pmatrix}_{(s, u_r, u_{\theta})} \quad (36)$$

Considering without loss of generality (under small angle assumption ie slender body) that $u_r = \cos(\psi)n_i \sim n_i$. The impermeability condition can be applied

against u_r at $r = R$ such that

$$\forall \theta V_{\perp}(s) \cdot \vec{u}_r - \vartheta(s) \frac{\sin(\theta)}{2\pi R^2} = 0$$

or as $V_{\perp}(s) \cdot \vec{u}_r = V_{\perp}(s)\sin(\theta)$ (as illustrated on figure 7), the impermeability condition becomes independent of θ and the doublet strength is finally given by

$$\vartheta(s) = 2\pi V_{\perp}(s)R^2 \quad (37)$$

Now as we have expressed the sources and doublet strength in function of the local geometry. We can use the incompressible unsteady Bernoulli equation to compute the unsteady lift applied on the section of the fuselage.

$$\rho \frac{\partial \phi}{\partial t} + \frac{1}{2} \rho \nabla \phi \cdot \nabla \phi + p = p_{\infty}$$

where $\nabla \phi$ is the flow field velocity expressed as the gradient of the total potential. In the cylindrical coordinate system, it is expressed as

$$\begin{aligned} \nabla \phi &= \begin{pmatrix} V \cdot \vec{s} + \frac{\partial \varphi}{\partial s} \\ V_{\perp} \sin \theta + \frac{\partial \varphi}{\partial r} \\ V_{\perp} \cos \theta + \frac{\partial \varphi}{\partial r} \frac{\partial \varphi}{\partial \theta} \end{pmatrix} \\ &= \begin{pmatrix} V \cdot \vec{s} + \frac{\partial \varphi}{\partial s} \\ 0 \\ V_{\perp} \cos \theta + \frac{\partial \varphi}{\partial r} \frac{\partial \varphi}{\partial \theta} \end{pmatrix} \end{aligned}$$

where the second term in the vector is equal to zero as imposed by the impermeability condition. Note that φ denotes the perturbation potential induced by the source and the doublet. For a seek of clarity we will use the notation $(\varphi_s \varphi_r \varphi_{\theta})$ as φ partial derivatives. Developing the scalar product comes the local dynamic pressure as follows

$$\begin{aligned} \frac{1}{2} \rho \nabla \phi \cdot \nabla \phi &= (V \cdot s + \varphi_s)^2 + (V_{\perp} \cos \theta + \varphi_{\theta})^2 \\ &= (V \cdot s)^2 + 2V_s V_s \\ &\quad + (V_{\perp} \cos \theta)^2 + 2V_{\perp} \cos \theta \varphi_{\theta} + \varphi_{\theta}^2 + \varphi_s^2 \end{aligned} \quad (38)$$

This equation is already quite untrackable but it provides good insights that are used in the next development. The total pressure force on the elementary slice of the fuselage is given by

$$\begin{aligned} \frac{d\vec{L}}{ds} &= - \int_C p(R, \theta) \vec{n}_i(R, \theta) dl \\ &= - \int_0^{2\pi} p(R, \theta) \vec{u}_r(R, \theta) R d\theta \end{aligned} \quad (39)$$

From now we can invoke the asymmetry property. First of all the normal vector is impair in $\theta + \pi$ ie $\vec{u}_r(\theta + \pi) = -\vec{u}_r(\theta)$. In other words, if some component of the local pressure is invariant spatially or respects the property $y(\theta + \pi) = y(\theta)$, their effects cancel

each other. When we inspect the element of 38 Every square component can be neglected and it comes

$$\frac{1}{2} \rho \nabla \phi \cdot \nabla \phi \doteq 2\varphi_s V_s + 2V_{\perp} \cos \theta \varphi_{\theta} \quad (40)$$

Note that in the equation above, we have used the \doteq notation to specify that only components that do not vanish with the imparity are conserved. Finally noting thanks to equation 36 and 33 the last term in equation 40 is proportional to $\cos \theta^2$ respects the parity property. The dynamic pressure is then simplified with no conservatism as

$$\frac{1}{2} \rho \nabla \phi \cdot \nabla \phi \doteq 2\varphi_s V \cdot s = 2 \frac{\partial \vartheta(s)}{\partial s} \frac{\sin(\theta)}{2\pi R} V \cdot s \quad (41)$$

By inspection of the temporal variation of the potential function comes the same type of simplification

$$\frac{\partial \phi}{\partial t} = \frac{\partial \varphi}{\partial t} \doteq \frac{\partial \vartheta(s)}{\partial t} \frac{\sin(\theta)}{2\pi r} \quad (42)$$

As a consequence the simplified expression of the local pressure located in (s, R, θ)

$$-p(\theta, R) \doteq 2 \frac{\partial \vartheta(s)}{\partial s} \frac{\sin(\theta)}{2\pi R} V \cdot s + \frac{\partial \vartheta(s)}{\partial t} \frac{\sin(\theta)}{2\pi R} \quad (43)$$

Now denoting that $n(\theta) = \cos(\theta)c_{\perp} + \sin(\theta)n_{\perp}$ After integration, it comes

$$\frac{d\vec{L}}{ds} = \left(\frac{\partial \vartheta(s)}{\partial s} V \cdot s + \frac{1}{2} \frac{\partial \vartheta(s)}{\partial t} \right)$$

Deriving the doubet strength against t and s using its definition 37 it comes

$$\begin{aligned} \frac{d\vec{L}}{ds} &= 2\pi\rho V \cdot s V_{\perp} R \frac{dR}{ds} \vec{n}_{\perp} - \rho 2\pi \frac{\partial V_{\perp}}{\partial t} R^2 \vec{n}_{\perp} \\ &= 2\pi\rho V \cdot s V_{\perp} R \frac{dR}{ds} \vec{n}_{\perp} - \rho 2\pi a_{i,\perp} R^2 \vec{n}_{\perp} \end{aligned}$$

Denoting that $\vec{n}_{\perp} = \frac{\vec{V}_{\perp}}{V_{\perp}} = \frac{\vec{a}_{\perp}}{a_{\perp}}$ it comes the final expression of the elementary lift.

$$\begin{aligned} \frac{d\vec{L}}{ds} &= 2\pi\rho V \cdot s \vec{V}_{\perp} R \frac{dR}{ds} - \rho 2\pi a_{i,\perp} R^2 \\ &= 2\pi\rho V \cdot s \vec{V}_{\perp} R \frac{dR}{ds} - \rho 2\pi (\vec{a}_i - (\vec{a}_i \cdot \vec{s}) \vec{s}) R^2 \end{aligned} \quad (44)$$

44 is the combination of Eq (68) and (86) of the Drela's technical document. This equation highlights the different properties of the lift. First of all, it does not depend on the source strength but only on that of the doublets. Secondly, the lift and added mass forces (unsteady part of the lift equation) will point towards the same/opposite direction of the cross-section projection of the local velocity ie acceleration. Indeed in the steady case, the direction of lift is $\frac{dR}{ds}$ sign dependant as depicted in figure 2.

Appendix B: The vectorial formulation of the unsteady Kutta Joukowski theorem

Let us consider a thin vortex sheet S made of an airfoil and wake vortex sheets S_a and S_w such that $S = S_a \cup S_w$. At any point P on S let V^+ and V^- be the upper and lower velocities as depicted in the figure 37. We define the jump operator $\Delta\Box$ of any variable \Box as the difference $\Box^+ - \Box^-$. The vortex sheet distribution $\gamma_a(\xi)$ results in a tangential velocity jump equal to the local strength

$$\gamma_a(\xi) = V^+ - V^- = \Delta V \quad (45)$$

The local vortex sheet is oriented in the spanwise direction such that

$$\gamma(\vec{\xi}) = \vec{\eta} \times \Delta \vec{V}(\xi) = \Delta V \vec{s} \quad (46)$$

where $\vec{\eta}$ and \vec{s} are respectively the vortex sheet normal and spanwise unit vectors. From incompressible and irrotational condition the 2D flow can be modeled by a potential function $\phi(\xi, \eta)$ such that

$$\vec{V} = \nabla \phi = \begin{pmatrix} \frac{\partial \phi}{\partial \xi} \\ \frac{\partial \phi}{\partial \eta} \end{pmatrix} \quad (47)$$

One can define any closed curve C that connects the upper and lower side of the sheet in P (cf figure 37). The circulation Γ is then defined as

$$\Gamma = \oint_C \vec{V} \cdot d\vec{\xi} = \oint_C \nabla \phi \cdot d\vec{\xi} \quad (48)$$

Note that equation 48 can be separated as follow

$$\Gamma = \oint_{C^+} \nabla \phi^+ \cdot d\vec{\xi} - \oint_{C^-} \nabla \phi^- \cdot d\vec{\xi} \quad (49)$$

with $d\vec{\xi}$ always tangent to the vortex sheet. If we evaluate this integral on the vortex sheet, the velocity is tangent to s , in consequence, $\nabla \phi = \begin{pmatrix} \frac{\partial \phi}{\partial \xi} \\ 0 \end{pmatrix}$ Equation 49 simplifies then to

$$\Gamma = \oint_{C^+} \frac{\partial \phi^+}{\partial \xi} \cdot d\xi - \oint_{C^-} \frac{\partial \phi^-}{\partial \xi} \cdot d\xi \quad (50)$$

That is finally given as

$$\Gamma = \oint_{C^+} \partial \phi^+ - \oint_{C^-} \partial \phi^- = \phi^+ - \phi^- = \Delta \phi \quad (51)$$

From the equation 51 comes the vorticity strength distribution as follows.

$$\vec{\gamma} = \vec{n} \times \Delta \vec{V} = \vec{n} \times \vec{\nabla} \Delta \phi = \vec{n} \times \vec{\nabla} \Gamma \quad (52)$$

Now from the unsteady Bernoulli equation, the local pressure jump on the airfoil vorticity sheet can be computed

$$\frac{\partial \phi^+}{\partial t} + \frac{1}{2} V^{+,2} + \frac{p^+}{\rho} = \frac{\partial \phi^-}{\partial t} + \frac{1}{2} V^{-,2} + \frac{p^-}{\rho}$$

rearranged in

$$\frac{\partial \Delta \phi}{\partial t} + \frac{1}{2} \Delta(V^2) = -\frac{\Delta p}{\rho} \quad (53)$$

The dynamic pressure jump in 53 can be expressed as follows

$$\frac{1}{2} \Delta(V^2) = \frac{1}{2} (V^+ - V^-) \cdot (V^+ + V^-) = \Delta \vec{V} \cdot \vec{V}$$

Using equation 46 combined with 52 The previous equation can be simplified to

$$\frac{1}{2} \Delta(V^2) = \vec{\eta} \cdot (\vec{V} \times \vec{s})$$

The local pressure jump is finally expressed using expression 51:

$$-\Delta p(\xi) = \rho \left(\frac{\partial \Gamma}{\partial t} + \vec{\eta} \cdot (\vec{V} \times \vec{s}) \right) \quad (54)$$

Now in ASWING, the vortex sheet S_a is lumped into a vortex line of strength Γ at the quarter chord location as described in figure 37. Also, the wake vortex sheet is now considered as a straight prescribed wake of strength Γ_w . From the Kutta condition at the trailing edge ie zero pressure jump $\Gamma_w = \Gamma$. As the wake is by definition force free only the pressure forces over the airfoil have to be integrated. As $\gamma(\xi)$ distribution has been lumped its strength can be expressed as $\gamma(\xi) = \frac{\Gamma}{c_\beta}$. The contribution of circulation variables to the lift is then given by

$$\begin{aligned} \vec{f}_{lift,\Gamma} &= \int_0^{c_\beta} \Delta p d\xi \vec{\eta} = \rho \frac{\partial \Gamma}{\partial t} c_\beta \vec{\eta} + \rho \Gamma (\vec{V} \times \vec{s}) \\ &= \rho \frac{\partial \Gamma}{\partial t} c_\beta \frac{\Gamma (\vec{V} \times \vec{s})}{|V|} + \rho \Gamma (\vec{V} \times \vec{s}) \end{aligned} \quad (55)$$

One has denoted c_β instead of the local chord c . The reason is that in the ASWING model, the wake is wind-aligned. It means that it does not necessarily lie in the cross-section place (c,n) as described in figure 4(a). Or, as the unsteady vectorial Kutta-Joukowsky theorem is 2D it must be integrated into the plane where the horseshoe legs of the wake. The local chord must be changed in consequence. By denoting V_\perp as the projected velocity vector into the cross-section plane (c, n), we can identify thanks to figure 4(b) that

$$\frac{c_\beta}{c} = \frac{|V|}{|V_\perp|}$$

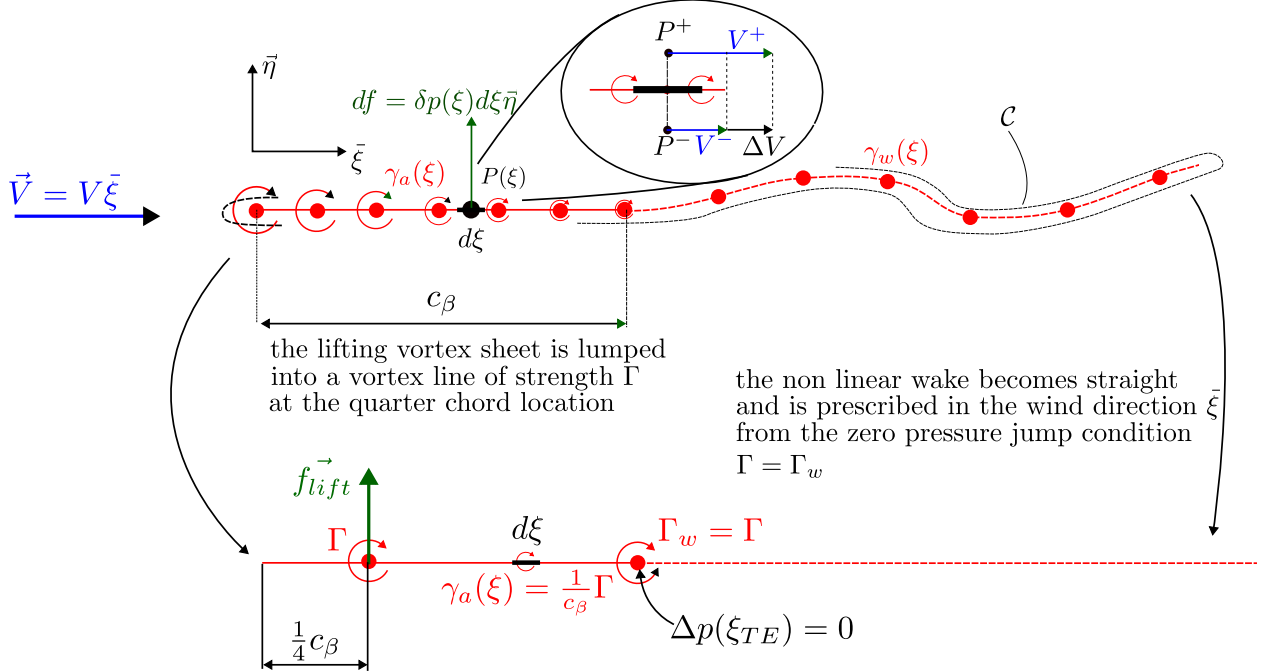


Figure 37: Kutta-Joukowsky theorem illustration of the vortex sheet lumping and simplification

Using it in equation 55 leads to the final expression of the unsteady circulatory lift.

$$\vec{f}_{lift,\Gamma} = \rho c \frac{\partial \Gamma}{\partial t} \frac{(\vec{V} \times \vec{s})}{|V_\perp|} + \rho \Gamma (\vec{V} \times \vec{s}) \quad (56)$$

Equation 3 is finally consistent with equations (38) of Drela (2008). In light of the equation we can notice that despite the Kutta Joukowsky theorem has been derived into a 2D plane that does not necessarily lie into the cross-section one, the lift forces lie into it as depicted in figure 3(a). Note that we have denoted the lift induced by the circulation variable Γ .

Appendix C: XFOIL analysis of the effect of the Reynolds number and a deflected flap on the ASWING parameters

An XFOIL analysis of NACA4415 is presented in figure 38. Figure 38 (a) highlights the variation of the lift stall and zero lift angle with angle of attack. Figure 38 (b) depicts the lift stall shifting with a flap deflection. Figures 38 (c) and (d) highlight the flap derivatives linearity with flap deflection angle and their variation with the Reynolds number.

their exact value are not reported in the technical document [37]. Figures 43 and 42 present the analysis of the forward wing airfoils that are denoted as JWR, JWJ, JWT with R, J and T standing for Root, Joint and Tip. Figures 43 and 42 present the analysis of the rear wing airfoils that are denoted as JTR, JTT.

Appendix D : Boeing KC-135 geometry and MSES airfoil analysis:

The figure 39 presents 4 MSES (Drela and Giles 1987 and 1993) KC-130-A airfoil analysis at 2 lift coefficients. The effect of the Mach number and lift coefficient on the appearance of the shock can be clearly identified. Also, the effect of the shock position on the boundary layer thickness and thus friction drag is also illustrated. There is a huge dependency of the drag coefficient with the Ma number and lift coefficient at transonic flow thus the discrepancies identified in the transonic cases presented earlier in the report. Figure 40 presents all the geometric parameters and airfoil of the KC-130 to reproduce the aircraft in ASWING.

Appendix E : Diamond joined wing, airfoil XFOIL analysis

This appendix presents the XFOIL analysis performed for each airfoil of the diamond joined wing used in case *S4 – 15Atoc*. For each airfoil, the following XFOIL parameters have been used : $R_e = 1E6$, $M_a = 0.35$, $X_{tr}/c = 0.35$, $N = 5$. Where X_{tr} is the forced boundary layer transition position and N is the amplification coefficient. Those parameters are based on the technical report [37] where a forced transition is mentioned at the above location. To compute the flap derivatives, the analysis have been performed at 2 different Reynolds number that are $R_e = 1E6$ and $R_e = 0.625E6$. This because some of the rolling moment measurement have been performed at lower dynamic pressure because it was exceeding the balance limits. In the end it turns out that the flap derivatives are barely changing with the Reynolds number. Note that several analysis have been performed with various hinge location (0.70c, 0.75c, 0.80c and 0.85c) because

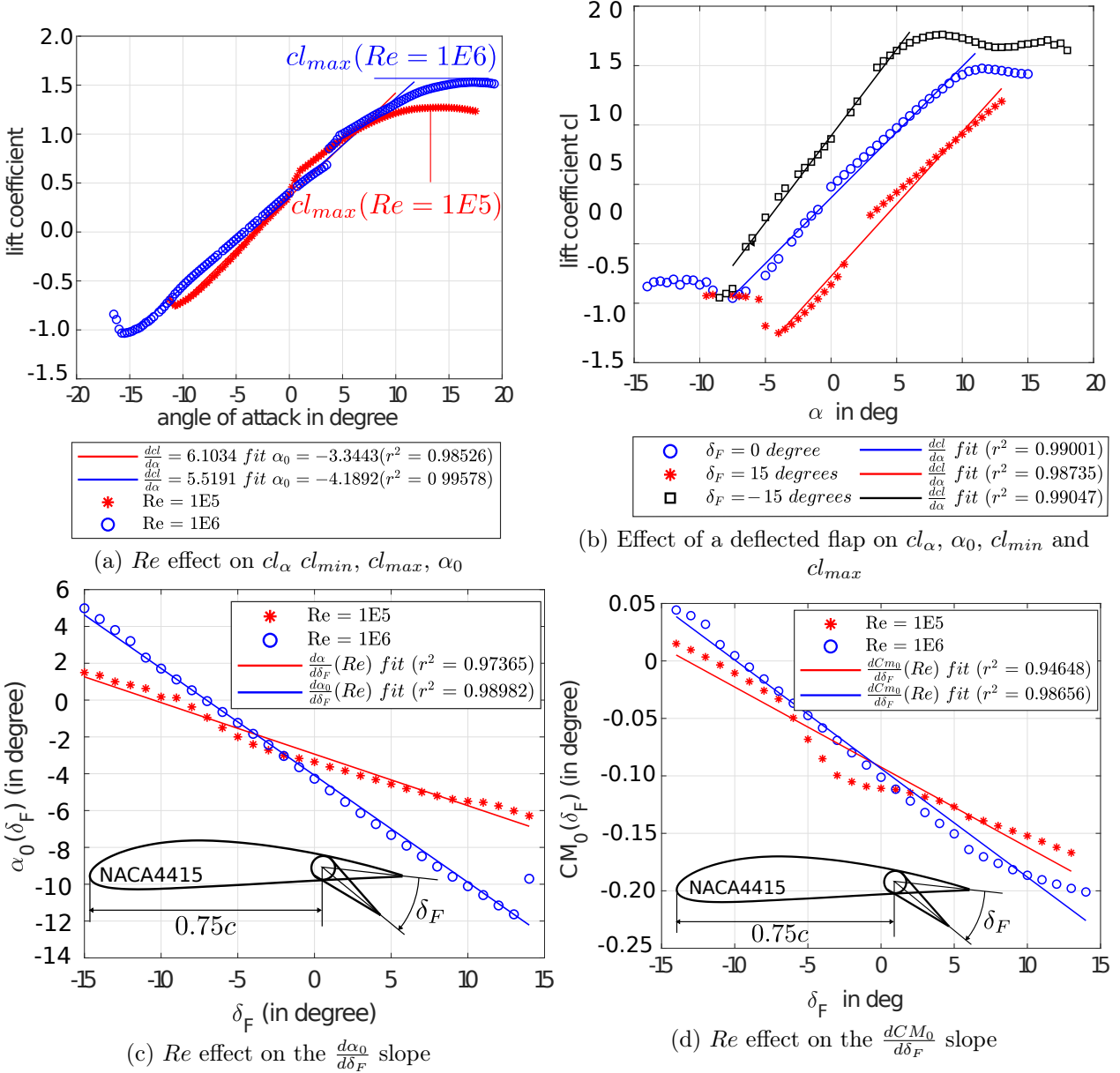


Figure 38: Effect of Reynolds number and flap deflection on ASWING airfoil derivatives. Illustration on the NACA4415

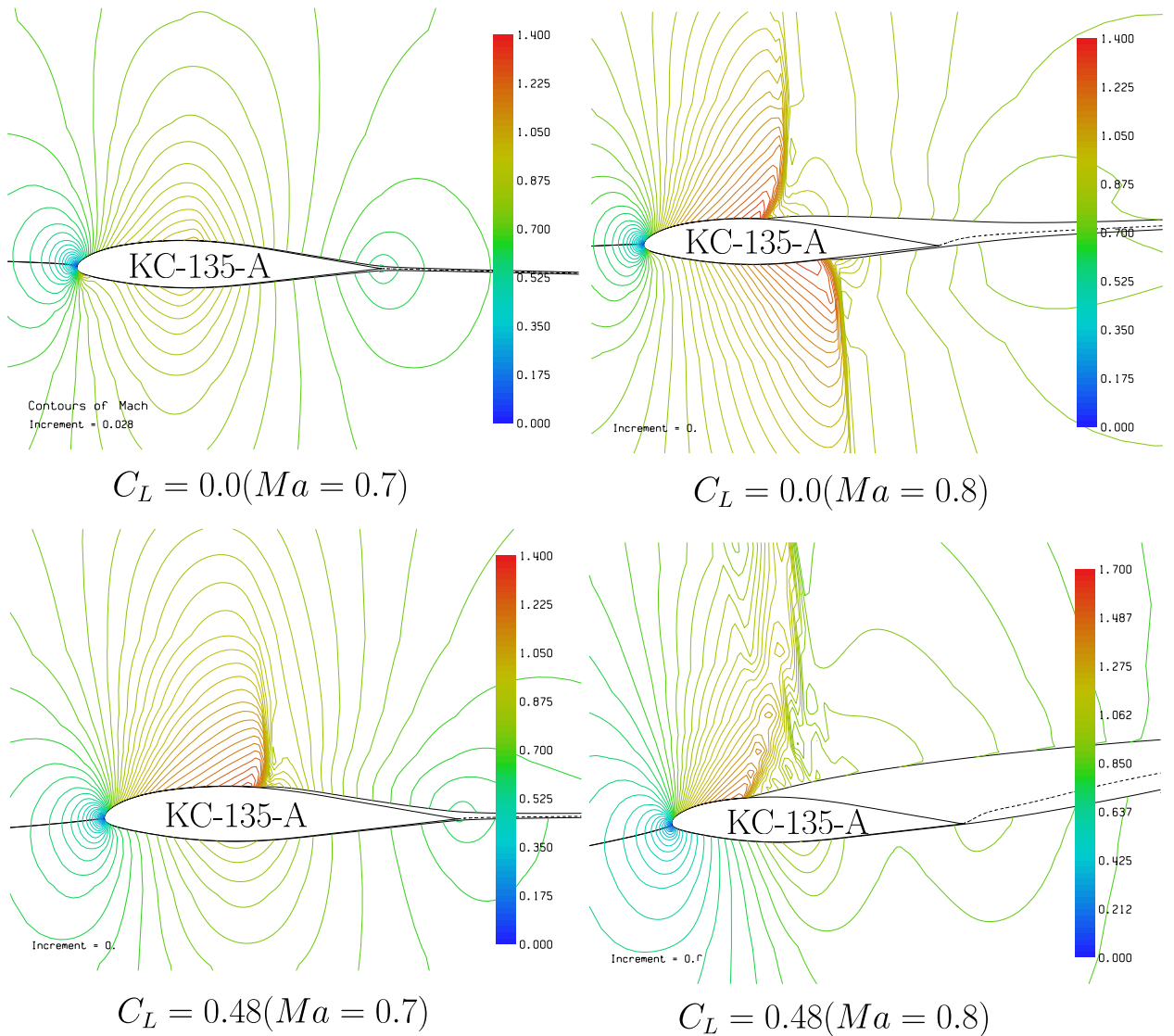


Figure 39: Appendix-D:Boeing KC-135 geometry and airfoils

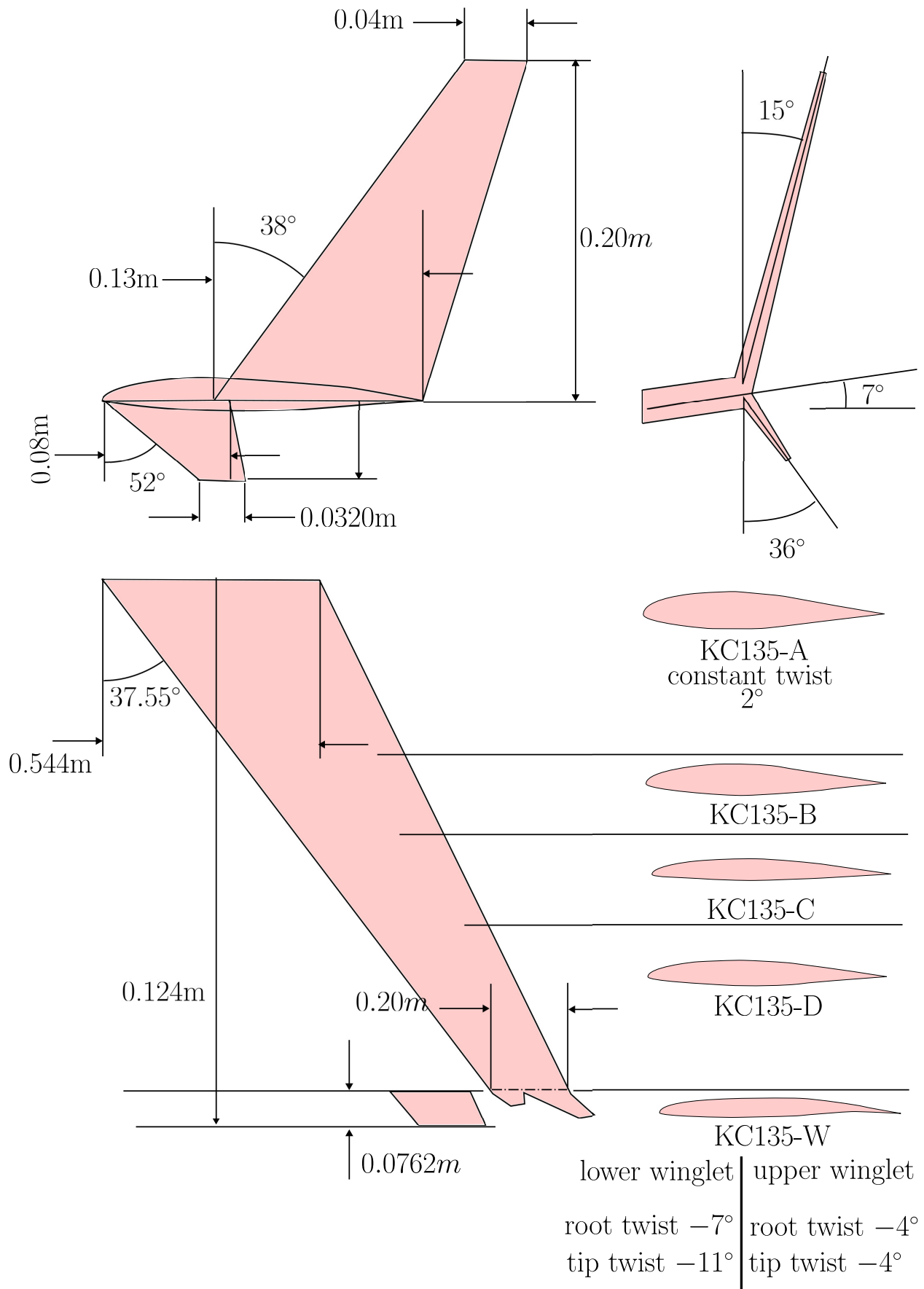


Figure 40: Appendix-D: Boeing KC-135 geometry and airfoils

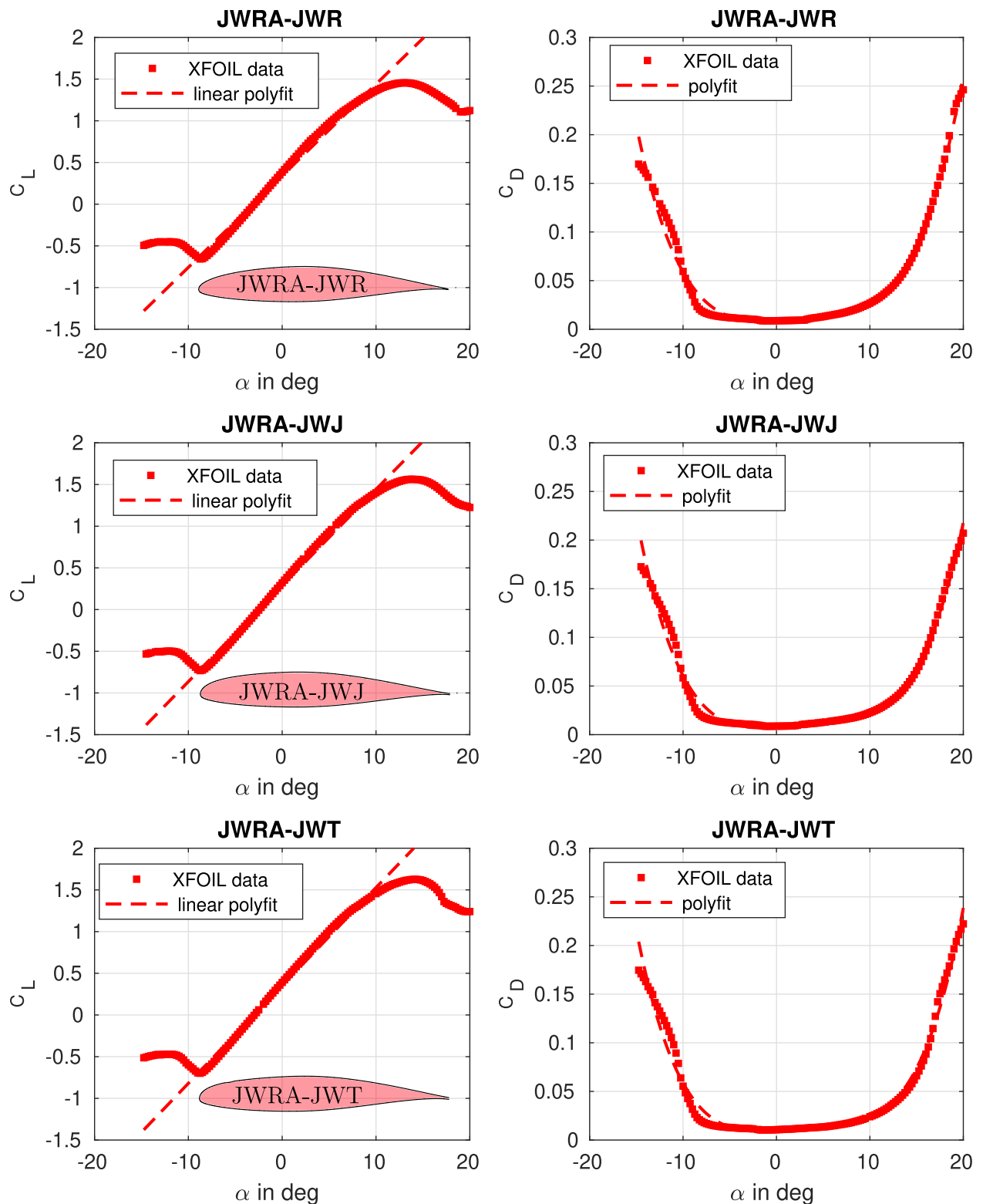


Figure 41: Appendix-E : Diamond Joined wing (JWRA) forward wing airfoil polars

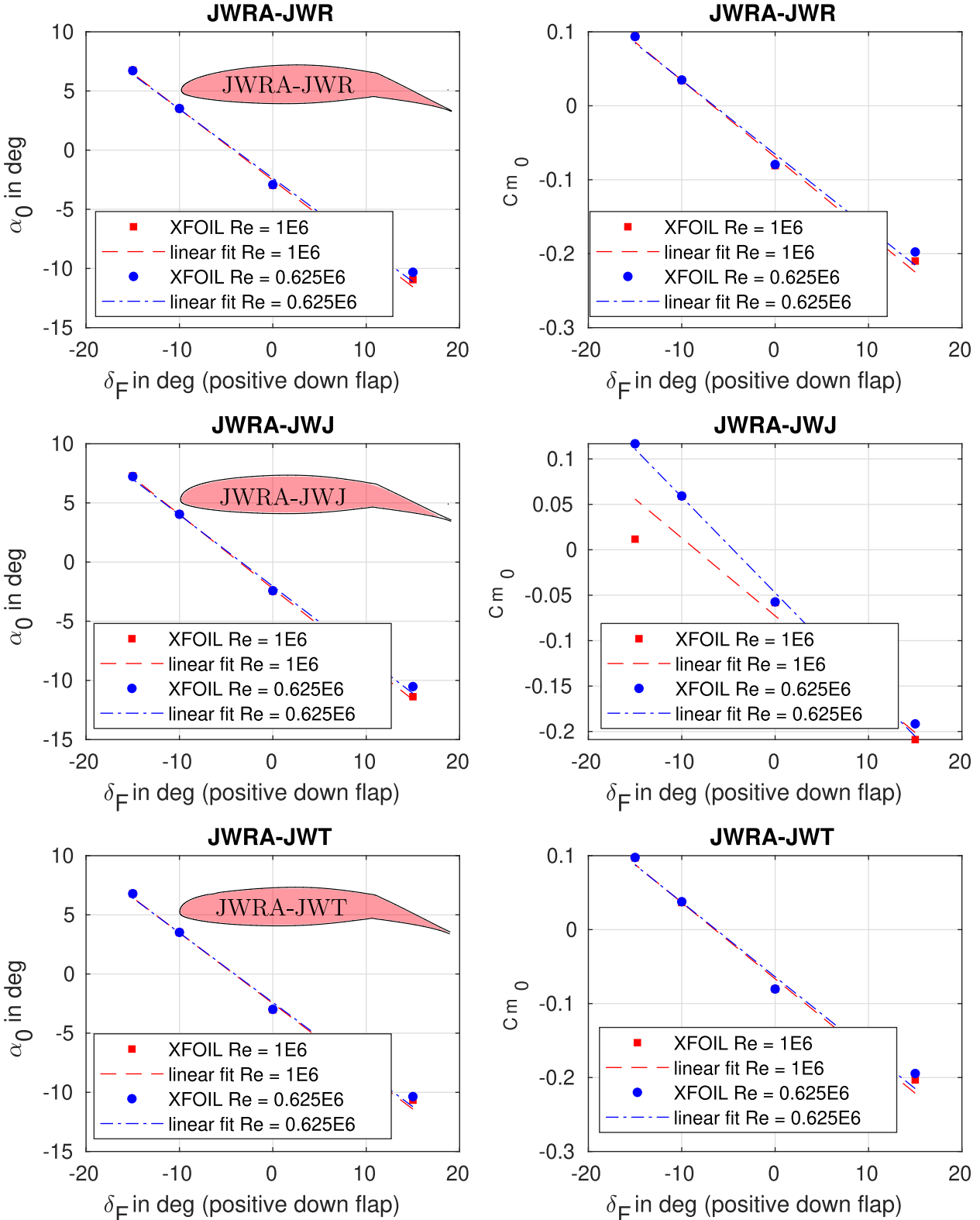


Figure 42: Appendix-E : Diamond Joined wing (JWRA) forward wing airfoil flap derivatives with the hinge located at 0.70c.

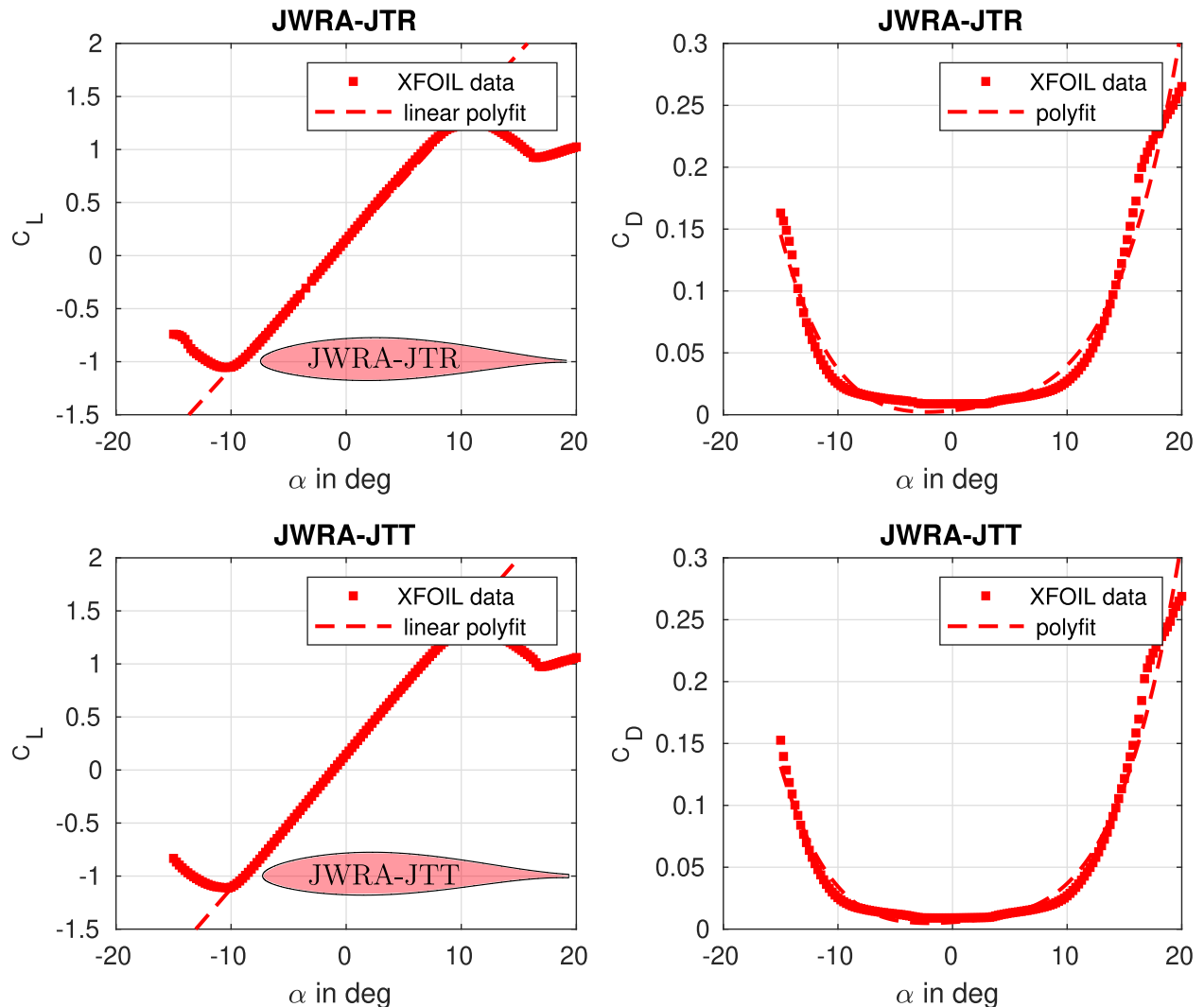


Figure 43: Appendix-E : Diamond Joined wing (JWRA) rear wing airfoil polars

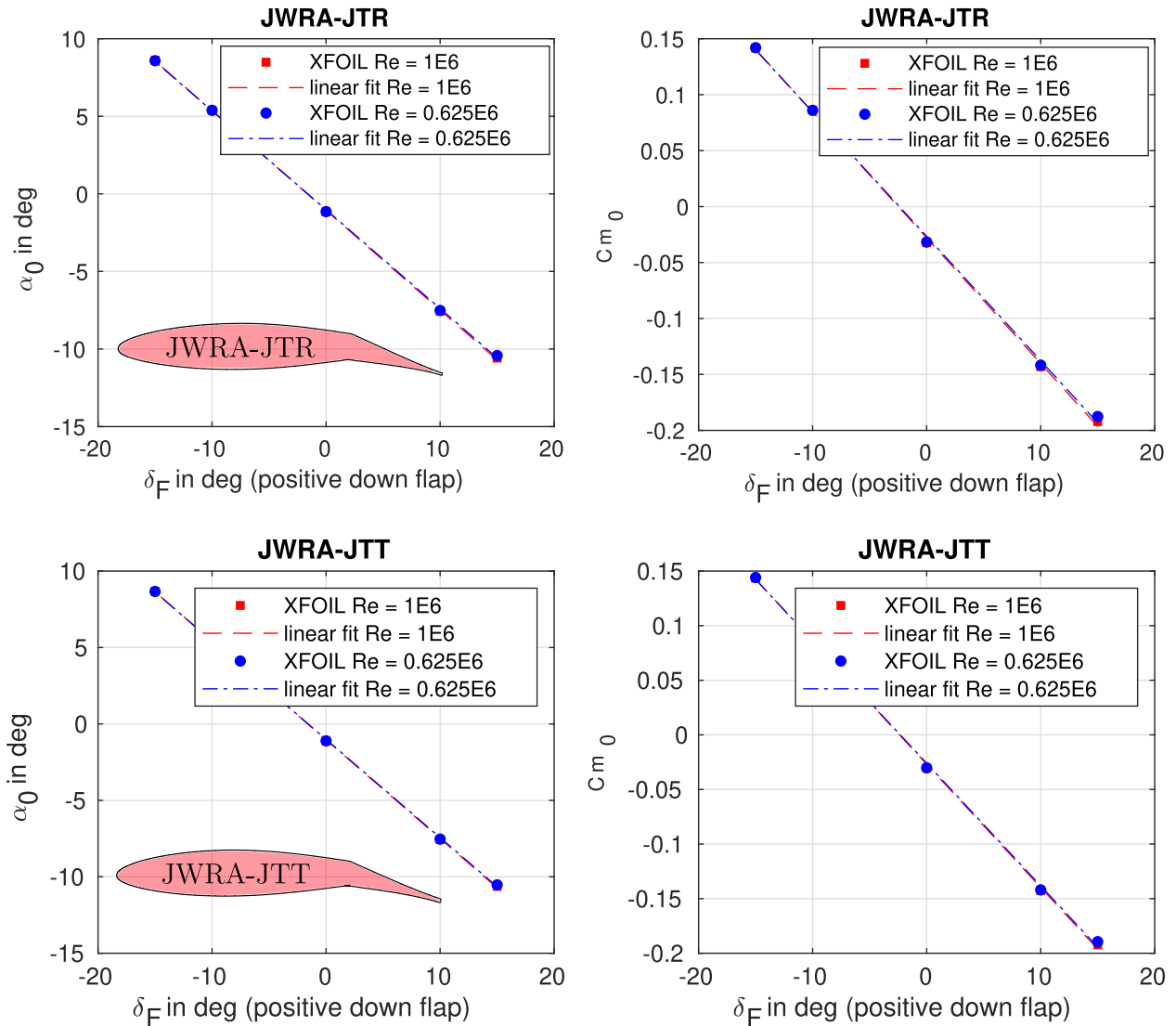


Figure 44: Appendix-E : Diamond Joined wing (JWRA) rear wing airfoil flap derivatives with the hinge located at 0.70c.

References

- [1] Applin, Z. T. (1995). Pressure Distributions From Subsonic Tests of a NACA 0012 Semispan Wing Model. NASA Technical Memorandum 110148, NASA, Langley Research Center, Hampton, Virginia.
- [2] Barber, M. R. and Selegan, D. (1982). Kc-135 winglet program overview. *KC-135 Winglet Program Rev.*, (NASA-CP-2211).
- [3] Chandre-Vila, O., Boin, J.-P., Barriety, B., Nivet, Y., Morlier, J., and Gourdain, N. (2023). Fast Nonlinear Static Aeroelasticity Method for High-Aspect-Ratio Wings at Different Mach Regimes. *Journal of Aircraft*, pages 1–21.
- [4] Chandre Vila, O., Nivet, Y., Morlier, J., and Gourdain, N. (2022). Fast Method For Dynamic Fluid-Structure Interactions Considering Unsteady Aerodynamics. In *AIAA SCITECH 2022 Forum*, San Diego, CA & Virtual. American Institute of Aeronautics and Astronautics.
- [5] Chauhan, S. S. and Martins, J. R. R. A. (2019). Low-Fidelity Aerostructural Optimization of Aircraft Wings with a Simplified Wingbox Model Using OpenAeroStruct. In Rodrigues, H., Herskovits, J., Mota Soares, C., Araújo, A., Guedes, J., Folgado, J., Moleiro, F., and Madeira, J. F. A., editors, *EngOpt 2018 Proceedings of the 6th International Conference on Engineering Optimization*, pages 418–431. Springer International Publishing, Cham.
- [6] Cheng, H. and Wang, H. (2018). Prediction of Lift Coefficient for Tandem Wing Configuration or Multiple-Lifting-Surface System Using Prandtl's Lifting-Line Theory. *International Journal of Aerospace Engineering*, 2018:1–15.
- [7] Chiereghin, N., Cleaver, D., and Gursul, I. (2017a). Unsteady Force and Flow Measurements for Plunging Finite Wings. In *47th AIAA Fluid Dynamics Conference*, Denver, Colorado. American Institute of Aeronautics and Astronautics.
- [8] Chiereghin, N., Cleaver, D., and Gursul, I. (2017b). Unsteady Measurements for a Periodically Plunging Airfoil. In *55th AIAA Aerospace Sciences Meeting*, Grapevine, Texas. American Institute of Aeronautics and Astronautics.
- [9] Chreim, J. R. (2019). *Development of a propeller Lifting-Line tool for analysis and design*. Mestrado em Engenharia Mecânica de Energia de Fluidos, Universidade de São Paulo, São Paulo.
- [10] Colas, D., Roberts, N. H., and Suryakumar, V. S. (2018a). HALE Multidisciplinary Design Optimization Part I: Solar-Powered Single and Multiple-Boom Aircraft. In *2018 Aviation Technology, Integration, and Operations Conference*, Atlanta, Georgia. American Institute of Aeronautics and Astronautics.
- [11] Colas, D., Roberts, N. H., and Suryakumar, V. S. (2018b). HALE Multidisciplinary Design Optimization Part I: Solar-Powered Single and Multiple-Boom Aircraft. In *2018 Aviation Technology, Integration, and Operations Conference*, Atlanta, Georgia. American Institute of Aeronautics and Astronautics.
- [12] Drela, M. (1993). Design and optimization method for multi-element airfoils. In *Aerospace Design Conference*, page 969.
- [13] Drela, M. (1999). Integrated simulation model for preliminary aerodynamic, structural, and control-law design of aircraft. In *40th Structures, Structural Dynamics, and Materials Conference and Exhibit*, St. Louis, MO, U.S.A. American Institute of Aeronautics and Astronautics.
- [14] Drela, M. (2008). ASWING 5.81 Technical Description — Unsteady Extension. page 42.
- [15] Drela, M. (2009). ASWING 5.86 Technical Description — Steady Formulation. page 57.
- [16] Drela, M. (2014). *Flight vehicle aerodynamics*. MIT press.
- [17] Drela, M. and Giles, M. B. (1987). Viscous-inviscid analysis of transonic and low reynolds number airfoils. *AIAA journal*, 25(10):1347–1355.
- [18] ESCUDERO, C. F. (2021). *Contrôle passif des instabilités aéroélastiques des ailes d'avion par ajout d'oscillateurs non linéaires*. PhD thesis, Université de Toulouse, ISAE-SUPAERO, Polytechnique Montréal, Toulouse/Montréal.
- [19] Feistel, T. W., Corsiglia, V. R., and Levin, D. B. (1981). Wind-Tunnel Measurements of Wing-Canard Interference and a Comparison with Various Theories. *SAE Transactions*, 90:2026–2039. Publisher: SAE International.
- [20] Fernandez-Escudero, C., Gagnon, M., Laurendeau, E., Prothien, S., Michon, G., and Ross, A. (2019). Comparison of low, medium and high fidelity numerical methods for unsteady aerodynamics and nonlinear aeroelasticity. *Journal of Fluids and Structures*, 91:102744.
- [21] González, O., Boschetti, P., Cárdenas, E., and Amerio, A. (2010). Static-Stability Analysis of an

- Unmanned Airplane as a Flexible-Body. In *AIAA Atmospheric Flight Mechanics Conference*, Toronto, Ontario, Canada. American Institute of Aeronautics and Astronautics.
- [22] Heald, R. and Strother, D. (1929). Report No. 298. Effect of variation of chord and span of ailerons on rolling and yawing moments in level flight. *Journal of the Franklin Institute*, 207(5):715–716.
- [23] Heald, R. and Strother, D. (1930). Report No. 343. Effect of variation of chord and span of ailerons on rolling and yawing moments at several angles of pitch. *Journal of the Franklin Institute*, 210(1):126–127.
- [24] J. Weber, Dr.rer.nat. and G. G. Brebner, M.A (1958). Low-Speed Tests on 45.deg Swept.back Wings Part I. Pressure Measurements on Wings of Aspect Ratio 5. Aeronautical Research Council Reports And Memoranda 2882, London" Her Majesty'S Stationery Office.
- [25] Jacobs, P. F., Flechner, S. G., and Montoya, L. C. (1977). Effect of winglets on a first-generation jet transport wing. 1: Longitudinal aerodynamic characteristics of a semispan model at subsonic speeds. Technical Report NASA-TN-D-8473, NASA.
- [26] Jan, R., Condomines, J.-P., and Moschetta, J.-M. (2021). Fast simulation model for control law design and benchmark of high aspect ratio flexible UAVs. In *International Micro Air Vehicle Conference*, Mexico City, Mexico.
- [27] Jasa, J. P., Hwang, J. T., and Martins, J. R. R. A. (2018). Open-source coupled aerostructural optimization using Python. *Structural and Multidisciplinary Optimization*, 57(4):1815–1827.
- [28] Jones, J. (2017). *Development of a very flexible testbed aircraft for the validation of nonlinear aeroelastic codes*. PhD thesis, University of Michigan, USA.
- [29] Kroo, I., Gallman, J., and Smith, S. (1991). Aerodynamic and structural studies of joined-wing aircraft. *Journal of aircraft*, 28(1):74–81.
- [30] Lin, H.-H., Jhou, J., and Stearman, R. (1989). Influence of joint fixity on the structural static and dynamic response of a joined-wing aircraft: Part i: Static response. *SAE Transactions*, pages 221–234.
- [31] Love, M., Zink, P., Wieselmann, P., and Younghren, H. (2005). Body Freedom Flutter of High Aspect Ratio Flying Wings. In *46th AIAA/ASME/ASCE/AHS/ASC Structures, Structural Dynamics and Materials Conference*, Austin, Texas. American Institute of Aeronautics and Astronautics.
- [32] Martina, A. P. (1956). The interference effects of a body on the spanwise load distributions of two 45 degree sweptback wings of aspect ratio 8.02 from low-speed tests. Technical Report NACA-TN-3730, NACA.
- [33] McCormack, G. and Stevens Jr, V. I. (1947). An investigation of the low speed stability and control characteristics of swept-forward and swept-back wings in the ames 40-by 80-foot wind tunnel. Technical Report NACA-RM-A6K15, NACA.
- [34] Miklosovic, D. S. (2008). Analytic and Experimental Investigation of Dihedral Configurations of Three-Winglet Planforms. *Journal of Fluids Engineering*, 130(7):071103.
- [35] Milne-Thomson, L. M. (1973). *Theoretical aerodynamics*. Courier Corporation.
- [36] Recant, I. G. (1939). Wind-tunnel investigation of ground effect on wings with flaps. Technical Report NACA-TN-705, NACA.
- [37] Smith, S. C. and Stonum, R. K. (1989). Experimental aerodynamic characteristics of a joined-wing research aircraft configuration. NASA Technical Memorandum NASA-TM-101083, NASA.
- [38] Stearman, R. (1990). Influence of joint fixity on the aeroelastic characteristics of a joined wing structure. In *31st Structures, Structural Dynamics and Materials Conference*, page 980.
- [39] Theodore Theodorsen (1935). Report No. 496, general theory of aerodynamic instability and the mechanism of flutter. *Journal of the Franklin Institute*, 219(6):766–767.
- [40] Upson, R. H. and Klikoff, W. (1933). Application of practical hydrodynamics to airship design. NACA Technical Report 405, NACA.
- [41] van Dam, C. P., Vijgen, P. M. H. W., and Holmes, B. J. (1991). Experimental investigation on the effect of crescent planform on lift and drag. *Journal of Aircraft*, 28(11):713–720.
- [42] VanDorn, N. H. and DeYoung, J. (1947). A comparison of three theoretical methods of calculating span load distribution on swept wings. Technical Report NACA-RM-A7C31, NACA.
- [43] Variyar, A., Economou, T. D., and Alonso, J. J. (2017). Design and Optimization of Unconventional Aircraft Configurations with Aeroelastic Constraints. In *55th AIAA Aerospace Sciences Meeting*, Grapevine, Texas. American Institute of Aeronautics and Astronautics.

- [44] Von Karman, T. (1930). Calculation of pressure distribution on airship hulls. NACA Technical Memorandum 574.
- [45] Warwick, S., Bras, M., Richards, J., and Suleiman, A. (2019). Measurement of Aeroelastic Wing Deflections Using Modal Shapes and Strain Pattern Analysis. In *AIAA Scitech 2019 Forum*, San Diego, California. American Institute of Aeronautics and Astronautics.
- [46] Wenzinger, C. J. and Harris, T. A. (1939). Wind-tunnel investigation of an naca 23021 airfoil with various arrangements of slotted flaps. Technical report, US Government Printing Office.
- [47] Werter, N. and De Breuker, R. (2016). A novel dynamic aeroelastic framework for aeroelastic tailoring and structural optimisation. *Composite Structures*, 158:369–386.
- [48] Wolkovitch, J. (1982a). Low-speed wind tunnel test on joined wing and monoplane configurations. volume 1. analysis of results. Technical Report Nasa contractor report N00014-79-C-0953 or ACA Report 82-1, NASA.
- [49] Wolkovitch, J. (1982b). Low-speed wind tunnel test on joined wing and monoplane configurations. volume 2. test data. Technical Report Nasa contractor report N00014-79-C-0953 or ACA Report 82-2, NASA.



Adresse postale
ISAE-SUPAERO
10 avenue É. Belin – BP 54032
31055 Toulouse CEDEX 4 – France

Téléphone
33 (0)5 61 33 80 80

Site internet
www.isae-supaero.fr